2. GLOBAL CLIMATE—R. J. H. Dunn, D. F. Hurst, N. Gobron, and K. M. Willett, Eds.

a. *Overview*—R. J. H. Dunn, D. F. Hurst, N. Gobron, and K. M. Willett

For yet another year in succession, 2016 was the warmest at the surface in the 150-year instrumental record with global annual anomalies between 0.45°–0.56°C above the 1981–2010 average but by a lesser margin than the previous two. The strong El Niño continued to dominate global conditions during the early part of the year, but the El Niño–Southern Oscillation (ENSO) transitioned to a weak La Niña as the year progressed. Also of note is the largest annual increase of global atmospheric CO_2 ever observed in the 58-year measurement record, with an increase of 3.5 ± 0.1 ppm since 2015 to 402.9 ± 0.1 ppm.

Many other essential climate variables (ECVs), especially those closely linked to surface temperature, responded to these exceptionally warm conditions. Upper atmospheric, lake, and extreme surface temperatures all exhibited exceptional if not record warmth. In the cryosphere, glaciers continued to have a negative mass balance, now for the 37th successive year. And although the winter season Northern Hemisphere snow cover extent was near average, the rapid increase in snow cover during autumn and decrease during spring is consistent with warmer-than-average conditions.

The global warmth was associated with extensive drought. The global drought extent surpassed most years in the post-1950 record and was strongly influenced by the El Niño, with every month of 2016 having at least 12% of global land experiencing severe drought conditions. Despite this, strong decreases in fire-related emissions were measured in 2016 for Australia and North America. Tropical Asia also saw decreases in fire-related emissions from the 2015 record high levels to near-record low levels in 2016, but increases occurred for northern and Southeast Asia. Also, atmospheric moisture at the surface and in the upper troposphere was high, and at record levels for surface specific humidity over land, but with little change in global levels of cloudiness. These high levels of moisture were also apparent in the water vapor column, which peaked in line with the El Niño in early 2016 and reached record levels over the oceans. The global average fraction of photosynthetically available radiation (FAPAR) was also above average. Levels of precipitation globally were above average, although by how much depended on the dataset analyzed.

Global atmospheric burdens of the three dominant greenhouse gases (CO_2, CH_4, and N_2O) continued their long-term upward trends in 2016. Increases in the global annual mean mole fractions of CH_4 and N_2O from 2015 to 2016 were fairly consistent with decadal trends, but the 3.5 ± 0.1 ppm (0.88% ± 0.03%) rise in global annual mean CO_2 from 2015 to 2016 was the largest annual increase ever observed in the 58-year atmospheric measurement record. This strong growth pushed the 2016 global average CO_2 mole fraction at Earth's surface above 400 ppm (402.9 ± 0.1 ppm) for the first time in the modern atmospheric measurement record and in ice core records dating back as far as 800 000 years. In mid-2016 the global burden of carbon monoxide (CO) returned to near its long-term average after spiking in mid-2015 due to extreme biomass fires in Indonesia.

The burdens of many ozone-depleting substances continued to decline, lowering their associated radiative forcing and reducing stratospheric halogen loading. Ozone measurements in the upper stratosphere (~40 km) indicate a 2%–4% decade^{-1} increase since the late 1990s that may signal the start of ozone layer recovery. Water vapor anomalies in the tropical lower stratosphere (~17 km) decreased from 0.9 ppm in December 2015 to near –1.0 ppm in November 2016. This 1.9 ppm drop is equal to 40% of the 13-year average abundance of tropical lower stratospheric water vapor in November. The atypical evolution of the quasi-biennial oscillation during 2016 was undoubtedly a strong contributor to this abrupt and severe drying of the tropical lower stratosphere. The 2016 global averages of total aerosol optical depth and tropospheric ozone again exceeded the previous year's global averages, continuing their upward trends since 2003 and 2004.

In the Southern Hemisphere, the Antarctic Oscillation remained positive until late 2016, which combined with the fading of the El Niño, led to a retreat of the West Antarctic Peninsula sea ice margin. The North Atlantic Oscillation was on the whole positive in both the 2015/16 and 2016/17 winters. Globally, land surface wind speed showed only an insignificant decrease, maintaining the overall recovery since around 2013 of the multidecadal decline since 1973.

This year an other-worldly topic is included in the single sidebar, discussing what is known about the weather and climate on a different planet, Mars. Sidebar 2.1 explores how the meteorological state of Mars is observed and the information that a satellite reanalysis product gives on this dry and cold world, along with the events of the 2015–17 Martian year.

Time series and anomaly maps for many variables described in this chapter are shown in Plates 1.1 and 2.1, respectively. Many sections refer to online figures that can be found here: http://dx.doi.org/10.1175/2017BAMSStateoftheClimate.2.

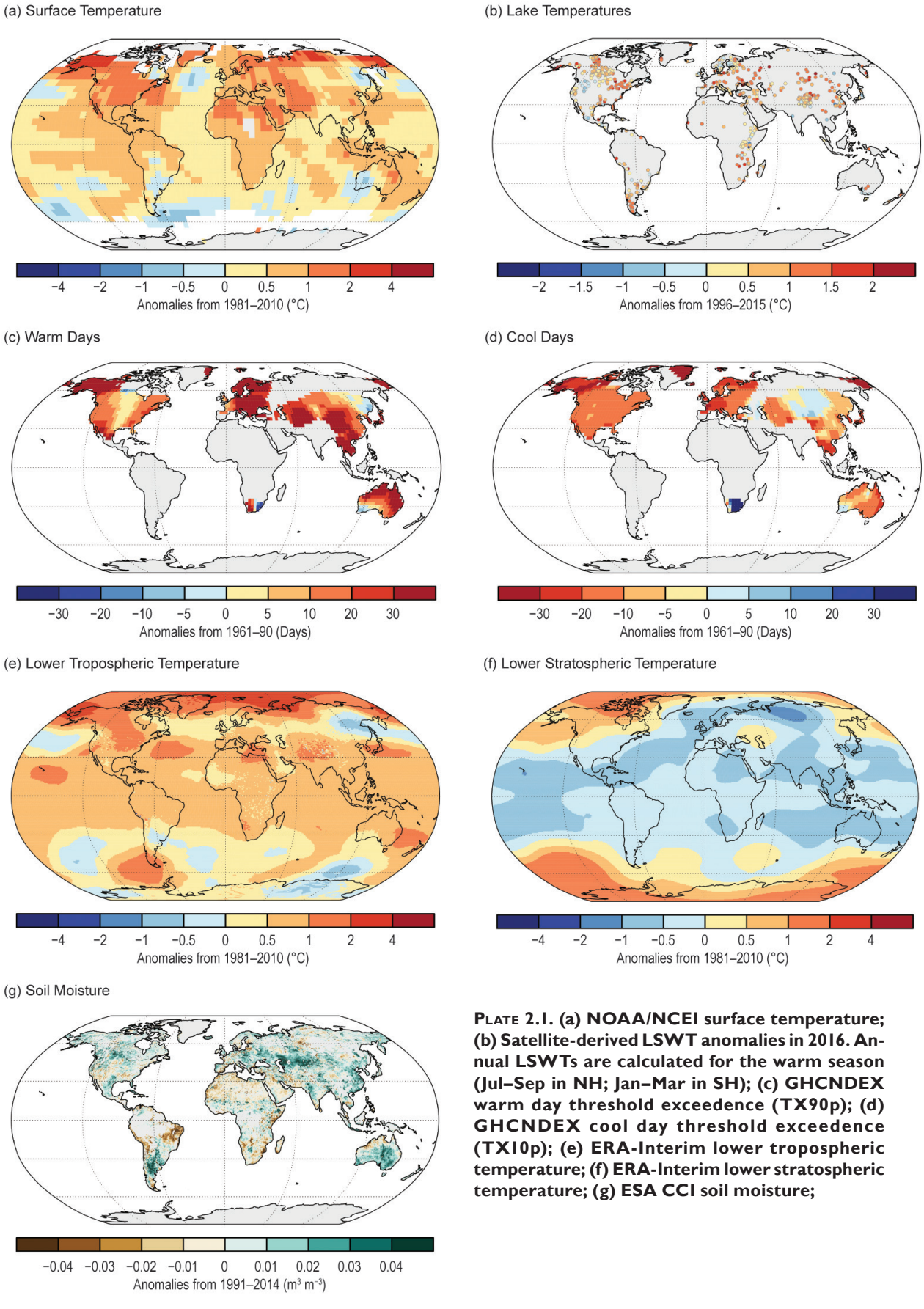

Plate 2.1. (a) NOAA/NCEI surface temperature; (b) Satellite-derived LSWT anomalies in 2016. Annual LSWTs are calculated for the warm season (Jul–Sep in NH; Jan–Mar in SH); (c) GHCNDEX warm day threshold exceedence (TX90p); (d) GHCNDEX cool day threshold exceedence (TX10p); (e) ERA-Interim lower tropospheric temperature; (f) ERA-Interim lower stratospheric temperature; (g) ESA CCI soil moisture;

(h) Terrestrial Water Storage

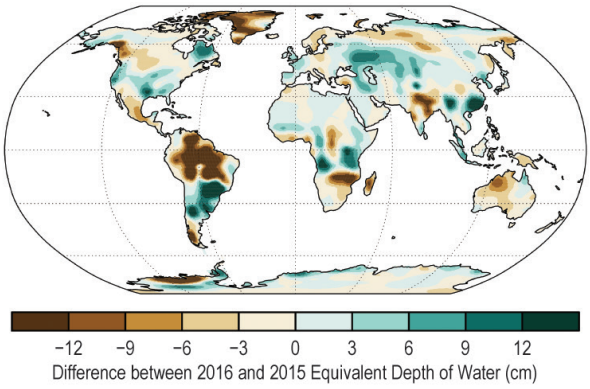

(i) Precipitation

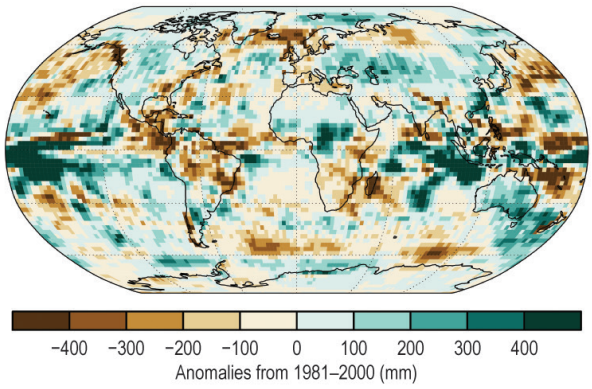

(j) Runoff

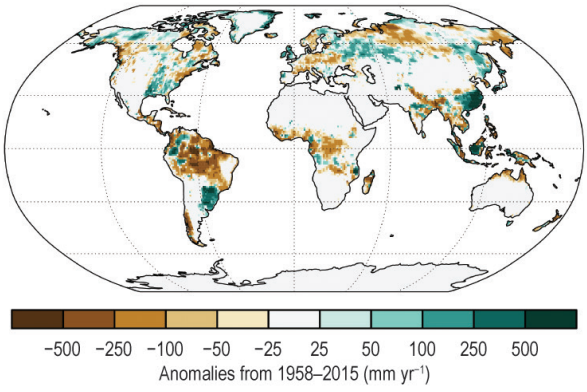

(k) River Discharge

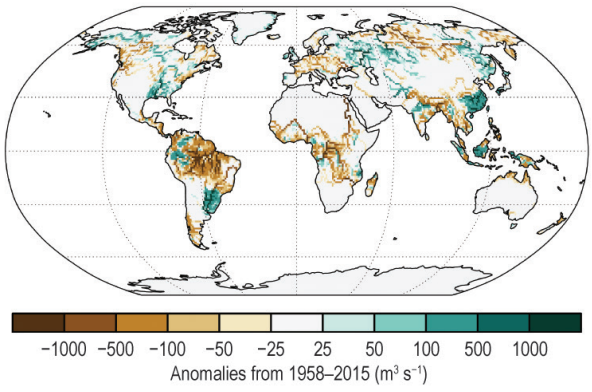

(l) Surface Specific Humidity

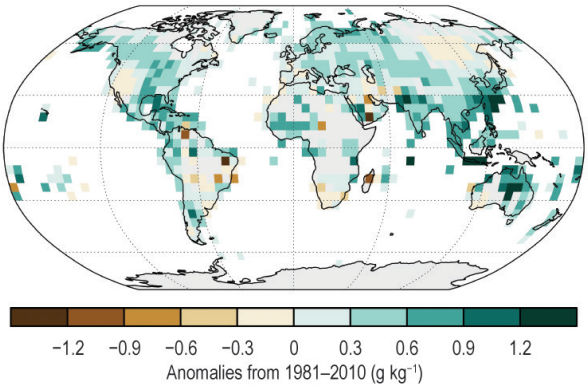

(m) Surface Relative Humidity

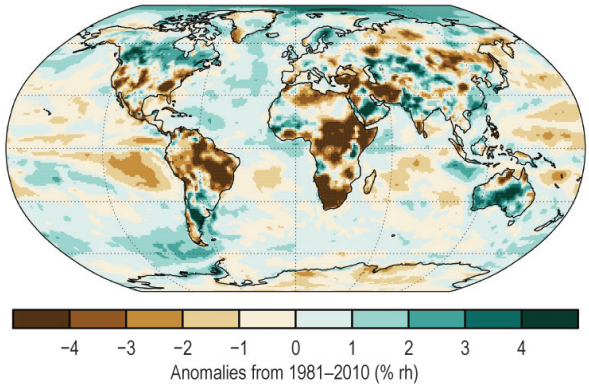

(n) Cloudiness

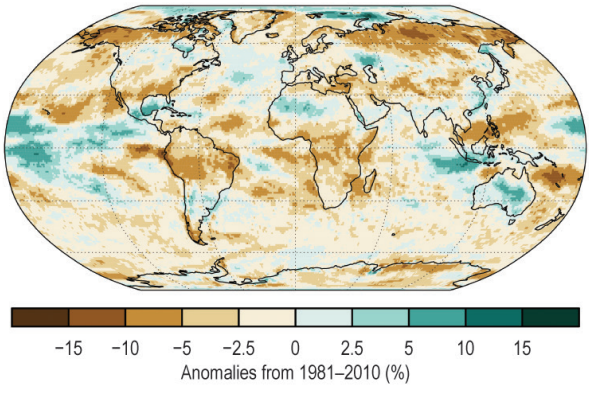

Plate 2.1. (cont.) (h) GRACE 2016 difference from 2015 water storage; (i) GPCP precipitation; (j) ELSE system runoff; (k) ELSE system river discharge; (l) HadISDH land surface specific humidity; (m) ERA-Interim surface relative humidity; (n) PATMOS-x/AVHRR cloudiness;

(o) Upper Tropospheric Humidity

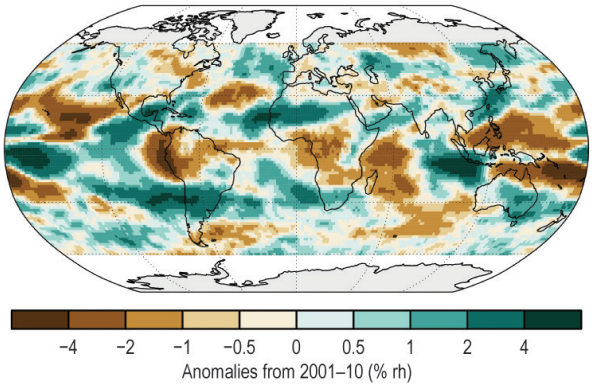

(p) Total Column Water Vapor

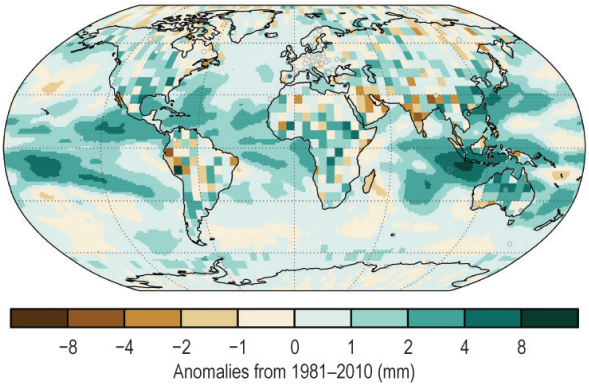

(q) Drought

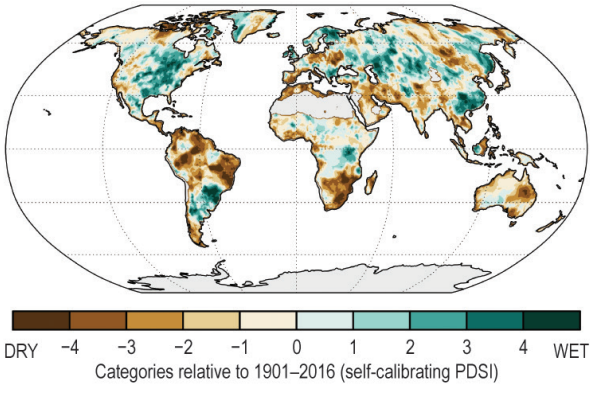

(r) Global Land Evaporation

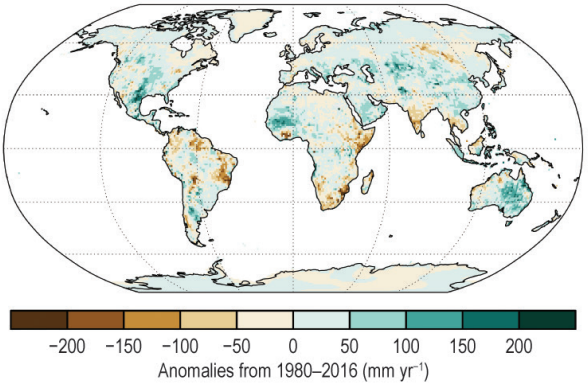

(s) Stratospheric (Total Column) Ozone

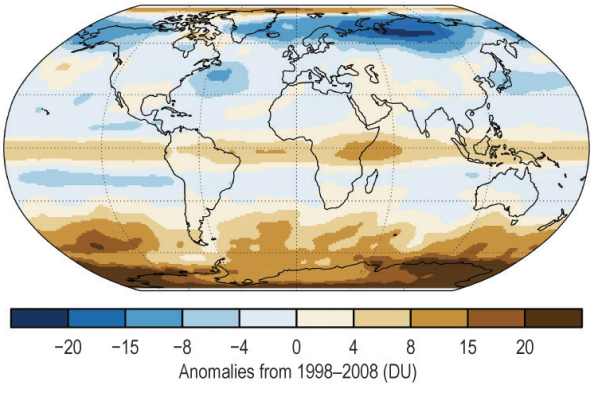

(t) Upper Air (850-hPa) Winds

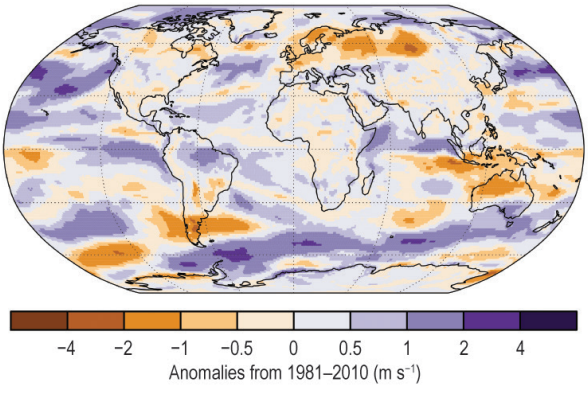

(u) Surface Winds

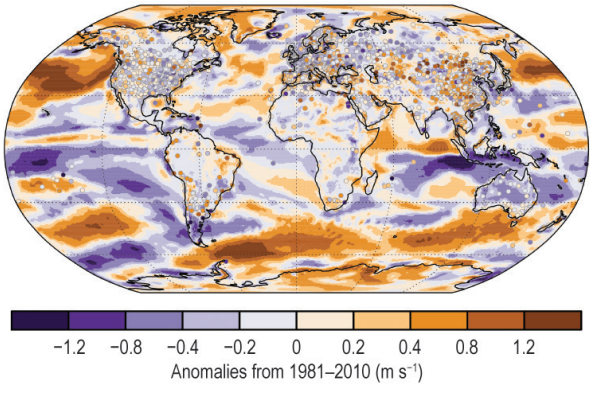

Plate 2.1. (cont.) (o) Microwave radiometer upper tropospheric humidity; (p) Microwave radiometer retrievals (ocean), COSMIC GPS-RO data (land), and GNSS (circles, land) total column water vapor; (q) scPDSI drought annual average 2016 anomaly; (r) GLEAM Land evaporation anomalies for 2016; (s) GOME-2 [using GOME, SCIAMACHY, and GOME-2 (GSG) for the climatology] stratospheric (total column) ozone; (t) ERA-Interim 850-hPa wind speed; (u) MERRA-2 (worldwide grids), Had-ISD (points, except Australia), CSIRO (points, Australia) surface wind speed;

(v) Sea Level Pressure

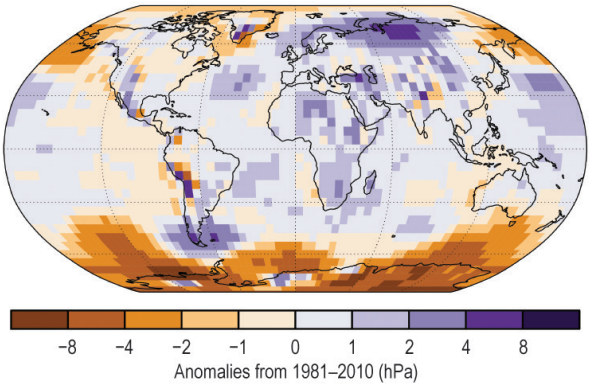

(w) OMI/MLS Tropospheric Column Ozone

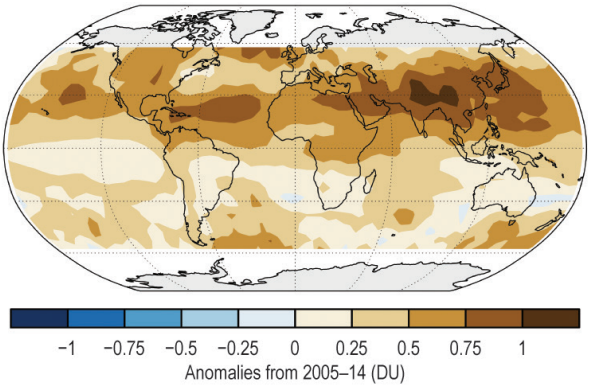

(x) Total Aerosol

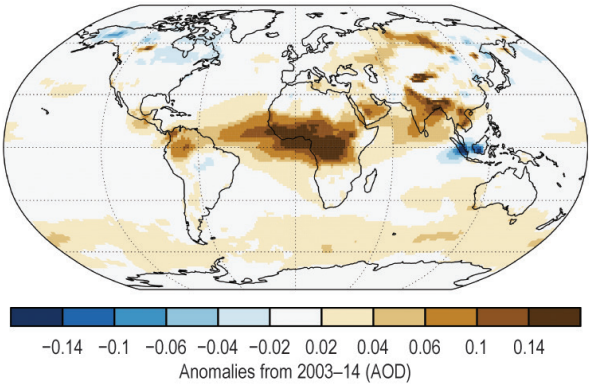

(y) Dust Aerosol

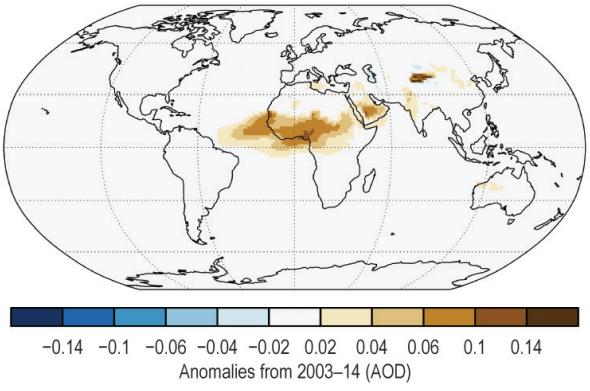

(z) Biomass Burning Aerosol

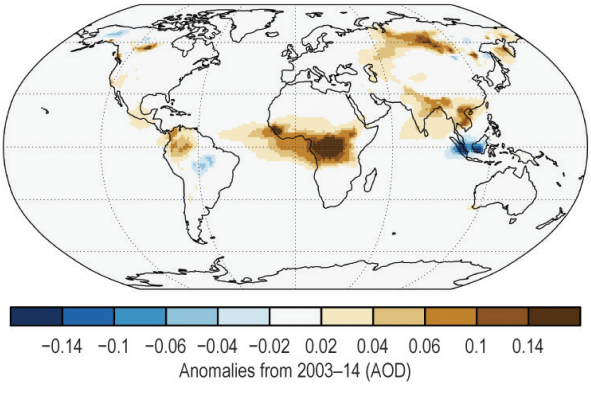

(aa) Fraction of Absorbed Photosynthetically Active Radiation

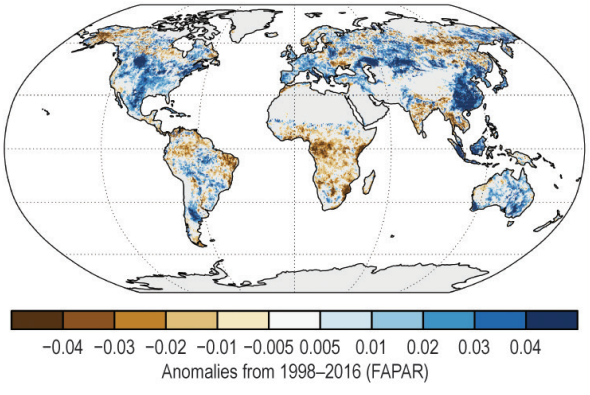

(ab) Land Surface Albedo in the Visible

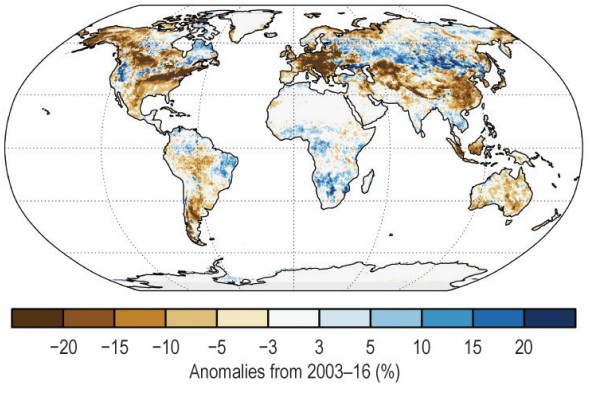

Plate 2.1. (cont.) (v) HadSLP2r sea level pressure; (w) Tropospheric ozone; (x) CAMS total aerosol optical depth; (y) CAMS aerosol optical depth from dust; (z) CAMS aerosol optical depth from biomass burning; (aa) SeaWiFS/MERIS/MODIS fraction of absorbed photosynthetically active radiation (FAPAR); (ab) Surface visible albedo from MODIS white sky broadband;

(ac) Land Surface Albedo in the Near-Infrared

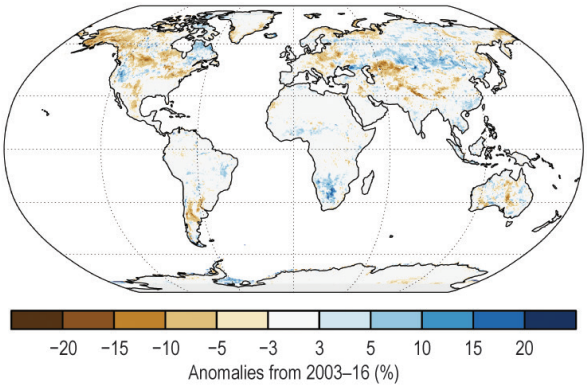

(ad) Carbon Emissions from Biomass Burning

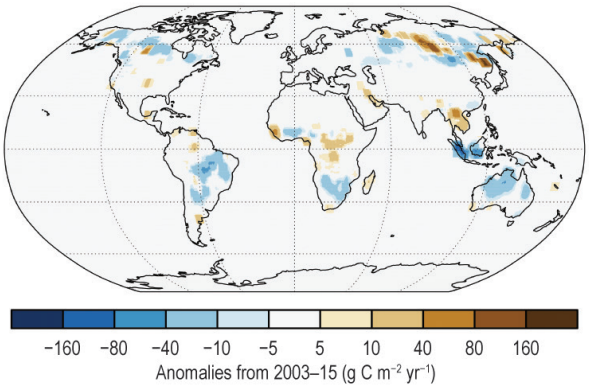

(ae) Carbon Monoxide

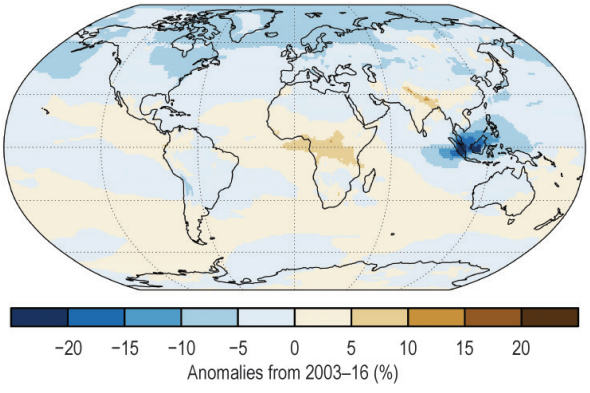

Plate 2.1. (cont.) (ac) Surface near-infrared albedo from MODIS white sky broadband; (ad) GFASv1.3 carbonaceous emissions from biomass burning; (ae) CAMS total column CO anomalies.

b. Temperature

1) Global surface temperatures—A. Sánchez-Lugo, C. Morice, P. Berrisford, and A. Argüez

For the third consecutive year, a new global surface temperature record was set. The 2016 global land and ocean surface temperature was 0.45°–0.56°C (Table 2.1) above the 1981–2010 average. This surpasses the previous record set in 2015 by 0.01°–0.12°C and the now third warmest year (2014) by 0.18°–0.25°C, according to four global independent in situ analyses (NASA-GISS, Hansen et al. 2010; HadCRUT4, Morice et al. 2012; NOAAGlobalTemp, Smith et al. 2008; JMA, Ishihara 2006). This was also the second consecutive year in which the annual global land and ocean temperature was more than 1°C above the mid-to-late nineteenth century average (a period in which temperatures are commonly taken to be representative of pre-industrial conditions) at 1.06°–1.21°C above average.

The global surface temperature analyses assessed here are derived from air temperatures observed at weather stations over land and sea surface temperatures (SST) observed from ships and buoys. While each analysis differs in methodology, leading to minor differences in temperature anomalies, all four analyses are in close agreement (Fig. 2.1). Differences between analyses are mainly due to how each methodology treats areas with little to no data and how each analysis accounts for changes in measurement methods [for more details see Kennedy et al. (2010); Hansen et al. (2010); and Huang et al. (2015)]. Conditions in higher latitudes are typically a major factor contributing to differences in the global average temperature estimates, with analyses that reconstruct anomalies in sparsely observed regions indicating either warmer or cooler anomalies than those analyses that do not. The ranges of temperature anomalies provided in this summary are ranges of best estimates for the assessed in situ analyses. These ranges do not include additional uncertainty information from each in situ analysis, which can be found in Table 2.1.

The presence of a mature strong warm phase El Niño at the start of 2016 combined with the ongoing long-term warming trend of the global climate system resulted in the highest global temperature departure from average since records began in mid-to late 1800s. Fifteen of the 16 warmest years on record have occurred since the beginning of the 21st century, with 1998 the only year from the 20th century among the top 16 years. The average rate of increase in the annual global surface temperature since 1901 is 0.78°–0.90°C century^{-1}. However, the rate of increase is nearly twice as great in the period since 1980

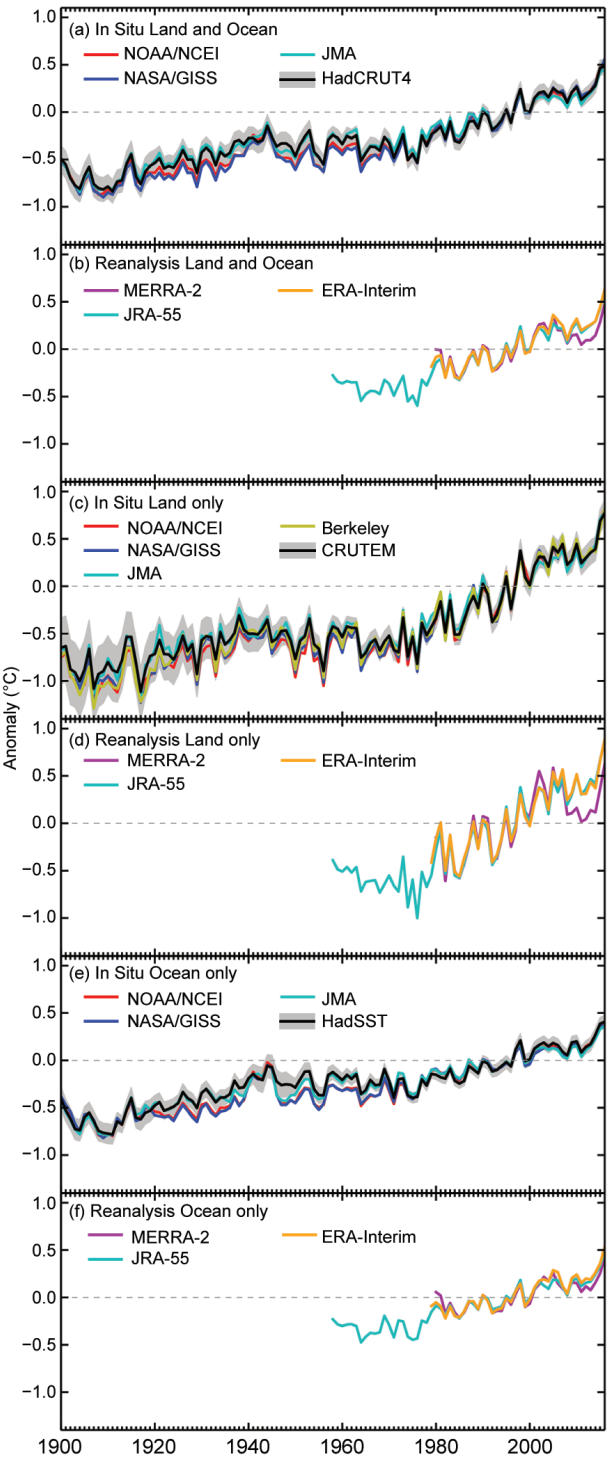

Fig. 2.1. Global average surface air temperature anomalies (°C; 1981–2010 base period). In situ estimates are shown from NOAA/NCEI (Smith et al. 2008), NASA-GISS (Hansen et al. 2010), HadCRUT4 (Morice et al. 2012), CRUTEM4 (Jones et al. 2012), HadSST3 (Kennedy et al. 2011a,b), JMA (Isihara 2006), and Berkeley Earth (Rohde et al. 2013). Reanalyses estimates are shown from ERA-Interim (Dee et al. 2011), MERRA-2 (Bosilovich et al. 2015; Gelaro et al. 2017) and JRA-55 (Ebita et al. 2011; Kobayashi et al. 2015).

Table 2.1. Temperature anomalies (°C) and uncertainties (where available) for 2016 w.r.t. the 1981–2010 base period. Temperature anomalies provided in the table are the central values of a range of possible estimates. Uncertainty ranges are represented in terms of a 95% confidence interval. For ERA-Interim, the values shown are the adjusted 2-m temperature anomalies. Note that the land values computed for HadCRUT4 used the CRUTEM.4.5.0.0 dataset (Jones et al. 2012), the ocean values were computed using the HadSST.3.1.1.0 data set (Kennedy et al. 2011a,b), and the global land and ocean values used the HadCRUT4.5.0.0 data set.

Global	NASA–GISS	HadCRUT4	NOAA-Global Temp	JMA	Berkeley	ERA-Int
Land	+0.81	+0.77 ± 0.13	+0.81 ± 0.15	+0.80	+0.82	+0.86
Ocean	+0.37	+0.41 ± 0.07	+0.39 ± 0.16	+0.36	—	+0.53
Land and Ocean	+0.56 ± 0.05	+0.48 ± 0.08	+0.50 ± 0.15	+0.45	—	+0.62

(1.3°–1.7°C century^{-1}). From 1891 to 1980 a new temperature record was set on average every 8–11 years, depending on the assessed in situ dataset. Since 1981, a new temperature record has been set every three to four years on average. However, having three consecutive years (2014, 2015, and 2016) set a new global surface temperature record is unusual. The question is, how unusual is it?

To estimate the probability of the most recent three years consecutively setting records, a large number (10 000) of plausible time series of globally averaged temperatures was generated by Monte Carlo simulation, whereby scenarios are created that exhibit similar statistical properties to the observed record. The probability is calculated as the percentage of the scenarios that show the last three years each setting a warm record. In accordance with Argüez et al. (2013), only the years since 1975 are simulated, as there is virtual certainty that all earlier years in the assessed in situ datasets were cooler than the most recent warm years. Statistical modeling suggests that randomized simulations of natural variability since 1975 is appropriate, and these random scenarios are superimposed on the trend since 1975. This approach results in a probability of 0.8%–1.5%. While the warming trend over the last few decades makes such a feat substantially more likely than if the global surface temperature were stationary, it is still quite remarkable for the most recent three years to set consecutive records.

Spatially, the year 2016 was characterized by much-warmer-than-average conditions across much of the world's surface, with the most notable warm anomalies across parts of the higher northern latitudes (Plate 2.1a; Online Figs. S2.1–S2.3). The only land areas with temperatures below their 1981–2010 averages were parts of eastern Canada, southern South America, western Australia, and parts of Antarctica and eastern Asia. Several locations across the southern oceans and the northwestern Pacific Ocean had below-average temperatures, along with persistent cooler-than-average conditions across the northern Atlantic Ocean south of Greenland.

Across the land areas, the globally averaged annual temperature was 0.77°–0.82°C above the 1981–2010 average. All six assessed datasets [including Berkeley Earth (Rohde et al. 2013)] rank the 2016 global land-only surface temperature as the highest on record, surpassing the previous record of 2015 by 0.08°–0.21°C. The globally averaged annual temperature over the ocean was the highest on record at 0.36°–0.41°C above the 1981–2010 average, surpassing the previous record set in 2015 by 0.01°–0.03°C (see Chapter 3b for a more detailed analysis). The ocean's temperature departure from average tends to be smaller than the land's temperature departure because it requires a larger amount of energy to raise the ocean's temperatures; subsequently the ocean heats up at a slower rate.

Global average surface air temperatures are also estimated using reanalyses, which blend information from a numerical weather prediction model with observations. Reanalysis produces datasets with uniform spatial and temporal coverage of the whole globe. According to ERA-Interim (Dee et al. 2011), the 2016 globally averaged, adjusted (see Simmons et al. 2017 and Simmons and Poli 2015 for details) 2-m temperature was the highest since records began in 1979. The temperature was 0.62°C above the 1981–2010 average (Table 2.1) and 0.19° and 0.27°C above the previous records set in 2015 and 2005, respectively.

ERA-Interim in 2016 also shows warmer-than-average conditions over many regions of the world (Online Fig. S2.3), particularly over the higher northern latitudes. According to ERA-Interim, 2016 was the warmest year on record over both land and ocean. The 2-m temperature over land was 0.86°C above average (0.21° and 0.3°C above the previous records

set in 2015 and 2007, respectively) and over the oceans it was 0.53°C above average (0.18° and 0.25°C above the previous records set in 2015 and 2005).

2) Lake surface temperature—R. I. Woolway, L. Carrea, C. J. Merchant, M. T. Dokulil, E. de Eyto, C. L. DeGasperi, J. Korhonen, W. Marszelewski, L. May, A. M. Paterson, A. Rimmer, J. A. Rusak, S. G. Schladow, M. Schmid, S. V. Shimaraeva, E. Silow, M. A. Timofeev, P. Verburg, S. Watanabe, and G. A. Weyhenmeyer

Observed lake surface water temperature (LSWT) thermal anomalies in 2016 are placed in the context of the recent warming observed in global surface air temperature (Section 2b1) by collating long-term in situ LSWT observations from some of the world's best-studied lakes and a satellite-derived global LSWT dataset. The period 1996–2015, 20 years for which satellite-derived LSWTs are available, is used as the base period for all LSWT anomaly calculations. Warm-season averages (July–September in the Northern Hemisphere and January–March in the Southern Hemisphere) are analyzed to avoid ice cover, in line with previous LSWT analyses (Schneider and Hook 2010; Hook et al. 2012; O'Reilly et al. 2015; Torbick et al. 2016; Woolway et al. 2016).

In situ observations from 48 lakes show an average warm-season LSWT anomaly of 1.0°C in 2016 (Fig. 2.2). The LSWT anomaly in Lake Baikal (Russia), the largest (by volume) and deepest of the world's freshwater lakes, was more than 2.3°C warmer than average in 2016. Comparable anomalies were observed in the North American Great Lakes, with an average anomaly of +2°C in 2016. Warming is not restricted to the largest lakes. For example, Harp Lake in Dorset, Ontario (Canada; surface area ~1 km^2) was 1.1°C warmer in 2016, compared to its 20-year average. High LSWT anomalies were also observed in central Europe, with LSWT anomalies >+0.5°C, and in Scandinavia, with the second largest lake in Sweden, Lake Vättern, having a LSWT anomaly of +1.3°C. Higher-than-average LSWTs were also evident in the Southern Hemisphere, with Lakes Rotorua and Taupo (New Zealand) showing an average LSWT anomaly exceeding +1°C, and the smaller lakes in the Bay of Plenty region (New Zealand) experiencing an average anomaly of +1°C in 2016.

Satellite-derived warm-season LSWTs generated within the Globolakes project (www.globolakes.ac.uk) for 681 lakes are used in this analysis to investigate global variations in LSWT. LSWTs were retrieved during the day using the retrieval methods of MacCallum and Merchant (2012) on image pixels filled with water according to both the inland water

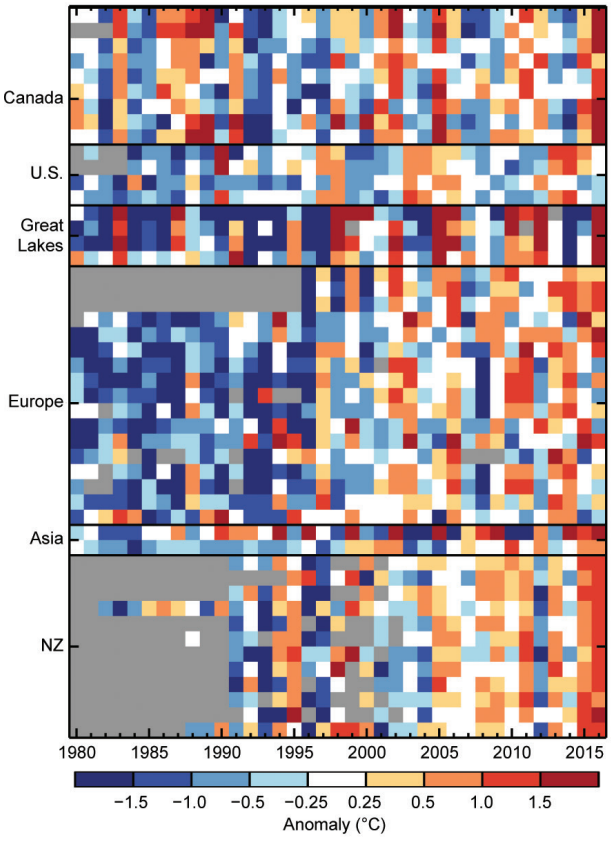

Fig. 2.2. In situ LSWT observations from 48 globally distributed lakes, showing the annually averaged warm season (Jul–Sep in NH; Jan–Mar in SH) anomalies (°C; relative to 1996–2015).

dataset of Carrea et al. (2015) and a reflectance-based water detection scheme (Xu 2006). The satellite temperatures represent mid-morning observations throughout the record. The observations were generated using data from the ATSR (Along Track Scanning Radiometer) series including ATSR-2 (1995–2003) and the Advanced ATSR (AATSR) (2002–12), extended with *MetOp*-A AVHRR (Advanced Very High Resolution Radiometer) (2007–16).

Globally and regionally averaged warming rates calculated from the satellite data show widespread warming tendencies in recent years (Fig. 2.3), being most evident in the extratropical Northern Hemisphere (>30°N), with a hemispheric average LSWT trend of +0.31°C decade^{-1} (p = 0.06). Warming (+0.21°C decade^{-1}, p = 0.07) is also found for the Southern Hemisphere (<30°S), but not in the tropics (30°N–30°S; p = 0.4). Using all available data, and weighting equally the northern, southern, and tropical regions, we obtain a global LSWT trend of +0.24°C decade^{-1} (p = 0.01) is obtained. Europe is the region showing the largest and most consistent LSWT warming trend (Fig. 2.3b), inline with previous studies (Hook et al. 2012), with a regional average LSWT

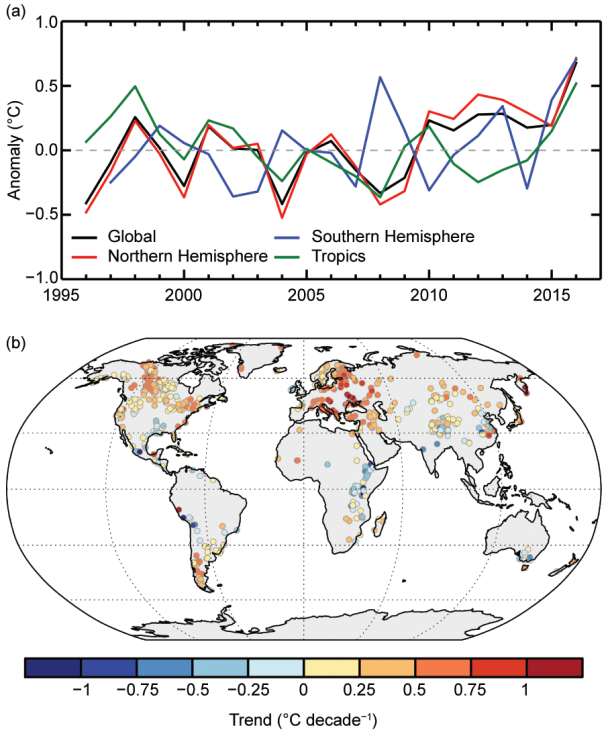

Fig. 2.3. Satellite-derived LSWT measurements from 681 lakes showing (a) global and regional annual average anomalies (°C) and (b) 1996–2016 LSWT trend (°C decade^{-1}). Annual LSWTs are calculated for the warm season (Jul–Sep in NH; Jan–Mar in SH) and LSWT trends are calculated on these anomalies.

trend of +0.55°C decade^{-1}. Other regions such as northeastern North America (+0.43°C decade^{-1}) and southern South America (notably those in southern Chile and Argentina; +0.3°C decade^{-1}) also experience significant regionally averaged warming.

In 2016, lakes were particularly warm with a global and equally weighted LSWT anomaly of +0.65°C. LSWT anomalies in the Northern Hemisphere (+0.72°C), Southern Hemisphere (+0.70°C), and the tropics (+0.52°C) were all anomalously high (Fig. 2.3a; Plate 2.1b) in 2016. About 83% of satellite-observed LSWT anomalies in 2016 were warmer than their 20-year average.

Global in situ and satellite measurements both point to LSWTs in 2016 being anomalously high, the warmest year in the 21-year record, reflecting the observed warming in global surface air temperature. Rising LSWTs have major implications for lake ecosystems (O'Reilly et al. 2003; Smol et al. 2005; Smol and Douglas 2007) and can, among other things, increase the occurrence of toxic cyanobacterial blooms (Kosten et al. 2012) and subsequently threaten water quality (Huisman et al. 2005). Warming of LSWT has been observed since 1996 and was particularly striking in 2016. If this trend continues, local economies dependent on lakes for drinking water, agricultural irrigation, recreation, and tourism are likely to be increasingly affected.

3) Land surface temperature extremes—R. J. H. Dunn, S. E. Perkins-Kirkpatrick, and M. G. Donat

As in the previous year, 2016 set the highest global annual mean temperature on record, and again, it experienced various anomalously high temperature events, especially with respect to minimum temperatures (Plates 2.1c,d). During 2016, Australia and western North America experienced the highest number of warm days and nights (defined below, using the 90th percentiles of the maximum and minimum daily temperatures) in the observational records dating back to 1951. Other than this, only a few regions exhibited record extreme temperatures throughout the year, but the globally averaged temperature for 2016 was the highest on record (see Section 2b1).

As in previous reports, the GHCNDEX dataset (Donat et al. 2013) is used to monitor global temperature extremes. GHCNDEX is a quasi-global gridded dataset of land-based observed temperature and precipitation extremes. A suite of temperature and precipitation extremes indices (Zhang et al. 2011) is first calculated for daily station time series from the GHCN-Daily archive (Menne et al. 2012), before interpolating the indices on global grids. As in previous reports (e.g., Donat et al. 2016), some of the indices fields have limited spatial coverage for 2016, especially those derived from minimum temperatures across central and eastern Asia, compared to those calculated from maximum temperatures.

Results are presented here for a number of the temperature indices in GHCNDEX: TX90p (frequency of warm days, defined as number of days above the seasonal 90th percentile of daily maximum temperatures; all percentiles in GHCNDEX were calculated over the 1961–90 base period), TX10p (frequency of cool days, defined as number of days with maximum temperatures below the seasonal 10th percentile), TN90p and TN10p (analogous definitions using the minimum temperature yielding the frequency of warm nights and cool nights, respectively). Some of the extreme temperature indices showed globally large anomalies during 2016, calculated relative to the 1961–90 average. For example, 2016 had the second largest number of warm days (TX90p; 1.76 times more than the 1961–90 climatology), behind 2015, and the fifth smallest number of cool days (TX10p; only about 0.65 times the climatology; Fig. 2.4) in the GHCNDEX record. The number of warm and cool nights showed record anomalies with 1.96 and

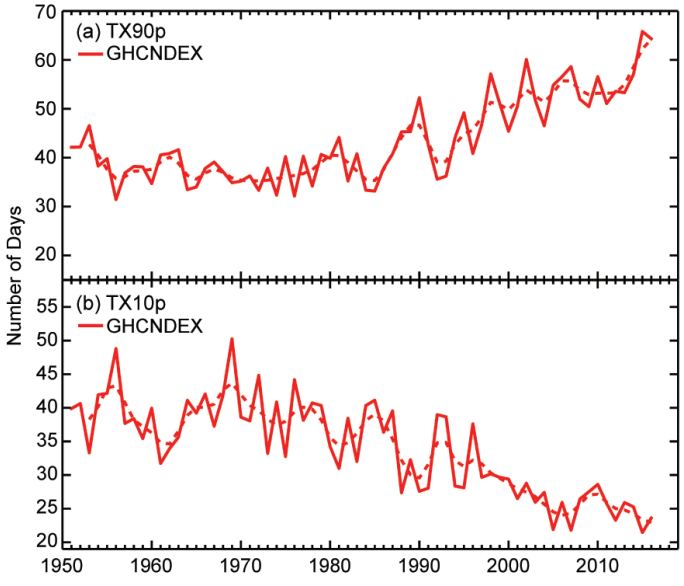

Fig. 2.4. Global average time series of annual local anomalies for (a) TX90p and (b) TX10p. Units: days.

0.40 times the climatology for TN90p and TN10p, respectively (see Online Fig. S2.5).

Several regions, including western North America, Europe, and large parts of Asia and Australia, experienced warm anomalies in TX90p, TX10p, TN90p, and TX10p in each season of 2016 consistent with above-average temperatures (Online Fig. S2.6). The ERA-Interim reanalysis product (Dee et al. 2011; Online Fig. S2.7) also shows, on an annual basis, warm anomalies in these indices in Africa and large parts of South America, where GHCNDEX lacks coverage, indicating that virtually all land areas have seen warm anomalies in these indices. The seasonal lowest minimum temperatures were the highest on record for all but the Northern Hemisphere summer (JJA). In contrast, a region that showed an excess of cool days and nights was through midlatitude Asia in autumn (SON; Online Fig. S2.6). The indices derived from maximum temperature are consistent with general warm anomalies, but, as in previous years, are more geographically variable, although with predominantly warm anomalies apart from midlatitude Asia in autumn.

The regions that experienced annual records are identified in Fig. 2.5. Record high numbers of warm nights were experienced in Australia, Alaska, and northwestern Canada. These regions also had record numbers of warm days, as did parts of central Asia. There were a number of notable regional anomalously high temperature events during 2016. In North America, Alaska experienced record numbers of warm and cool days (Plates 2.1c,d; Fig. 2.5), while extreme heat contributed to disastrous wildfire conditions in Fort McMurray in Canada (see Sidebar 7.1 for more details). The contiguous United States experienced extreme heatwaves in June and October, particularly over the Midwest, characterized by high minimum temperatures at the seasonal scale (see JJA and SON TN90p in Online Fig. S2.6). Europe sweltered through heatwaves during August and September, which, combined with a warm winter, contributed to its warm year (see DJF, TX90p and TN90p in Online Fig. S2.6, of which December 2015 has no effect on the 2016 value). During April and May, dry but intense heatwaves set in just before the monsoon, with a new national Indian high temperature record of 51.0°C set in Phalodi, Rajasthan. Countries in the Middle East also experienced extreme conditions during July, with temperatures well above 50°C recorded in Iran, Iraq, and Kuwait. These regions also experienced large annual exceedances of warm maximum and minimum temperatures (see ERA-Interim TN90p and TX90p in Online Fig. S2.7). South America experienced record warm months in January, February, and April, which contributed to the continent's second warmest year on record (see ERA-Interim TN90p and TX90p in Online Fig. S2.7). Australia experienced its warmest autumn on record where the national average temperature was 1.86°C above the seasonal average (TX90p and TN90p in Online Fig. S2.6).

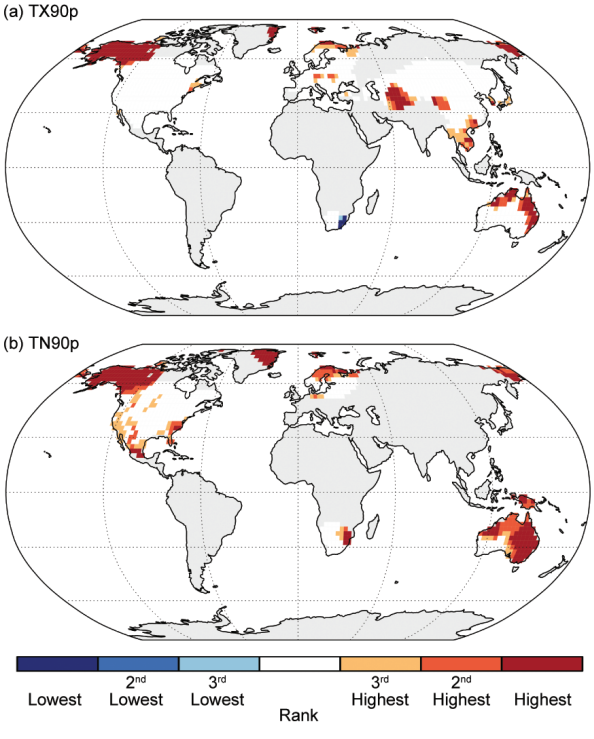

Fig. 2.5. Rank plot over the period 1951–2016 of TX90p and TN90p.

4) Lower and mid-tropospheric temperature—J. R. Christy

The bulk atmospheric response to the warm phase ENSO of 2015/16 dominated the global and tropical temperature values this year. The 2016 annual globally averaged temperature of the lower troposphere (LT: the bulk atmosphere below 10-km altitude or roughly the lower 70% by mass) was 0.45° to 0.75°C above the 1981–2010 mean, depending on the dataset. The year 2016 proved to be the warmest of the past 59 years in all datasets, exceeding the previous major warm phase ENSO (1998) by +0.02° to +0.38°C (Fig. 2.6). In general, the radiosonde-based datasets displayed greater warming relative to 1998, likely due to their more limited geographic coverage.

Direct measurements of the LT bulk temperature utilize radiosonde (balloon) datasets beginning in 1958 which are complemented by satellites since late 1978, described in Christy (2016). In addition to radiosonde and satellite estimates, three reanalysis products [ERA-I, MERRA-2, and JRA-55; see Christy (2016) for details] are examined with ERA-I used to provide spatial depictions of the temperature anomalies (Plate 2.1e; Fig. 2.7). The peak tropospheric warming in 2016 occurred in February with a rapid decline to June, and from then on was fairly stationary. This lag of a few months of peak warming relative to the surface, which peaked in late 2015, is typical (Christy and McNider 1994).

Regionally, warm anomalies occurred throughout the Arctic (north of 60°N). The midlatitude belts in both hemispheres featured both above- and below-average areas. The band from 30°N–30°S (half of the global area) was ubiquitously warmer than average (Plate 2.1e). The latitude–time depiction of the LT temperatures beginning in 1979 indicates major responses to the 2016 and prior warm phase ENSOs (1983, 1987, 1998, 2010, and 2016) with a protracted ENSO-like period 2002–06 (Fig. 2.7).

The global LT trend based on radiosondes (starting in 1958) is +0.16 ± 0.02°C decade^{-1} and based on both radiosondes and satellites (starting in 1979) is +0.16 ± 0.04°C decade^{-1}, where the range represents the variation among the datasets and thus serves as an estimate of structural uncertainty in Fig. 2.6. Major volcanic events in 1963, 1982, and 1991 contributed to cooler temperatures at those times that affected the early part of the LT record, especially in the satellite era, thus increasing the upward trend to some extent.

The layer centered on the midtroposphere (MT) is used for tropical atmospheric temperature monitoring and is able to utilize more independently constructed datasets. The top of the effective MT layer reaches higher into the stratosphere than LT, but in the tropics where the tropopause is approximately 16 km in altitude, there is only a slight influence

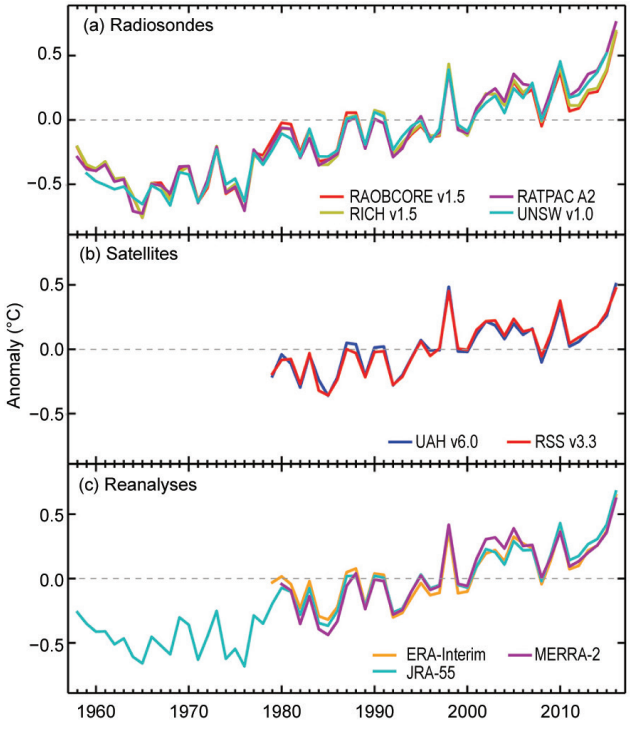

Fig. 2.6. Global average lower tropospheric temperature annual anomalies (°C; 1981–2010 base period for the MSU LT equivalent layer. (a) Radiosonde: RATPAC (Free et al. 2005), RAOBCORE and RICH (Haimberger et al. 2012) and UNSW (Sherwood and Nishant 2015). (b) Satellites: UAHv6.0 (Spencer et al. 2017) and RSSv3.3 (Mears and Wentz 2009). (c) Reanalyses: ERA-Interim (Dee et al. 2011), MERRA-2 (Bosilovich et al. 2015; Gelaro et al. 2017), and JRA-55 (Ebita et al. 2011; Kobayashi et al. 2015).

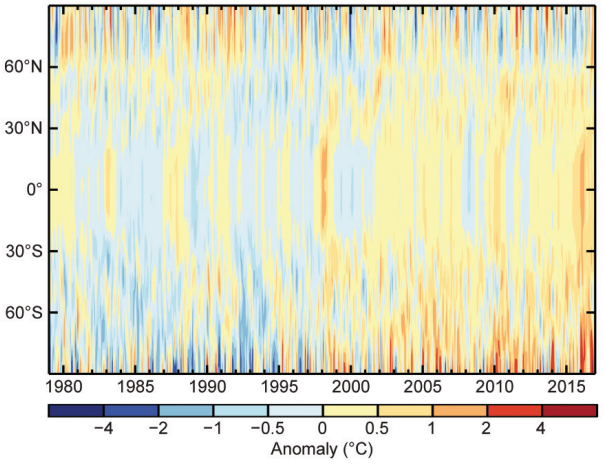

Fig. 2.7. Latitude–time cross-section of lower tropospheric temperature anomalies (°C) relative to 1981–2010 from ERA-Interim (Dee et al. 2011).

Table 2.2. Bulk atmospheric temperature trends (°C decade^{-1}). The tropical region spans 20°N–20°S. (Red indicates through 2015 only)

	Global LT		Tropics LT		Tropics MT	
Start Year:	**1958**	**1979**	**1958**	**1979**	**1958**	**1979**
Radiosondes						
RAOBCORE	+0.15	+0.14	+0.16	+0.14	+0.14	+0.10
RICH	+0.16	+0.16	+0.15	+0.16	+0.11	+0.12
RATPAC	+0.17	+0.20	+0.15	+0.15	+0.10	+0.09
UNSW	+0.17	+0.16	+0.15	+0.11	+0.10	+0.07
Satellites						
UAHv6.0	—	+0.12	—	+0.12	—	+0.08
RSSv3.3	—	+0.14	—	+0.13	—	—
RSSv4.0	—	—	—	—	—	+0.15
NOAAv4.0	—	—	—	—	—	+0.17
UWv1.0	—	—	—	—	—	+0.13
Reanalyses						
ERA-I	—	+0.14	—	+0.11	—	+0.10
JRA-55	—	+0.16	—	+0.13	—	+0.10
MERRA-2	—	+0.16	—	+0.14	—	+0.11

from the stratosphere on MT. Satellite monitoring of this layer is most sensitive to the mid- to upper troposphere, which in the tropics is the layer that typically responds most strongly to thermal forcing of any kind, for example, ENSO, enhanced greenhouse gases, etc. [See Christy (2016) for more details.]

Examining the various datasets of tropical MT trends (1979–2015 in Online Fig. S2.9), it is noted that the 2016 spike in tropical temperature due to the warm phase ENSO has increased trend values relative to those presented last year. Radiosonde values cluster closely around +0.11°C decade^{-1} while satellite results vary considerably from +0.08° (UAH) to +0.17°C (NOAA) decade^{-1}. The notable difference between UAH and the other satellite datasets is most evident over the lower latitude oceans (Online Fig. S2.9). This suggests the discrepancy is not due to corrections for diurnal (east–west) drift of the spacecraft, because these are negligible over the oceans, but to differing assumptions regarding basic calibration issues, primarily between 1990 and 2005. Understanding this discrepancy is an active area of research.

Tropical temperature trends are displayed in online Fig. S2.10 to demonstrate their vertical structure, as well as the MT bulk layer values at the top and in Table 2.2. Included are trends from the output of 102 CMIP-5 RCP4.5 model simulations (Flato et al. 2013), demonstrating the theoretical expectation of basic lapse-rate theory in which trends are magnified with altitude into the upper troposphere (National Research Council 2003; Christy 2014). The results (Online Fig. S2.10; Table 2.2) through 2016 continue to show that the observed MT trends tend to be below estimates anticipated from theory. The tropical surface trend (from NOAA/NCEI) is +0.13°C decade^{-1}. The median MT trend of all datasets examined here, including reanalyses, is +0.11°C decade^{-1}, less than that predicted by lapse-rate theory which indicates MT's trend would be a factor of about 1.4 greater than the surface, or +0.19°C decade^{-1}. The CMIP-5 Model mean surface trend is +0.19°C decade^{-1} and the mean MT trend is +0.27°C decade^{-1}, in agreement with lapse-rate theory.

5) Lower stratospheric temperature—C. Long and J. Christy

Radiosonde data, satellite data, and reanalyses agree that the global annual average temperature of the lower stratosphere layer (TLS) in 2016 was cooler than the previous three years (Fig. 2.8). This behavior is linked to lower stratospheric cooling associated with the strong El Niño and to the unusually persistent westerly phase of the quasi-biennial oscillation (QBO) winds in the tropics from 2015 through 2016 (Newman et al. 2016; Section 2e3). Enhanced upwelling and cooling in the tropical lower stratosphere

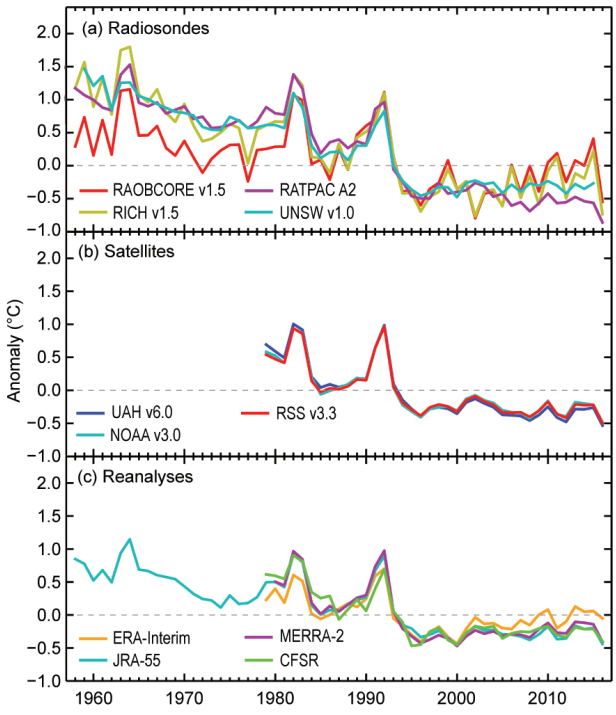

Fig. 2.8. Annual global TLS weighted temperature anomalies (°C) from the 1981–2010 climatology for radiosonde (RAOBCORE, RICH, RATPAC, and UNSW), satellite (UAH, RSS, NOAA/STAR), and reanalyses (CFSR, MERRA-2, ERA-I, and JRA-55). All show a cooler 2016 value.

are associated with El Niño conditions (Calvo et al. 2010; Randel et al. 2009). The QBO westerly phase is associated with a cooler middle and lower stratosphere in the tropics. The shear of westerlies over easterlies results in negative temperature anomalies from the thermal wind relationship. The TLS layer (MSU channel 4 and AMSU channel 9) retrieval is most sensitive to the lower stratosphere but with some influence from the upper troposphere as well as the middle and upper stratosphere. Positive temperature anomalies throughout the troposphere associated with the strong El Niño added complexity to this layer's temperature anomalies. To disentangle the influences of the QBO and ENSO on the TLS retrieval, Figs. 2.9a,b present monthly global temperature anomalies since 1980 at individual pressure levels in the upper troposphere and lower stratosphere, respectively, using the MERRA-2 reanalysis. The upper troposphere (400–200 hPa) contributes ~20% and the lower stratosphere (70–20 hPa) contributes ~42% towards the TLS weighted layer value. The remaining ~38% comes from the near-tropopause layer (150–100 hPa). Beginning in mid-2015, the lower stratospheric temperature record shows the negative temperature anomalies associated with the stratospheric influences of El Niño and the persistent QBO westerly phase.

Annual mean TLS layer anomalies for 2016 were positive in both polar regions and strongly negative in the tropics (Plate 2.1f; Online Fig. S2.11). The positive NH polar TLS anomalies are attributed to large positive anomalies in March due to a strong final stratospheric warming and to positive anomalies in November and December. In the SH, positive anomalies are associated with a warmer-than-average polar region during austral winter and spring. These higher temperatures also resulted in a smaller-than-normal ozone hole in 2016 (also see Chapter 6h). In the tropics, negative anomalies started in March and persisted throughout the rest of 2016, due to the temperature signal of the westerly phase of the QBO.

Figure 2.8 shows that the lower stratospheric temperature is highly impacted by the volcanic eruptions of El Chichón (1982) and Mt. Pinatubo (1991) but shows little trend since 1994. Offsetting impacts of increasing ozone (positive temperature anomalies) and increasing CO_2 (negative temperature anomalies) in the lower stratosphere may have led to this flat trend (Ferraro et al. 2015; Aquila et al. 2016). The various observation systems differ slightly from each other during this period since 1994. The four radiosonde datasets (RAOBCORE, Haimberger et al. 2012; RICH, Haimberger et al. 2012; RATPAC, Free et al. 2005; and

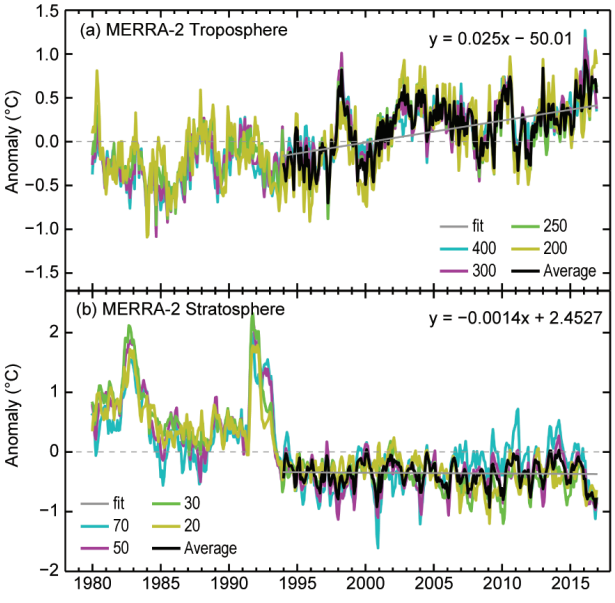

Fig. 2.9. MERRA-2 global temperature anomaly (°C) time series relative to 1981–2010 climatology at various (a) tropospheric and (b) stratospheric levels. The troposphere average anomaly is the unweighted average of (400-, 300-, 250-, and 200-hPa) values. The stratosphere average anomaly is the unweighted average of (70-, 50-, 30-, and 20-hPa) values.

UNSW, Sherwood and Nishant 2015) show different global trends and variability (Fig. 2.8): RAOBCORE and RICH are similar and highly variable during this period, but RATPAC and UNSW behave more like the satellite and reanalyses. However UNSW (for which 2016 data are still awaited) has a relatively flat trend, while RATPAC has a cooling trend. The three satellite records (RSS, Mears and Wentz 2009; STAR, Zou and Wang 2010; and UAH, Christy et al. 2011) have very minor differences in the global anomalies and show a relatively flat trend from 1994 to present. The four reanalyses (ERA-Interim, Dee et al. 2011; JRA-55, Kobayashi et al. 2015; MERRA-2, Bosilovich et al. 2017; and CFSR, Saha et al. 2010) show varying global trends since 1994. ERA-I and MERRA-2 have positive trends, while the CFSR and JRA-55 are near neutral. Reanalyses assimilate observations beyond the radiosondes and MSU and AMSU radiances, and the positive trends of ERA-I and MERRA-2 may be due to the usage of GPSRO data beginning in 2006.

Finally, trend variability with latitude is examined. Figs. S2.12a,b show the latitudinal annual trends (°C decade^{-1}) for the four reanalyses and the three satellite TLS datasets. There is a large range of trends in the tropics among the four reanalyses from a negative trend in JRA-55 to equally positive trends in ERA-I and MERRA-2, to the CFSR neutral trend. The satellite trends in the tropics are all slightly negative. All reanalyses and satellites are in agreement that at more southerly latitudes the trends becomes more positive. The four reanalyses differ from the satellites in the Northern Hemisphere mid- and high latitudes. The satellites all agree upon a negative trend in the midlatitudes while the reanalyses range from near-neutral to positive trends. The reanalyses all show a stronger positive trend in the northern high latitudes while the satellites have neutral or positive trends. Both the reanalyses and satellite data have smaller trend error in the tropics and large error in the mid- and high latitudes.

c. *Cryosphere*

1) Permafrost thermal state—D. A. Streletskiy, B. Biskaborn, J. Noetzli, J-P. Lanckman, V. E. Romanovsky, P. Schoeneich, N. I. Shiklomanov, S. L. Smith, G. Vieira, and L. Zhao

The Global Terrestrial Network for Permafrost (GTN-P) provides systematic long-term measurements of permafrost temperature and active layer thickness (ALT) worldwide, and it is part of the Global Climate Observing System under the umbrella of the World Meteorological Organization (WMO). The GTN-P recently launched a sophisticated data management system (http://gtnpdatabase.org), which includes 1350 temperature boreholes and 250 active layer measurement sites worldwide (Biskaborn et al. 2015) in order to assess the thermal state of the permafrost at the global scale.

Permafrost temperature in the Arctic increases along a north–south bioclimatic gradient from <–14°C in High Canadian Arctic to just below 0°C

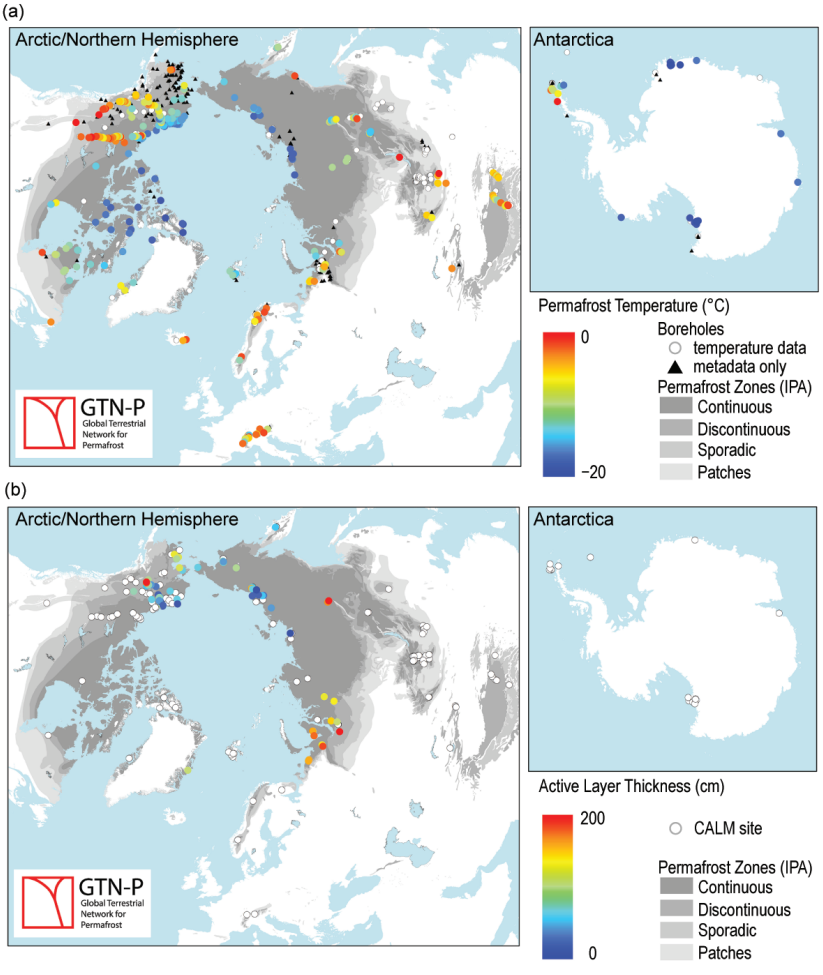

Fig. 2.10. (a) Permafrost monitoring boreholes showing permafrost temperature (°C) at zero annual amplitude depth in 2010–16 as reported by 314 sites. (b) Active layer thickness (cm) with data from 2016 as reported by 83 sites. (Source: Global Terrestrial Network for Permafrost.)

near the limits of permafrost distribution, but differences in site-specific conditions, such as snow depth, vegetation, and soil properties, complicate this general geographic trend (Fig. 2.10a). The permafrost temperature at 20-m depth in the European Alps is generally above −3°C and is above −1.5°C on the Tibetan Plateau. Continental Antarctica is characterized by permafrost temperature below −15°C, with the exception of Antarctic Peninsula where permafrost temperature is generally higher than −3°C.

Permafrost temperatures over the last decade have generally increased across the entire permafrost domain which is consistent with air temperature trends; however, there is considerable spatial and temporal variability. The highest increases in permafrost temperature are found in the High Arctic of Canada, North Slope of Alaska, and western Siberia and are pronounced in the regions with cold continuous permafrost in Russia and North America. In the sub-Arctic, where permafrost temperatures are relatively high and within 2°C of the freezing point, there has generally been little change in permafrost temperature over the last several years. More detailed description of the latest changes in permafrost temperature in the Arctic and sub-Arctic is provided in Chapter 5.

In Alpine permafrost areas most measurement sites show significant warming since 2009. Permafrost temperature in central Europe continued to increase over the last 15–30 years, and 2016 saw the highest temperature on record for 20-m depth, even though the air temperature was not a record there for the year (PERMOS 2016; PermaFRANCE: http://permafrance.osug.fr; Fig. 2.11a). Permafrost temperatures also continued to increase in central Asia. All observation sites in the Qinghai–Tibetan Plateau showed positive trends from 2005 to 2015; however, there is strong spatial variability. Ground temperature at 10-m depth has increased by 0.04°–0.49°C decade^{-1}, and at 20-m depth by 0.01°–0.28°C decade^{-1} (Fig. 2.11b).

In continental Antarctica, along the latitudinal transect in Victoria Land from Wright Valley to Terra Nova Bay, permafrost warming of about 0.5°C since 2008 has been found in the southern coastal site (Guglielmin et al. 2016). Farther north in Rothera, no apparent trend has been found. In the Western Antarctic Peninsula, ground cooling is significantly controlled by the longer lasting snow cover and warming events seem to be related to strong El Niño events (Oliva et al. 2017), which have resulted in fast warming pulses in the time series. In Antarctic Peninsula permafrost stabilized or even aggraded since 1999, primarily due to regional atmospheric cooling in the northern Ant-

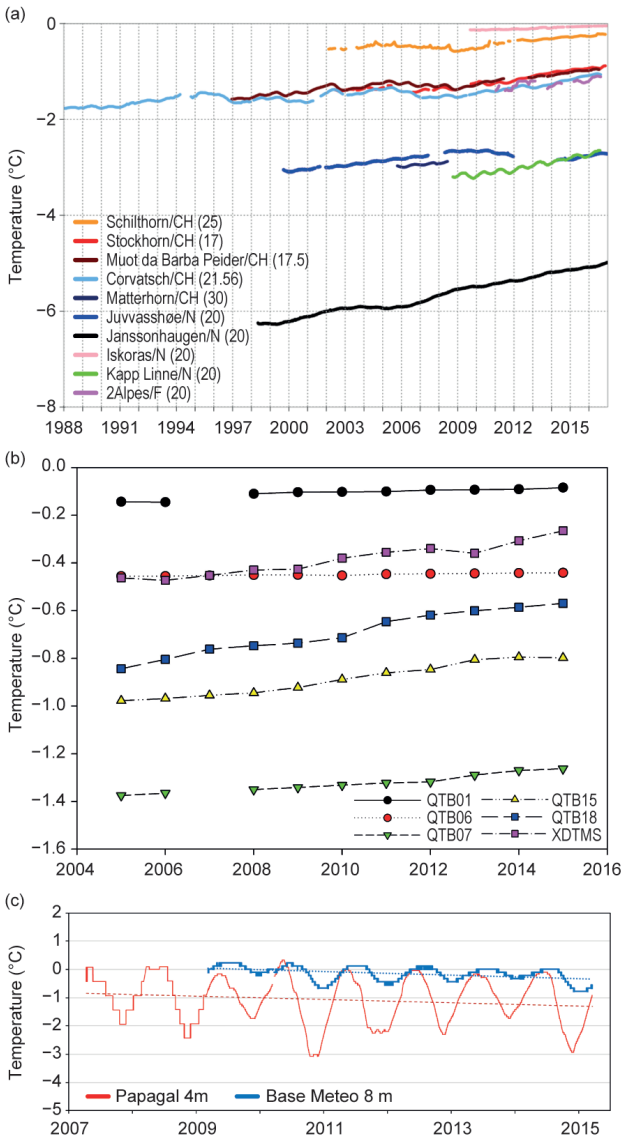

Fig. 2.11. Temperature (°C) measured in permafrost boreholes: (a) monthly mean values in central and northern Europe at approximately 20-m depth; (b) values along the Qinghai–Xizang Highway on the Tibetan Plateau at 20-m depth; and (c) in Levingston Island, Antarctica, at 4- and 8-m depth. (a) and (b) demonstrate permafrost warming with higher rate for colder permafrost, (c) demonstrates permafrost aggradation. (Sources: Swiss Permafrost Monitoring Network PERMOS; French Permafrost Monitoring Network CRYOBSCLIM/PermaFRANCE; Norwegian Meteorological Institute and the Norwegian Permafrost Database, NORPERM; Cryosphere Research Station on Qinghai-Xizang Plateau, CAS.)

arctic Peninsula at a rate of −0.47°C decade^{-1}, which followed significant warming that has been estimated at +0.32°C decade^{-1} for 1979–99 (Turner et al. 2016; Oliva et al. 2017). As a result, the active layer thickness in Deception Island and Byers Peninsula in the

South Shetlands off the northern tip of the Antarctic Peninsula, as well as in James Ross Island, has decreased (Ramos et al. 2017; de Pablo et al. 2017; Hrbáček et al. 2016). In some locations, such as Papagal, Hurd Peninsula (Livingston Island), ground cooling resulted in permafrost aggradation at sites where permafrost was previously unknown (Vieira et al. 2016; Fig. 2.11c).

The ALT is characterized by large spatial and temporal variability, so only sites that measure ALT at the spatially distributed grids and reported data in 2016 are presented on the global map (Fig. 2.10b). The ALT ranges from 0.3 m in the High Arctic regions to 2 m near the southern boundary of permafrost zone. However, ALT can be substantially higher in mountainous regions, where measurements are only possible by using interpolation from temperature boreholes. With the exception of a few sites, ALT experienced positive trends since the mid-1990s. The extremely warm summer of 2016 reinforced this trend; it has resulted in the highest recorded ALT at a majority of the sites located in interior Alaska and northwest Siberia. Close to maximum values of ALT were also observed at the North Slope of Alaska, Greenland, European Arctic, European North of Russia, and Russian Far East, and European Alps, where maximum values of ALT were reached in 2015. However, at several sites of the northwest Antarctic Peninsula, ALT has been stable or even decreased.

Table 2.3. Monthly and annual climatological information on NH and continental snow extent between Nov1966 and Dec 2016. Included are the numbers of years with data used in the calculations, means, std. dev., 2016 values, and rankings. Areas are in millions of km^2. Years 1968, 1969, and 1971 have 1, 5, and 3 missing months respectively, and are not included in the annual calculations. North America includes Greenland. Ranks are from most extensive (1) to least (ranges from 47 to 51 depending on the month).

	Years	Mean SCE	Std. Dev.	2016	2016 NH Rank	Eurasia Rank	N. Amer. Rank
Jan	50	47.1	1.6	48.8	9	13	6
Feb	50	46.0	1.8	43.5	48	47	38
Mar	50	40.5	1.9	37.2	49	46	48
Apr	50	30.5	1.7	27.9	50	46	40
May	50	19.2	2.0	16.3	47	42	49
Jun	49	9.6	2.4	5.6	47	48	47
Jul	47	4.0	1.2	2.6	42	41	42
Aug	48	3.0	0.7	2.6	29	37	23
Sep	48	5.4	0.9	5.7	18	20	13
Oct	49	18.3	2.7	23.0	3	3	2
Nov	51	34.1	2.1	36.9	5	2	40
Dec	51	43.7	1.9	45.4	8	12	11
Annual	**47**	**25.1**	**0.8**	**24.6**	**36**	**30**	**37**

2) Northern hemisphere continental snow cover extent—D. A. Robinson

Annual snow cover extent (SCE) over Northern Hemisphere (NH) lands averaged 24.6 million km^2 in 2016. This is 0.5 million km^2 less than the 47-year average (1967, 1970, 1972–2016) and ranks 2016 as having the 12th least extensive (or 36th most extensive) cover on record (Table 2.3; Fig. 2.12). It is almost identical to the 2015 mean extent. This evaluation considers snow over NH continents, including the Greenland ice sheet. SCE in 2016 ranged from 48.8 million km^2 in January to 2.6 million km^2 in July and August. Monthly SCE is calculated at the Rutgers Global Snow Lab from daily SCE maps produced by meteorologists at the National Ice Center (a US joint NOAA, Navy, and Coast Guard facility), who rely primarily on visible satellite imagery to construct the maps.

SCE across the Northern Hemisphere started 2016 off on the high side, ranking ninth in January for Eurasia (EU) and North America (NA) combined. This changed quickly, with February Northern Hemisphere extent ranking third lowest of the past 50 years. The dearth of snow cover continued throughout the late winter and spring, with rankings of first through fourth least extensive continuing throughout. Monthly NH anomalies of SCE were between 2.5 million km^2 and 4.0 million km^2 below average from February through June. During this period, SCE over the individual continents ranked 38th or

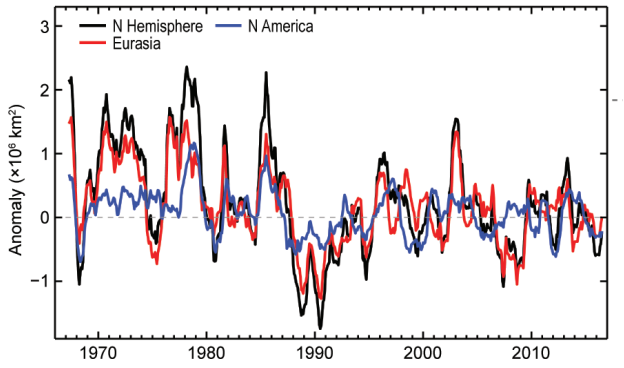

Fig. 2.12. Twelve-month running anomalies of monthly snow cover extent (× 10⁶ km²) over NH lands as a whole, and Eurasia and North America separately, plotted on the 7th month using values from Nov 1966 to Dec 2016. Anomalies are calculated from NOAA snow maps relative to 1981–2010. Mean hemispheric snow extent is 25.1 million km² for the full period of record. Monthly means for the period of record are used for 9 missing months between 1968 and 1971 to create a continuous series. Missing months fall between Jun and Oct; no winter months are missing.

lower. This continued the lower spring extents that have occurred in the second half of the satellite record compared to the first.

Much snow, as in the previous three years, arrived early over Northern Hemisphere continents during autumn 2016. October SCE was 4.7 million km² above average, ranking third most extensive. November came in as fifth most extensive and December eighth. Throughout these months, EU coverage was well above average, while over NA there was pronounced back and forth anomalies, with October second greatest, November 12th lowest, and December 11th most extensive.

SCE over the contiguous United States in January 2016 was seventh most extensive of the past half century but declined precipitously to only 38th largest in February and a meek 49th (of 50) in March. The extensive October 2016 SCE across NA were due almost entirely to record large extent in Canada. Meanwhile farther south, U.S. October cover ranked just 33rd largest. SCE remained at a 33rd largest ranking over the United States in November, before jumping to 13th most extensive in December.

Maps depicting daily, weekly, and monthly conditions, daily and monthly anomalies, and monthly climatologies for the entire period of record may be viewed at the Rutgers Global Snow Lab website (http://snowcover.org). Monthly SCE for the NH, EU, NA, contiguous US, Alaska, and Canada are also posted, along with information on how to acquire weekly areas and the weekly and monthly gridded products.

3) Alpine glaciers—M. Pelto

The World Glacier Monitoring Service (WGMS) record of mass balance and terminus behavior (WGMS 2015) provides a global index for alpine glacier behavior since 1894. Globally in 2015 mass balance was –1177 mm for the 40 long-term reference glaciers and –1130 mm for all 133 monitored glaciers. Preliminary data reported to the WGMS from Austria, Canada, Chile, China, France, Italy, Kazakhstan, Kyrgyzstan, Norway, Russia, Switzerland, and the United States indicate that 2016 is the 37th consecutive year without positive annual balances, with a mean of –852 mm for reporting reference glaciers.

Alpine glacier mass balance is the most accurate indicator of glacier response to climate and along with the worldwide retreat of alpine glaciers is one of the clearest signals of ongoing climate change (Haeberli et al. 2000). The ongoing global glacier retreat is currently affecting human society by raising sea level, changing seasonal stream runoff, and increasing geohazards (Bliss et al. 2014; Marzeion et al. 2014). Glacier mass balance is the difference between accumulation and ablation. The retreat is a reflection of strongly negative mass balances over the last 30 years (Zemp et al. 2015). Glaciological and geodetic observations, 5200 since 1850, show that the rates of early 21st century mass loss are without precedent on a global scale, at least for the time period observed and probably also for recorded history (Zemp et al. 2015). Marzeion et al. (2014) indicate that most of the recent mass loss (1991–2010) is due to anthropogenic forcing.

The cumulative mass balance loss from 1980–2015 is –18.8 m water equivalent (w.e.), the equivalent of cutting a 21-m thick slice off the top of the average glacier (Fig. 2.13). The trend is remarkably consistent from region to region (WGMS 2015). WGMS mass balance based on 40 reference glaciers with a

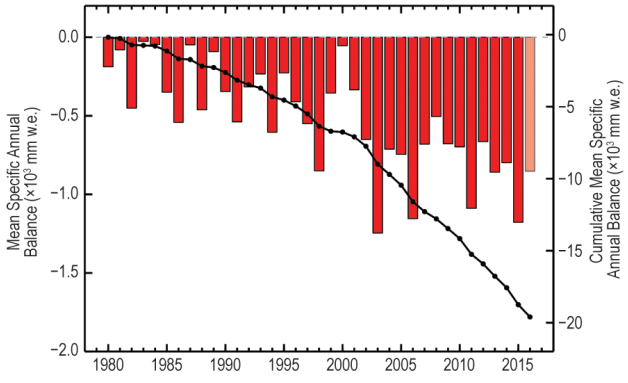

Fig. 2.13. Mean annual (red bars) and cumulative (black line) annual balance reported for the 41 reference glaciers to the WGMS (1980–2016). The data for 2016 are prelimimary only including 27 reference glaciers at the time of publication.

minimum of 30 years of record is not appreciably different from that of all glaciers at –18.3 m w.e.. The decadal mean annual mass balance was –228 mm in the 1980s, –443 mm in the 1990s, –676 mm for 2000s and –876 mm for 2010–16. The declining mass balance trend during a period of retreat indicates alpine glaciers are not approaching equilibrium, and retreat will continue to be the dominant terminus response. The recent rapid retreat and prolonged negative balances has led to some glaciers disappearing and others fragmenting (Fig. 2.14; Pelto 2010; Lynch et al. 2016).

Much of Europe experienced record or near-record warmth in 2016, thus contributing to the negative mass balance of glaciers on this continent. In the European Alps, annual mass balance has been reported for 12 glaciers from Austria, France, Italy, and Switzerland. All had negative annual balances with a mean of –1050 mm w.e. This continues the pattern of substantial negative balances in the Alps that drives continued terminus retreat. In 2015 in Switzerland, 99 glaciers were observed: 92 retreated, 3 were stable, and 4 advanced. In 2015 Austria observed 93 glaciers: 89 retreated, 2 were stable, and 2 advanced; the average retreat rate was 22 m.

In Norway, terminus fluctuation data from 28 glaciers with ongoing assessment indicate that from 2011–15 26 retreated, 1 advanced, and 1 was stable. The average terminus change was –12.5 m (Kjøllmoen et al. 2016). Mass balance surveys with completed results are available for seven glaciers; six of the seven had negative mass balances with an average loss of –380 mm w.e.

In western North America data have been submitted from 14 glaciers in Alaska and Washington in the United States, and British Columbia in Canada. All 14 glaciers reported negative mass balances with a mean loss of –1075 mm w.e. The winter and spring of 2016 were exceptionally warm across the region, while ablation conditions were close to average.

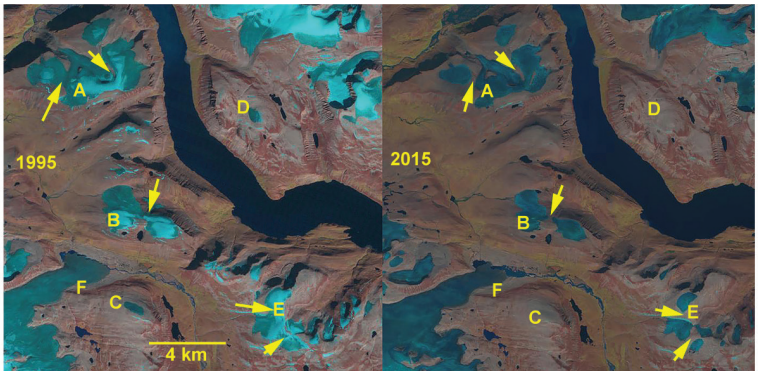

Fig. 2.14. Landsat images from 1995 and 2015 of glaciers in the Clephane Bay Region, Baffin Island (Canada). The yellow arrows indicate fragmentation. Glaciers at points C and D have dissappeared.

In the high mountains of central Asia five glaciers reported data from Kazakhstan, Kyrgyzstan, and Russia. Four of five were negative with a mean of –360 mm w.e. Maurer et al. (2016) noted that mean mass balance was significantly negative for all types of glaciers in the Eastern Himalaya from 1974 to 2006.

d. Hydrological cycle

1) Surface humidity—K. Willett, D. I. Berry, M. Bosilovich, and A. Simmons

Given the record warmth of the surface atmosphere and a strong El Niño at the beginning of the year (ongoing since 2014 in sea level pressure–based indices), concurrent high levels of surface moisture were expected in 2016. Over land and ocean all data products, including both in situ only and reanalyses, show 2016 as a record or near-record moist year in terms of specific humidity (q; Figs. 2.15a–d), well above the long-term average. As El Niño subsided to neutral/sporadic La Niña conditions the specific humidity also dropped substantially, albeit not sufficiently to lower annual averages appreciably.

Drivers of global land and ocean relative humidity are complex as reflected in the greater degree of differences between data products and between land and ocean estimates (Figs. 2.15e–h). Generally over land, relative humidity annual averages remained below the long-term average while ocean averages were close to average according to the reanalyses. Note that reanalyses currently provide the only up-to-date estimate of marine relative humidity. Over ocean, the reanalyses also show reasonable agreement with each other. Interestingly, the reanalyses show similar year-to-year variability to each other over land, remaining reasonably steady from around 2009 onwards, albeit at different average levels. The in situ-only HadISDH land product (Willett et al. 2013, 2014) differs somewhat with much more recovery from the recent drying period (~2000 to ~2012). It is too early to say whether the drying or the steadying/potential recovery is part of a long-term trend or something more transient.

Spatially, the pattern of specific humidity is far less El Niño–like than in 2015 (Plate 2.1l; Online Fig. S2.13), and relative humidity shows a general drier-than-average fingerprint over the tropical Pacific (Plate 2.1m; Online Fig. S2.14). Of note is the switch to strongly moister-than-average anomalies in specific humidity around northern Australia, South East Asia, southern China, and the western tropical Pacific

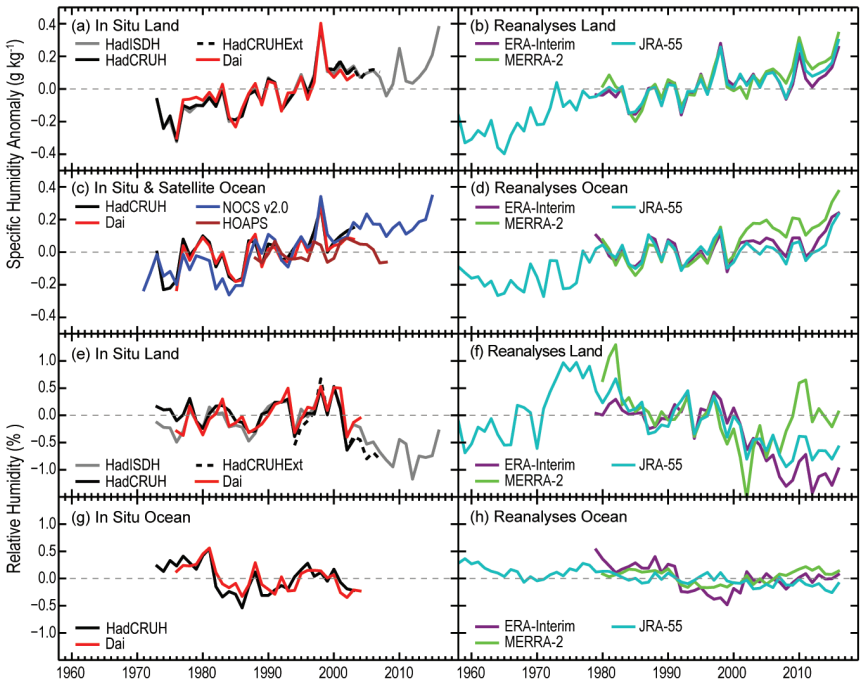

Fig. 2.15. Global average surface humidity annual anomalies (1979–2003 base period). For the in situ datasets 2-m surface humidity is used over land and ~10-m over the oceans. For the reanalysis 2-m humidity is used over the whole globe. For ERA-Interim ocean series only points over open sea are selected and background forecast values are used as opposed to analysis values because of unreliable use of ship data in producing the analysis. All data have been adjusted to have a mean of zero over the common period 1979–2003 to allow direct comparison, with HOAPS given a zero mean over the 1988–2003 period. ERA-Interim values over land have been spatially matched to the presence of HadISDH. [Sources: HadISDH (Willett et al. 2013, 2014); HadCRUH (Willett et al. 2008); Dai (Dai 2006); HadCRUHext (Simmons et al. 2010); NOCSv2.0 (Berry and Kent 2009, 2011); HOAPS (Fennig et al. 2012) and reanalyses as described in Fig. 2.1. Data provided by authors, A. Dai and S. Kobayashi.]

generally. The drier-than-average anomalies of 2015 over the North Atlantic have persisted but weakened, whereas the tropical Atlantic shows moister-than-average anomalies in 2016 as opposed to drier. There is reasonable agreement in the spatial patterns presented for specific humidity from ERA-Interim (Dee et al. 2011) and HadISDH (Willett et al. 2013, 2014) over land.

Estimates of surface humidity generally come from in situ observations from weather stations over land and ships and buoys over the oceans. Satellites and radiosondes also provide an estimate of specific humidity at the surface. All of these data require pre-processing to remove random errors and account for systematic biases. Additionally, in situ data suffer from large data gaps in space and time. The reanalysis products combine these observations with a weather forecasting model to provide a physically consistent and globally complete estimate. The model provides considerable skill in dealing with poorer quality observations although such observations and changes to observation streams can still affect the quality and homogeneity of the model output (e.g., Kent et al. 2014). In the case of ERA-Interim note that the background forecast dominates over ocean due to issues with the assimilation of ship data. Clearly, each product has various strengths and weaknesses and it is not straight forward to present a "best" estimate.

The availability of multiple independent (or methodologically independent at least) products provides valuable information about the likely uncertainty in estimates of surface humidity. Note that spatial coverage between the in situ estimates and the reanalyses is drastically different—with little in situ information available outside the Northern Hemisphere. Over land, ERA-Interim has been masked to match the coverage of HadISDH when creating the series plotted in Fig. 2.15. The NOCSv2.0 (Berry and Kent 2009, 2011) dataset has not been updated for 2016 due to the increasing sparseness of the marine observations and decrease in the quality of the observing system (e.g., Berry and Kent 2017). NOCSv2.0 has been included along with the other static products for historical comparison across the various estimates (Fig. 2.15).

2) Total column water vapor—C. Mears, S. P. Ho, J. Wang, H. Huelsing, and L. Peng

Total column water vapor (TCWV) rapidly peaked dramatically in early 2016 in response to the 2015/16 El Niño event (Fig. 2.16). Estimates are available from satellite-borne microwave radiometers over ocean (Wentz 1997; Wentz et al. 2007), COSMIC GPS-RO (Global Positioning System–Radio Occultation) over land and ocean (Ho et al. 2010a,b; Teng et al. 2013; Huang et al. 2013), and ground-based GNSS (Global Navigation Satellite System) stations (Wang et al.

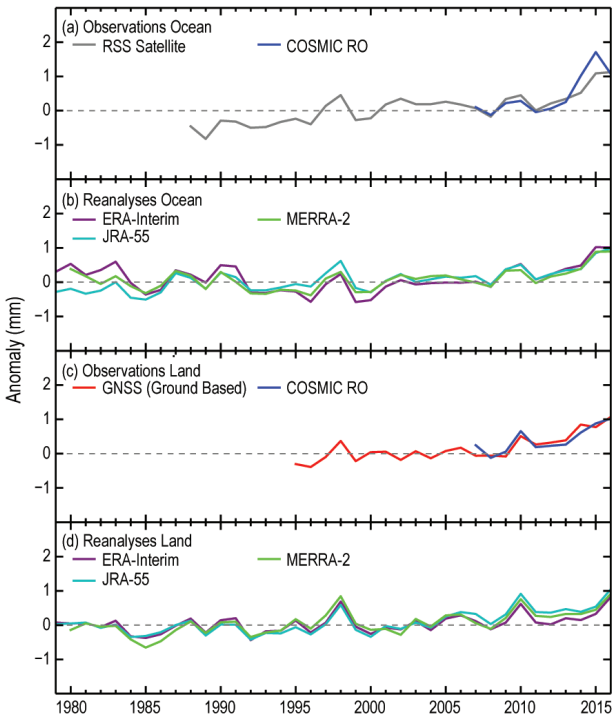

Fig. 2.16. Global mean TCWV annual anomalies (mm; relative to 1981–2010) for (a),(b) ocean only and (c),(d) land only for observations and reanalyses averaged over 60°N–60°S. Shorter time series are adjusted so that there is zero mean difference relative to the mean of the three reanalyses over the 2006–14 period.

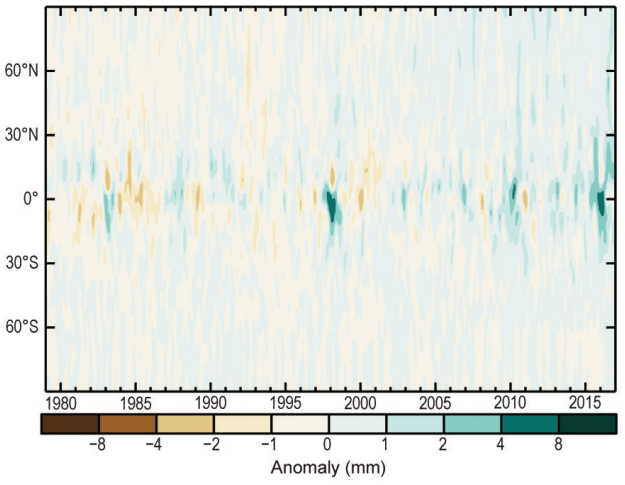

Fig. 2.17. Hovmöller plot of TCWV anomalies (mm; base period 1981–2010) including both land and ocean derived from the JRA-55 reanalysis.

2007; J. Wang et al. 2016) over land. An anomaly map for 2016 (Plate 2.1p) was made by combining data from these sources. Much of the globe showed small moist anomalies, except for small dry anomalies over regions of the Pacific Ocean (most notably off the Peruvian coast), the Southern Ocean, and some land areas. A large moist anomaly was present over the eastern tropical Indian Ocean, a region that also experienced a low wind speed anomaly in 2016 (see Plate 2.1u). The patterns in TCWV over the ocean is confirmed by COSMIC ocean measurements and by output from the MERRA-2, ERA-Interim, and JRA-55 reanalyses (not shown). Over land, the patterns from COSMIC are in agreement with the reanalysis output.

Over the ocean, the TCWV anomaly time series (Figs. 2.16a,b) from reanalysis and microwave radiometers show maxima in 1983, 1987/88, 1997/98, 2009/10, and 2015/16 associated with El Niño events. The 2015/16 anomaly is the largest recorded, particularly in the satellite radiometer data and the COSMIC data. This was caused by the large moist anomaly in the tropical Pacific Ocean, coupled with the preponderance of smaller moist anomalies in the rest of the world. The radiometer data show a discernible increasing trend while the different reanalysis products show a wide range of long-term trends. Minima are apparent in Northern Hemisphere winters during the La Nina events of 1984/85, 1988/89, 1999/2000, 2007/08, and late 2010 to mid-2012. Global water vapor has increased substantially since this last minimum at most latitudes (Fig. 2.17). The ocean-only COSMIC data are in general agreement with the reanalysis and radiometer data but show a larger peak for 2015 than the other data.

Over land average anomalies from the ground-based GNSS stations are used in place of the satellite radiometer measurements (Figs. 2.16c,d). The various reanalysis products, COSMIC, and GNSS are in good agreement, although as was the case for the oceans, the products more directly based on measurement show a larger increasing trend than the reanalyses over the past two decades. A land-and-ocean Hovmöller plot derived from JRA-55 (Fig. 2.17) indicates that the long-term increase in TCWV is occurring at all latitudes, with less variability outside the tropics. Previous strong El Niño events (1982/83 and 1997/98) showed pronounced drying events in the northern tropics that accompanied the moistening events on the equator and the southern subtropics. For the current El Niño this feature is much weaker, and the moist anomalies extend across most of the Northern Hemisphere.

3) Upper tropospheric humidity—V. O. John, L. Shi, E.-S. Chung, R. P. Allan, S. A. Buehler, and B. J. Soden

Water vapor is the principal greenhouse gas in the atmosphere and its changes contribute significantly to feedbacks in the climate system (Held and Soden 2000). Water vapor in the upper troposphere, while

insignificant by total mass when compared to the total column, constitutes a major part of the feedback because it is responsible for most of the tropospheric radiative cooling (Manabe and Möller 1961), and its radiative effect is proportional to relative changes in water vapor (John and Soden 2007).

Similar to last year's report (John et al. 2016), global scale monitoring of upper tropospheric humidity (UTH) is achieved using two independent satellite UTH datasets: (1) the infrared-based HIRS dataset (Shi and Bates 2011), and (2) the microwave-based UTH dataset (Chung et al. 2013). These datasets were constructed through careful bias corrections and intersatellite calibration. In these datasets, UTH represents a Jacobian weighted average of relative humidity in a broad layer which is roughly between 500- and 200-hPa but varies depending upon atmospheric humidity profile.

The area-weighted mean deseasonalized anomaly time series of UTH for 60°N–60°S is shown in Fig. 2.18. The anomalies are computed relative to the 2001–10 base period because the UTH dataset only begins in 1999. Positive relative humidity anomalies are observed in the second half of 2016, in contrast to the 2015 anomalies which were negative, indicating the shift from El Niño to La Niña conditions. A near-zero decadal trend in the upper tropospheric relative humidity time series indicates an increase in absolute (specific) humidity in step with the warming upper troposphere, and hence is consistent with a positive water vapor feedback (Chung et al. 2016). It is encouraging to see good agreement between the two independent datasets despite their differences in sampling: microwave data have an almost all-sky sampling whereas HIRS data sample mainly clear-sky scenes (John et al. 2011). Extreme anomalies for the HIRS time series arise from the sampling issues as

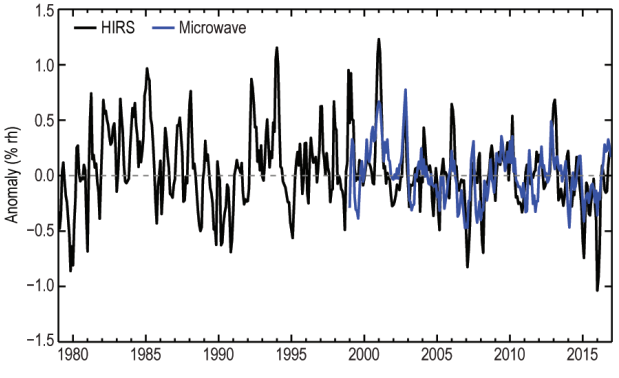

Fig. 2.18. Upper tropospheric humidity anomalies (%; 2001–10 base period) using HIRS (black) and microwave (blue) datasets. Time series are smoothed to remove variability on time scales shorter than 3 months.

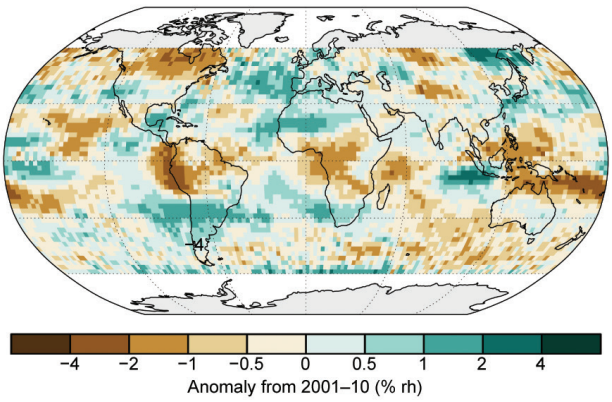

Fig. 2.19. Annual average UTH anomaly (%; 2001–10 base period) for 2016 based on the "clear-sky" HIRS UTH dataset.

demonstrated by John et al. (2011). The annual average UTH anomalies for 2016 relative to the 2001–10 base period (Plate 2.1o for microwave data; Fig. 2.19 for HIRS data) show moist anomalies over the central and eastern tropical Pacific and dry anomalies over the maritime continent which result from the still-strong El Niño during the first half of the year. Sampling of only clear-sky scenes by the HIRS dataset reduces the range of UTH between moist and dry regions, explaining the smaller magnitude of anomalies (~ ±2%) compared with the microwave dataset (~ ±5%).

4) Precipitation—R. S. Vose, R. Adler, A. Becker, and X. Yin

Precipitation over global land areas was above the 1961–90 average in 2016 (Fig. 2.20). However, there were two distinct "above-normal" story lines for the year depending upon the analyses considered. The first story line—one of slightly wetter-than-normal conditions—is supported by the Global Precipitation Climatology Centre (GPCC) dataset (Becker et al. 2013) and by the Global Historical Climatology Network (GHCN) dataset version 2 (Peterson and

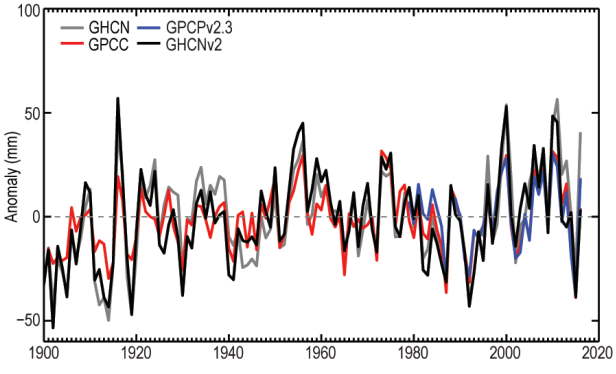

Fig. 2.20. Annual globally averaged precipitation anomalies (mm) over land areas relative to the 1961–90 base period (except GPCPv2.3, which is 1981–2000).

Vose 1997), both of which are based on surface stations. The 1961–90 base period is used here because it maximizes the number of stations available for a global analysis. The second story line—one of much-above-normal conditions—is supported by a new (experimental) version of GHCN that contains about five times as many stations as its operational counterpart (version 2), as well as by the Global Precipitation Climatology Project (GPCP) version 2.3 (Adler et al. 2003), which is based on both satellite data and surface stations and uses a different base period (1981–2010). (According to GPCP, precipitation over the global ocean surface in 2016 was much above the long-term average, as is typical of El Niño years.)

The annual anomaly map for 2016 (Plate 2.1i) shows a number of features at least partially related to the rapid evolution from an El Niño in the first few months of the year to La Niña conditions later on, with a near-neutral ENSO situation at the end of 2016. The central Pacific positive anomaly from the early months of the El Niño still dominated in the tropics, with a second strong positive feature in the eastern Indian Ocean. Over South America a negative anomaly covered the tropics (typical of El Niño), with a positive anomaly at higher latitudes. Much of North America, central Asia, northern Africa, and Australia experienced above-normal precipitation whereas Central America, western Europe, and southern Africa were below normal. Over the western United States the annual anomaly pattern shows some relief for the West Coast drought whereas the eastern U.S. generally had below-normal rainfall. The western Gulf of Mexico and the associated coastal areas also show a positive annual anomaly where significant floods occurred in Texas and Louisiana during the spring and early summer. Consistent with fading El Niño conditions, the strong positive anomalies over the tropical Pacific were less extreme than in 2015, as were the strong negative anomalies over the Maritime Continent. Broadly similar patterns are found for 2016 by the other precipitation datasets.

5) Cloudiness—M. J. Foster, S. A. Ackerman, K. Bedka, L. Di Girolamo, R. A. Frey, A. K. Heidinger, S. Sun-Mack, C. Phillips, W. P. Menzel, P. Minnis, and G. Zhao

Cloudiness measurements in the satellite era are dependent on the spectral sensitivity of the observing sensor. That said, year-to-year changes in global cloudiness among different sensors are generally in good agreement. Globally, cloudiness experienced only an incremental change (<0.2%) from that of 2015. This conclusion is based on several satellite cloud climatologies including PATMOS-x/AVHRR

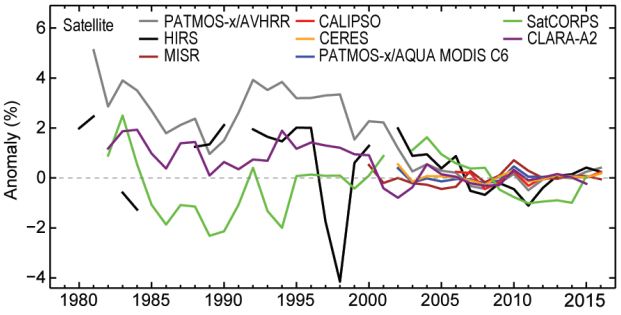

Fig. 2.21. Annual global cloudiness anomalies (%) for 1981–2016 (base period 2003–15, common to the satellite records excluding *CALIPSO*, where the entire record was used instead). Datasets include PATMOS-x/AVHRR, HIRS, MISR, *Aqua* MODIS C6, *CALIPSO*, CERES *Aqua* MODIS, SatCORPS, CLARA-A2, and PATMOS-x/*Aqua* MODIS.

(Pathfinder Atmospheres Extended/Advanced Very High Resolution Radiometer; Heidinger et al. 2014), *Aqua* MODIS C6 (Moderate Resolution Imaging Spectroradiometer Collection 6; Ackerman et al. 2008), *CALIPSO* (*Cloud-Aerosol Lidar and Infrared Pathfinder Satellite Observation*; Winker et al. 2007), CERES (Clouds and the Earth's Radiant Energy System) *Aqua* MODIS (Minnis et al. 2008; Trepte et al. 2010), MISR (Multi-angle Imaging SpectroRadiometer; Di Girolamo et al. 2010), HIRS (High Resolution Infrared Sounder; Wylie et al. 2005; Menzel et al. 2014), and PATMOS-x/*Aqua* MODIS. Several of these records—*Aqua* MODIS C6, *CALIPSO*, CERES *Aqua* MODIS, MISR and PATMOS-x/*Aqua* MODIS—are derived from polar-orbiting satellites flown as part of NASA's Earth Observing System. These records are shorter, the earliest starting in 2000, and do not yet suffer from issues such as satellite drift or intersatellite calibration. Figure 2.21 shows that since 2000 global cloudiness has been relatively stable. The average interannual change in cloudiness among all records represented was 0.3% after 2000 and 0.8% before 2000.

Currently it is not clear how much of this change is attributable to the influx of records taken from more modern satellites versus actual variability in cloudiness in the 1980s and 1990s. Strong El Niño events and the eruptions of El Chichón (1982) and Mount Pinatubo (1991) could explain positive cloudiness anomalies during this early period (a shift to more negative anomalies post-2000 can be seen in Figure 2.22), although it does not explain greater variability among the records. Of the records that extend back before 2000, three: PATMOS-x/AVHRR, CLARA-A2 (cloud, albedo and radiation dataset; Karlsson et al. 2017), and SatCORPS (satellite cloud and radiative property retrieval system; Minnis et al. 2016) are

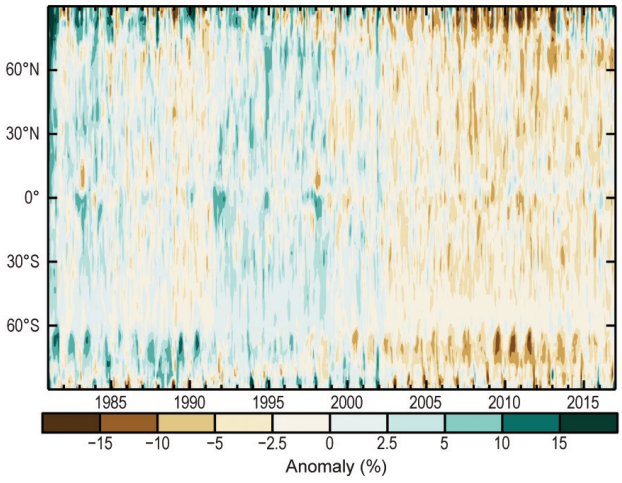

Fig. 2.22. Annual global cloudiness anomalies (%; 1981–2010 baseline) from the PATMOS-x/AVHRR record calculated using the same method as Plate 2.1n but zonally for each degree latitude.

derived from AVHRR instruments flown on NOAA POES and more recently the EUMETSAT MetOP series. Differences among these records can be attributed, in part, to which satellites were chosen for inclusion in the dataset and how the issue of diurnal drift was addressed (Foster and Heidinger 2013), as well as the auxiliary data used in the analyses. The fourth dataset to extend back before 2000, HIRS, has several gaps in coverage during this period and is more sensitive to the presence of thin cirrus clouds.

The emergence of several new global satellite cloud datasets in recent years has provided an opportunity to improve understanding of cloud feedbacks and their microphysical composition, and subsequently how they might be efficiently parameterized in numerical models. This is important as the role of clouds in the climate system is multifaceted. Clouds help modulate the global energy budget through cooling (reflection of incoming solar radiation) and warming (trapping outgoing terrestrial radiation) processes. Clouds affect the hydrological cycle through the storage and precipitation of atmospheric water. The structure of smaller clouds has historically been difficult to simulate on the spatial scales available to most general circulation models and, as such, have been a consistent source of uncertainty for climate prediction.

The global distribution of clouds is driven in part by large-scale circulation patterns such as ENSO. This can be seen in Fig. 2.22, as several of the stronger positive and negative anomalies correspond with phases of ENSO. The El Niño conditions in early 2016 resulted in enhanced large-scale convection in the central Pacific driven by higher-than-normal SSTs and convergence of low-level winds. This created positive maritime cloudiness anomalies in the central and eastern Pacific and corresponding negative anomalies over the western equatorial Pacific and Maritime Continent. This pattern can be seen clearly in online Fig. S2.15, although the El Niño pattern is apparent in the annual average as well, as seen in Plate 2.1n.

There were also several continental cloudiness anomalies significant at the 5% level relative to the 36-year PATMOS-x/AVHRR dataset, which frequently coincide with drought (negative anomalies) or flooding (positive anomalies) conditions. The significant anomalies in 2016 were almost all of the negative type. Alaska and portions of northern Canada experienced reduced cloudiness for much of the year, which coincided with unusually warm and dry conditions. For Alaska the largest negative cloudiness anomalies also corresponded with negative phases of the Arctic Oscillation. Portions of South America, encompassing Ecuador, Peru, parts of Bolivia, and the southern tip of Chile, also experienced significantly reduced cloudiness. The significant anomalies that covered the largest geographic area occurred in Siberia, which experienced reduced cloudiness for most of the year. Finally, southern Africa experienced reduced cloudiness during the boreal summer and autumn months.

6) River discharge and runoff—H. Kim

River discharge integrates the residual of precipitation (after evapotranspiration and reservoir storage) from headwaters to river outlets. It is important not only scientifically but also for human society because it is the most easily accessible renewable freshwater resource. It has, therefore, been monitored relatively long-term compared to other atmospheric and hydrologic variables. Still lacking, however, is a proper in situ gauge station network dense enough to provide a global monitoring service. Therefore, offline terrestrial simulation forced by atmospheric observations has been used to estimate global long-term variations. This is one of the most practical alternatives, at least until the Surface Water and Ocean Topography (SWOT) satellite begins to provide global river discharge observations in 2020.

A long-term (1958–2016) global offline land surface simulation has been performed by the ensemble land surface estimator (ELSE; Kim et al. 2009). The atmospheric boundary condition has been updated using the Japanese global atmospheric reanalysis (JRA-55; Kobayashi et al. 2015). To remove model precipitation bias in the JRA-55, the monthly observational Monitoring Product version 5 (Schneider et al.

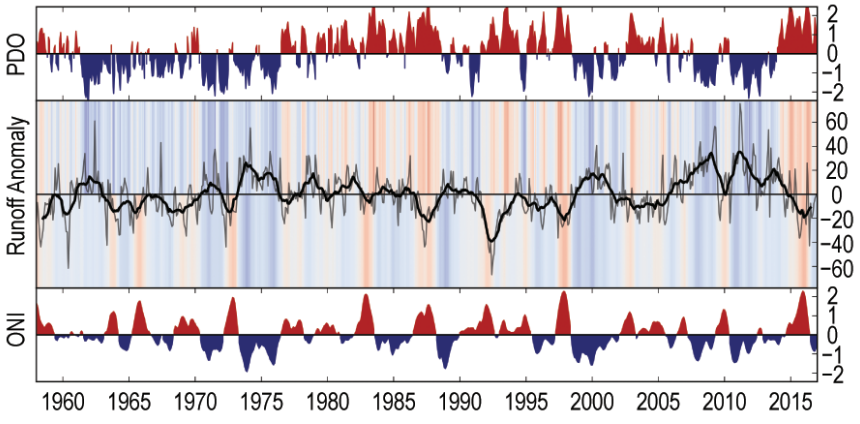

Fig. 2.23. Interannual variability of ONI (lower), PDO (upper), and global runoff (middle; mm; thick line is 12-month moving average). ONI and PDO are shaded red (positive phase) or blue (negative phase). Shading above and below the zero-line of global runoff is proportional to PDO and ONI, respectively.

2015) of the Global Precipitation Climatology Centre (GPCC) is used as the reference. The other parts of the simulation framework remain as the configuration from Kim (2016).

The global distributions of runoff (Plate 2.1j) and river discharge (Plate 2.1k) anomalies in 2016 show that large areas of South America, Africa, Europe, and Siberia were under significantly dry conditions. In particular, a number of global river basins, such as Amazon, Brahmaputra, Congo, Danube, Nile, Yenisei, and Zambezi have transported considerably lower amounts of freshwater than their climate normal to the oceans, while some basins including La Plata, Lena, Mississippi, and Yangtze were under wetter conditions than the long-term mean. The 59-year series of total terrestrial runoff anomalies is shown in Fig. 2.23 along with the oceanic Niño index (ONI) and Pacific decadal oscillation (PDO; Zhang et al. 1997) index. Both indices smoothed by a 12-month running mean are significantly anti-correlated ($R_{ONI} = -0.65$, $R_{PDO} = -0.55$) with similarly smoothed variations of monthly mean runoff. Dai et al. (2009) showed that the correlations between the global freshwater discharge and ENSO are significant for the rivers draining to the Atlantic ($R = -0.5$ with Niño3.4), Pacific ($R = -0.61$), and Indian ($R = -0.52$) Oceans (Dai et al. 2009). PDO is a pattern of Pacific climate variability similar to ENSO in character but which varies over a much longer timescale. Approximately 50% of the global discharge variability ($R = -0.69$) is reproducible when those two indices are used as the predictors in a multivariate linear regression. Therefore, reaching the lowest level of global mean runoff in more than a decade (Fig. 2.23) is likely associated with the strong 2015/16 El Niño. As shown in Fig. 2.24, the diminished global runoff, which had been evident since mid-2015, was alleviated from the boreal fall to the end of the year. However, South America and Africa had persistently deficient runoff, close to -2σ, through the entire year which may be a major cause of the low level of global runoff because the Amazon River, where the hydrologic cycle is largely controlled by ENSO (e.g., Zeng 1999), solely contributes to more than 15% and 70% of the global and South American freshwater discharge, respectively. Europe and North

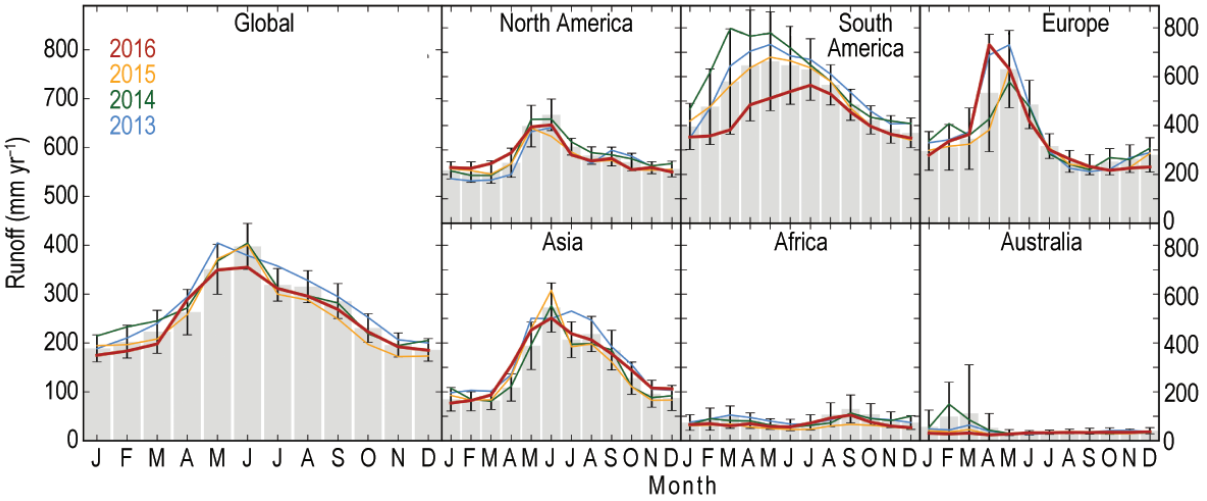

Fig. 2.24. Seasonal variations of global and continental runoff (mm) for 2013–16 (gray bar for 59-year climatology; error bars for 2v; colored lines for most recent 4 years).

America had excess runoff in early 2016 but then strong deficits from boreal summer onward. Asia and Australia ended 2016 with excess runoff. During the last four years, there has been large interannual variability, in both amplitude and phase, in South America, Europe, and Australia in boreal spring.

7) Groundwater and terrestrial water storage—M. Rodell, D. N. Wiese, and J. S. Famiglietti

Groundwater, soil moisture, surface water, snow, and ice compose terrestrial water storage (TWS). Groundwater varies more slowly than the surficial TWS components, but it commonly exhibits a larger range on multiannual timescales (Li et al. 2015). In situ groundwater data are only archived and shared by a few countries. Since 2002, however, the Gravity Recovery and Climate Experiment (GRACE; Tapley et al. 2004) satellite mission has been providing observations of TWS variations that approximate unconfined groundwater variations on seasonal and longer scales.

Changes in January–August mean TWS from 2015 to 2016 are plotted in Plate 2.1h as equivalent heights of water in cm. Beginning in 2011, certain GRACE instruments have been powered down during part of the orbital cycle in order to conserve battery life, including the last four months of 2016. TWS changes reflect the integrated effects of other hydroclimatic variables (see Plates 2.1g–r). The Amazon basin, which has the largest TWS fluctuations of any river basin, lost a huge amount of water in 2016 as a result of low precipitation (Sections 2d4, 2d8, 2d9). Somewhat balancing that, heavy rains greatly increased TWS in the southern half of South America, causing flooding and landslides near Sao Paolo in March. In general the rest of the world was more wet than dry. California enjoyed some relief from an historic drought, and the central and southern United States gained large amounts of TWS. A large area of western Russia also experienced TWS increases. Massive increases in TWS were associated with flooding in Angola (January–April), Myanmar (June–August), and southern China (June–July). Rains in east central Africa also increased TWS and the water level of Lake Victoria during the first half of the year (based on satellite altimetry; Birkett et al. 2011). Severe drought reduced TWS and caused food shortages in Madagascar, Mozambique, Zimbabwe, and neighboring countries. A region centered on Nepal was similarly afflicted, although continuing groundwater withdrawals for irrigation in northern India (Rodell et al. 2009; Panda and Wahr 2016) contributed to the observed signal. TWS also decreased in Mexico and northwest Australia. Significant reductions in TWS in Greenland, western Antarctica, southern coastal Alaska, and Patagonia represent ongoing ice sheet and glacier ablation, not groundwater depletion.

Figures 2.25 and 2.26 show time series of zonal mean and global deseasonalized monthly TWS anomalies from GRACE, excluding Greenland and Antarctica. The effects of droughts in Brazil, southern Africa, and Australia are clear in Fig. 2.25, as is the wetness in southern South America. Despite the massive Brazilian drought, by August global TWS had recovered substantially to −0.8 cm from a GRACE-period low of −2.8 cm in January 2016. That 2-cm increase in TWS (temporarily) offset about 7 mm of mean sea level rise.

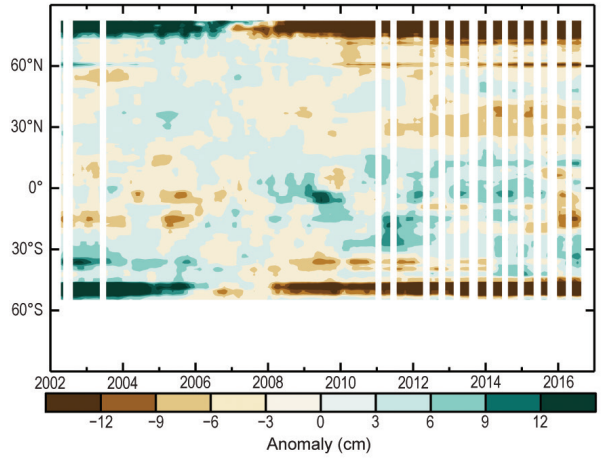

Fig. 2.25. GRACE zonal mean terrestrial water storage anomalies (cm, equivalent height of water; relative to 2005–10). White areas indicate months when data were unavailable.

8) Soil moisture—W. A. Dorigo, D. Chung, A. Gruber, S. Hahn, T. Mistelbauer, R. M. Parinussa, C. Reimer, R. van der Schalie, R. A. M. de Jeu, and W. Wagner

Satellite-based microwave radiometers and scatterometers can measure the moisture content of the

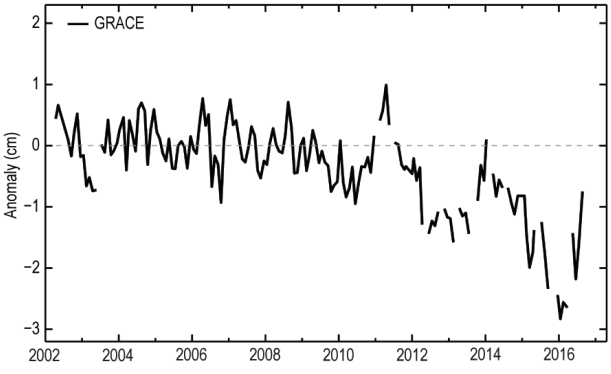

Fig. 2.26. GRACE global average terrestrial water storage anomalies in (cm, equivalent height of water; relative to 2005–10).

upper few centimeters of the soil. While dedicated soil moisture missions, such as NASA's Soil Moisture Active Passive (SMAP), are able to provide nearly contiguous global spatial coverage at daily time scales, as stand-alone missions they are too short for assessing soil moisture variability and change in a climatic context. The ESA Climate Change Initiative (CCI) bridges this gap by combining observations from a large number of historical and present-day passive and active microwave instruments (Liu et al. 2012; Wagner et al. 2012). The latest dataset combines 11 different sensors between late 1978 and December 2016 and now also includes data from the Soil Moisture Ocean Salinity (SMOS) mission (Dorigo et al. manuscript submitted to *Remote Sens. Environ.*). The dataset has been used for a wide range of applications (see Dorigo and de Jeu 2016; Dorigo et al. submitted,) and has been benchmarked against a large number of land surface models and in situ datasets (Albergel et al. 2013; Dorigo et al. 2015b; Fang et al. 2016; Loew et al. 2013). Based on the ESA CCI Soil Moisture (SM) dataset the yearly and monthly anomalies are computed here with respect to a 1991–2015 climatology.

For 2016, spatial anomaly patterns (Plate 2.1g) are markedly different from 2015, which was characterized by El Niño conditions throughout the year (Dorigo et al. 2016). Strong El Niño conditions continued into 2016, and aggravated drought conditions in the first months of the year in southern Africa (Online Fig. S2.16). Even though soil moisture conditions in this region returned to normal in the second half of the year, mean conditions for 2016 remained below average, thus increasing the risk of crop failure and food shortage in early 2017. (WMO 2017) For northeastern Brazil strong anomalous negative soil moisture conditions were observed for the fifth consecutive year (see previous *State of the Climate* reports, e.g., Dorigo et al. 2016) making it the longest drought recorded in this region. Anomalous dry conditions were also observed in western Bolivia and Peru, causing severe wildfires and shortages in water supply(see Chapter 7d2). At the subannual timescale, strong anomalous dry conditions were observed in Iran (January, February, December), Inner Mongolia (July, August), the southeastern United States (October, November), southern India (October–December), Turkey (November), and southeastern Europe (December) (Online Fig. S2.16).

Strong anomalous wet conditions were observed throughout the year for the southern part of South America, causing repeated heavy flooding in Argentina, Paraguay, and Uruguay. Wetter-than-usual conditions were also observed for eastern Europe and central Asia, alleviating the drought conditions that were reported for 2014 and 2015 in southern Russia (Dorigo et al. 2015a; Dorigo et al. 2016). Soil moisture conditions were also above average in central Europe, especially in February (Online Fig. S2.16). Anomalous wet soil moisture conditions throughout the year in Southeast Asia were associated with reported frequent severe flooding in this region. While the dry soil conditions observed in northern and eastern Australia (associated with El Niño) persisted into the first months of 2016 (Online Fig. S2.16), these were broadly compensated by above-average rainfall for the rest of the year, leading to wetter-than-usual soil moisture conditions for 2016 overall.

The year 2016 was marked by transition from strong El Niño conditions in the beginning of the year to weak La Niña/neutral ENSO conditions during the second half of the year. ENSO anomalies are known to potentially cause continental deviations in terrestrial water storages (Bauer-Marschallinger et al. 2013; Boening et al. 2012; Miralles et al. 2014a). ENSO-driven global negative soil moisture anomalies are clearly visible during the 1997/98 El Niño, while positive anomalies were observable for the strong La Niña episode of 2010/11, especially for the Southern Hemisphere (Fig. 2.27). Even though 2016 started with strong El Niño conditions, its negative impact on the global and, particularly, Southern Hemisphere soil moisture, was not as strong as for other recent El Niño events (e.g., 2004/05). This limited impact of El Niño on global soil moisture was already observed for 2015 and may be because other climate oscillations may have partly counterbalanced the negative effects

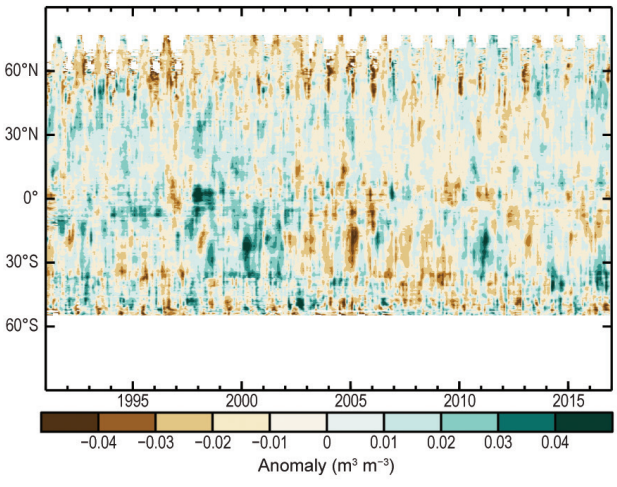

Fig. 2.27. Time–latitude diagram of surface soil moisture anomalies ($m^3 m^{-3}$; base period: 1991–2015). Data were masked as missing where retrievals are either not possible or of low quality (dense forests, frozen soil, snow, ice, etc.). (Source: ESA CCI Soil Moisture.)

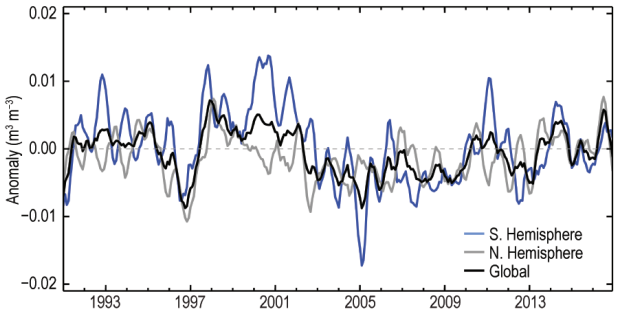

Fig. 2.28. Time series of 1991–2016 average global and hemispheric surface soil moisture anomalies ($m^3 m^{-3}$; base period: 1991–2015). Data were masked as missing where retrievals were either not possible or of very low quality (dense forests, frozen soil, snow, ice, etc.). (Source: ESA CCI Soil Moisture.)

of El Niño (Dorigo et al. 2016). Instead, globally and for both hemispheres, average soil moisture was slightly above normal in 2016 (Fig. 2.28).

No evident large-scale long-term global soil moisture trends can be observed (Fig. 2.28). This does not exclude, however, the existence of long-term trends at regional or local scales (Dorigo et al. 2012; Rahmani et al. 2016; S. Wang et al. 2016). Trends in average global soil moisture should be treated with caution owing to dataset properties changing over time and the inability to observe beneath dense vegetation or in mountain areas and frozen soils (cf. gray regions in Plate 2.1g and Online Fig. S2.16). Although the trends are based on surface soil moisture observations, they are generally also representative for the root zone because of the strong coupling between these layers.

9) Monitoring global drought using the self-calibrating Palmer drought severity index—T. J. Osborn, J. Barichivich, I. Harris, G. van der Schrier, and P. D. Jones

Hydrological drought results from a period of abnormally low precipitation, sometimes exacerbated by additional evapotranspiration (ET); its occurrence can be apparent in reduced river discharge, soil moisture, and/or groundwater storage, depending on season and duration of the event. Here, an estimate of drought called the self-calibrating Palmer drought severity index (scPDSI; Wells et al. 2004; van der Schrier et al. 2013a) is presented, using precipitation and Penman–Monteith potential ET from an early update of the CRU TS 3.25 dataset (Harris et al. 2014). Moisture categories are calibrated over the complete 1901–2016 period to ensure that "extreme" droughts and pluvials relate to events that do not occur more frequently than in approximately 2% of the months. This choice affects direct comparison with other hydrological cycle variables in Plates 2.1g–r which use a different baseline period. Other drought indices may give varied results (see van der Schrier et al. 2015).

Following the rapid expansion in the overall area of drought across the globe during 2015 (Osborn et al. 2016), drought area for 2016 was among the largest in the post-1950 record (Fig. 2.29). Every month of 2016 had at least 12% of global land experiencing severe drought conditions (scPDSI < −3), matched only by 1984 and 1985 (although 1983, 1986, and 1992 came close). Extreme drought conditions (scPDSI < −4) affected at least 4% of global land area in every month of 2016; a run of this length has not been matched by any other year in the post-1950 period, although extreme drought area peaked above 5% briefly in 1983 and above 6% briefly in 1984. The area where scPDSI indicates moderate drought (scPSDI < −2) peaked above 28% in early 2016 and declined to 26% by the end of the year. The current run (19 months as of December 2016) with at least 25% of global land area being affected by moderate drought is comparable with earlier periods such as 1965/66, 1970/71, 1991/92 and 2002/03, but it is currently dwarfed by the extended 69-month dry period of 1982–88. The 2016 peak should be interpreted cautiously, given that more observations for the final months of 2016 will become available in due course.

Although the area in drought during 2016 is no greater than at the end of 2015, the annual average extreme drought area in 2016 is around double the annual average for 2015 because 2015 began with a relatively small area in drought. This is evident in the more extensive regions of severe and extreme drought in 2016 (Plate 2.1q) compared with 2015 (Fig. 2.30). For example, drought intensified over southern and Mediterranean Africa, and it became more extensive across large parts of Brazil (except for the south) and

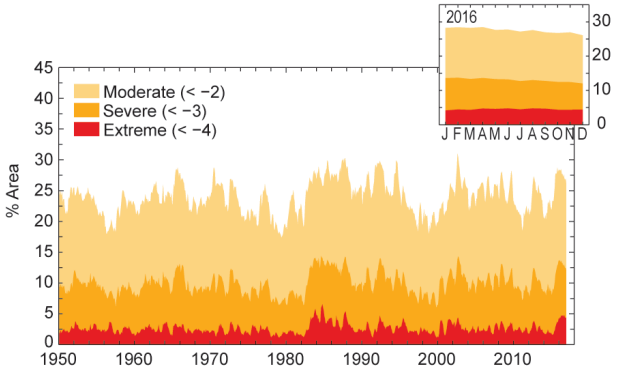

Fig. 2.29. Percentage of global land area (excluding ice sheets and deserts) with scPDSI indicating moderate (<–2), severe (<–3) and extreme (<–4) drought for each month of 1950–2016. Inset: 2016 monthly values.

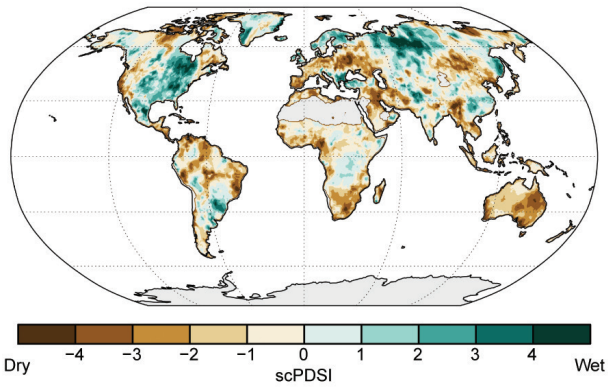

Fig. 2.30. Mean scPDSI for 2015. Droughts are indicated by negative values (brown), wet episodes by positive values (green). No calculation is made where a drought index is meaningless (gray areas: ice sheets or deserts with approximately zero mean precipitation).

other tropical countries in the northern half of South America (Jimenez-Muñoz et al. 2016). Moderate to severe drought is apparent in south-central Chile, a region undergoing a seven-year drought (Garreaud et al. 2017). Farther north, scPDSI values for 2016 were below –2 (indicating moderate to severe drought) in Columbia, Nicaragua, Honduras, and El Salvador, contributing to food insecurity in the region. The Californian drought was still present in 2016 (Plate 2.1q), although markedly less severe than in 2015 (Fig. 2.30).

The pattern of drought across sub-Saharan Africa is typical of that following an El Niño event, with dry conditions over southern Africa, particularly concentrated over Botswana, Zimbabwe, eastern regions of South Africa, and southern Mozambique, and wetter conditions farther north over Tanzania. Moderate to severe drought conditions are indicated by scPDSI < –2 around the Persian Gulf and through Iran to Pakistan (Plate 2.1q). Conditions in parts of India were drier during 2016 than in 2015, whereas much wetter conditions occurred across all of southern China. Farther north, negative (dry) values of scPDSI occurred over some regions of central Russia, but the remainder of extratropical Asia tended to be wetter than average. Dry conditions in Europe persisted or increased in the circum-Mediterranean, while much of Europe became wetter with the notable exception of eastern Europe. Droughts occurred in 2016 over the eastern half of Australia, parts of Indonesia, and Southeast Asia, as expected due to the strong El Niño event.

Similar to 2015, more than half of the land area south of 20°N was subject to some degree of drought in 2016. The area experiencing anomalously wet conditions, however, grew from 12% in 2015 to 17% in 2016, with a corresponding reduction in areas close to normal scPDSI and intense wet conditions in a region spanning southern Brazil, Uruguay, northeastern Argentina, and in areas around Lake Victoria.

Drought in 2016 was among the most extensive in the post-1950 record, including for the severe and extreme drought categories of the scPDSI. The strong El Niño of 2015/16 influenced the pattern of drought across the world's continents, although regional weather patterns modified or even overcame this influence in some parts of the world. The expansion in drought-affected areas during 2015 and 2016 is similar to the earlier expansion during the 1982/83 strong El Niño event (Fig. 2.31), consistent with a reduction in the atmospheric transport of moisture from oceans to land during El Niño events (Dai 2013), although the increased drought area persisted for about four years beyond the dissipation of that El Niño event (Fig. 2.29). A similar expansion did not occur, however, during the other major El Niño of the last 35 years (1997/98; Fig. 2.31), highlighting the complexity of the link between El Niño events and global drought area and the diversity of event types (G. Xu et al. 2016).

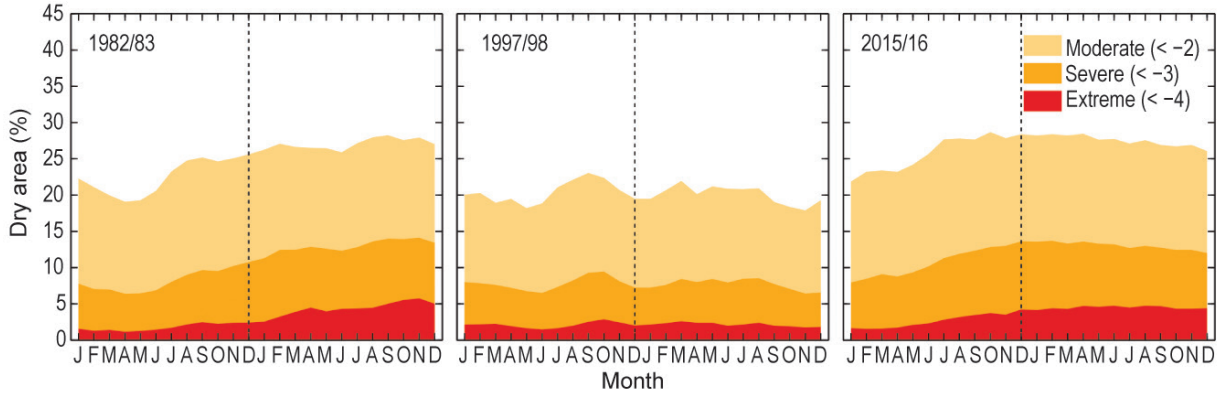

Fig. 2.31. Comparison of global drought-affected areas (%) for three strong El Niño events: 1982/83, 1997/98, and 2015/16.

10) Land evaporation—D. G. Miralles, B. Martens, H. E. Beck, A. J. Dolman, C. Jiménez, M. F. McCabe, and E. F. Wood

Terrestrial evaporation is an elusive variable: despite its pivotal role in linking water, energy, and biochemical cycles over land, global in situ measurements are scarce and satellites can only sense it indirectly. Nonetheless, pioneering efforts to infer evaporation from its satellite-observed environmental and climatic drivers (e.g., Price 1982; Nemani and Running 1989; Su 2002) have culminated in a range of datasets that can be used to monitor land evaporation dynamics at the global scale (e.g., Fisher et al. 2008; Miralles et al. 2011; Vinukollu et al. 2011; Yo. Zhang et al. 2016). While several international efforts remain focused on characterizing their uncertainties (McCabe et al. 2016; Miralles et al. 2016), these evaporation products are also being used to study a range of process behaviors, including: (1) trends in response to global warming (Jung et al. 2010; Yo. Zhang et al. 2016), (2) effects of internal climate variability on hydrology (Miralles et al. 2014b), (3) irrigation requirements in agricultural regions (Anderson et al. 2015), (4) evolution of drought conditions (Mu et al. 2013), and (5) role of land–atmospheric feedbacks during meteorological extremes (Miralles et al. 2014a).

Analyzing trends in continental evaporation facilitates the scrutiny of anticipated impacts of climate change on hydrology, such as the acceleration of the global water cycle or the *dry gets drier, wet gets wetter* hypothesis. Despite contrasting numbers found in the literature, the vast majority of studies report a mildly positive multidecadal trend during the satellite era (Miralles et al. 2014b; Yo. Zhang et al. 2016), although the reported trends are often not significant. Figure 2.32 shows the multidecadal terrestrial evaporation response based on GLEAM v3 (Miralles et al. 2011; Martens et al. 2017). An indicative linear trend of approximately 0.3 mm yr^{-1} (p = 0.002) for the entire globe can be determined from this figure, and it is due to the increase in evaporation in the Northern Hemisphere with this value being qualitatively in agreement with Clausius–Clapeyron expectations in a warming atmosphere (Miralles et al. 2014b; Brutsaert 2016; Trenberth et al. 2003). At monthly and annual timescales, the variability in mean continental evaporation is strongly affected by ocean–atmosphere oscillations, particularly due to the imprint of ENSO in Southern Hemisphere water-limited ecosystems (Miralles et al. 2014b).

In 2016, the global average terrestrial evaporation was higher than the 1980–2016 mean (Fig. 2.32), mainly due to a positive anomaly in the Northern Hemisphere during spring and summer (Fig. 2.33). This anomalous behavior is attributed to the high atmospheric temperatures during those two seasons (not shown). As the atmosphere returned to normal from the strong 2015 El Niño event, the negative anomalies in precipitation—and subsequently land evaporation—dissipated in the Southern Hemisphere (Fig. 2.32). Regionally, 2016 experienced anomalously low evaporation in eastern South America, northern Amazonia, southern Africa, the Horn of Africa, India, and Southeast Asia (Plate 2.1r)—in most of these regions, the reduced evaporation was associated with anomalously low precipitation and drought conditions (Section 2d9). Areas of positive anomalies include western Sahel, central and eastern Asia, eastern Australia, and central North America. In the latter region, the high summer temperatures contributed to a positive evaporation anomaly during the early

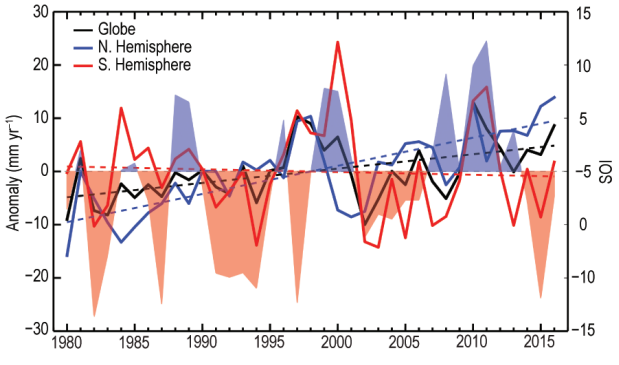

Fig. 2.32. Land evaporation anomaly (mm yr^{-1}; 1980–2016 base period) for the NH, SH, and the entire globe (solid lines). Linear trends are illustrated (dashed lines) and the values of the SOI (right axis, shaded area) are also shown. (Source: GLEAM.)

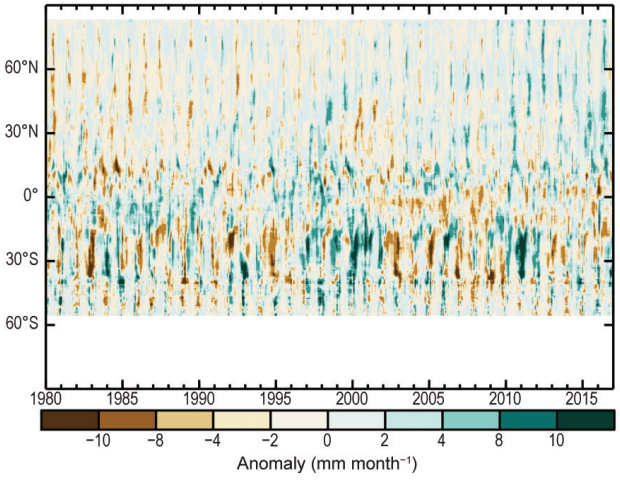

Fig. 2.33. Zonal mean terrestrial evaporation anomalies (mm month^{-1}; relative to 1980–2016). (Source: GLEAM.)

summer that exacerbated drying out the soils during early summer (NOAA 2017).

As a note of caution, anomalies and trends in satellite-based evaporation should be interpreted with considerable care, due to accuracy issues in the satellite and meteorological forcing, parameterization uncertainties, and choice of retrieval algorithms (Ershadi et al. 2014; Martens et al. 2017). Thus, the weighted use of multiple retrieval approaches is usually advised (Miralles et al. 2016; McCabe et al. 2016). While the operational monitoring of continental evaporation is becoming a realistic proposition (Ghilain et al. 2011; Anderson et al. 2011), current algorithms dedicated to estimating evaporation from satellite observations at global scales are mostly intended for research applications and are not currently updated in near-real time.

e. *Atmospheric circulation*

1) Mean sea level pressure and related modes of variability—R. Allan and C. K. Folland

Mean sea level pressure (MSLP) data reveal the major modes of variability that drive significant weather and climate events (Kaplan 2011). Arguably, the most globally impactful mode is the El Niño–Southern Oscillation (ENSO), for which the sea level pressure–derived Southern Oscillation index (SOI; Allan et al. 1996; Kaplan 2011) is an indicator. For 2015 through mid-2016, the SOI was negative, indicating the presence of an El Niño that was the strongest since that of 1997/98 (see Chapter 4b).

The SOI since 2009 showed a shift from El Niño to strong La Niña conditions around mid-2010, which persisted until its demise in early 2012, followed by near-normal conditions until early 2013. A swing to negative (El Niño-type) conditions occurred in early 2014 (Fig. 2.34b). The SOI was negative from February 2014 until April 2016 (except April–May 2014 and February 2015; see Fig. 2.34b). Hence, the Niño-3 and -4 regions of sea surface temperature (SST) anomalies

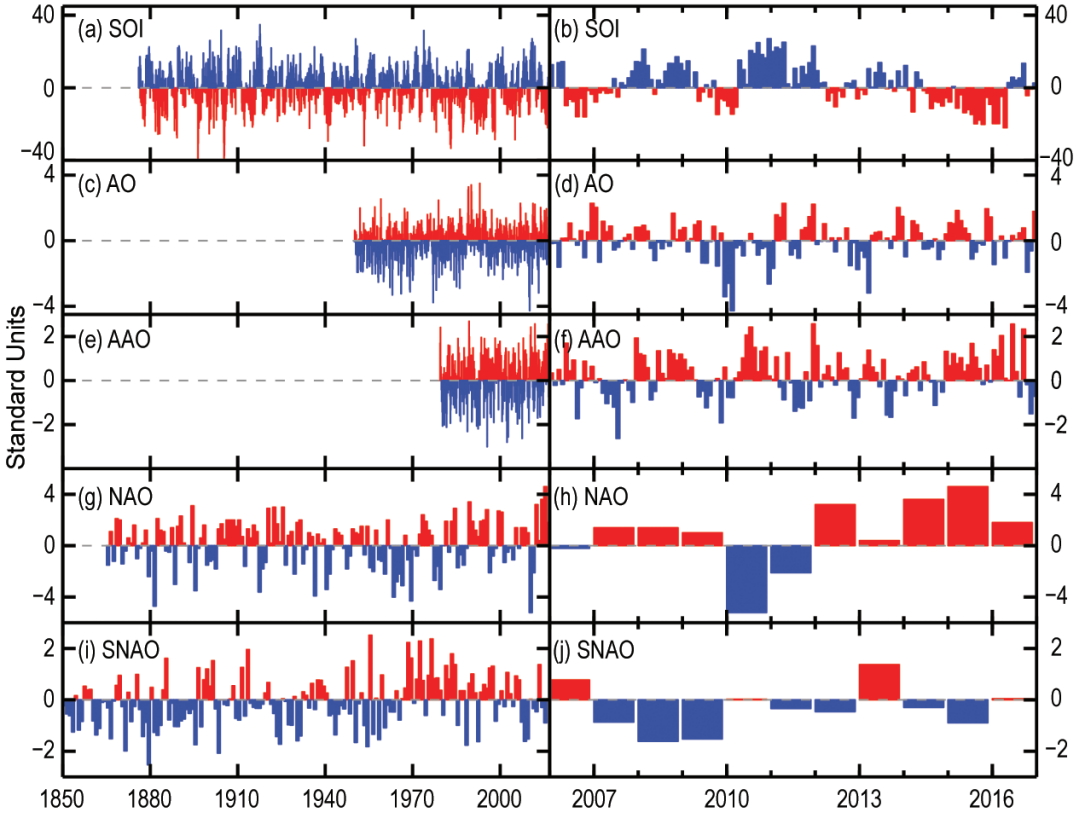

Fig. 2.34. Time series for modes of variability described using sea level pressure for the (left) complete period of record and (right) 2006–16. (a),(b) SOI (provided by the Australian Bureau of Meteorology); (c),(d) AO (NCEP Climate Prediction Center); (e),(f) AAO (NCEP Climate Prediction Center); (g),(h) winter (Dec–Feb) NAO average (NCAR; presented for winter at the beginning of each year so winter 2016/17 is not shown); (i),(j) summer (Jul–Aug) SNAO average (Folland et al. 2009).

were positive from April and February 2014 until June and August 2016, respectively (see Chapter 4b). Following the definition in Allan and D'Arrigo (1999), this constitutes a protracted El Niño episode. Figures 2.34a,b show the presence of these protracted El Niño and La Niña episodes in the SOI record since 1876, demonstrating that they can last up to six years (e.g., the 1990–95 protracted El Niño; see Gergis and Fowler 2009).

Owing to ocean–atmosphere interactions across the Indo–Pacific region, major El Niño and La Niña events can be near-global in their influence on world weather patterns via teleconnections to higher latitudes. Protracted El Niño and La Niña episodes tend to be more regional in their impacts (Allan and D'Arrigo 1999; Allan et al. 2003). As an example from Australia: in Queensland, the main impact appears to be periods of persistent drought (widespread flooding), which often occur during protracted El Niño (La Niña) episodes (Murphy and Ribbe 2004). The dry 2014 through mid-2016 period across much of Queensland reflects this latest protracted El Niño episode. Since May 2016, the SOI has been around neutral conditions.

More regionally, the Arctic Oscillation (AO), North Atlantic Oscillation (NAO), and the Antarctic Oscillation (AAO) indices can also be derived from MSLP (Figs. 2.34c–h). In the Northern Hemisphere, the last six winters have displayed broadly positive NAO conditions but a diverse range of circulation patterns. During the 2014/15 boreal winter the NAO was mainly positive, the North Pacific anticyclone was weak, and the Aleutian low was prominent (Figs. 2.34g,h, 2.35a). By contrast, during the early winter of 2015/16 the NAO oscillated between phases, with a deep trough over the North Atlantic leading to an enhanced jet stream that directed a series of extratropical cyclones towards northern Ireland and Scotland–northern England (Figs. 2.34g,h, 2.35b,e). By the mid-to-latter part of the 2015/16 winter the pattern had changed, with the NAO swinging from slightly negative in January to positive in February. The Aleutian low was enhanced, favoring downstream troughs over the North Atlantic–northern Europe sector and a northerly displacement of midlatitude storm tracks. Overall, it was the second wettest winter on record for the United Kingdom with 159% of normal rainfall, behind 2013/14 which saw 167%, and the wettest on record for Ireland. The 2016/17 boreal winter was marked by an increasingly positive NAO through mid-December 2016, temporarily negative NAO values around the start of 2017, and then a fluctuation between phases for the rest of January (Figs. 2.34g,h,

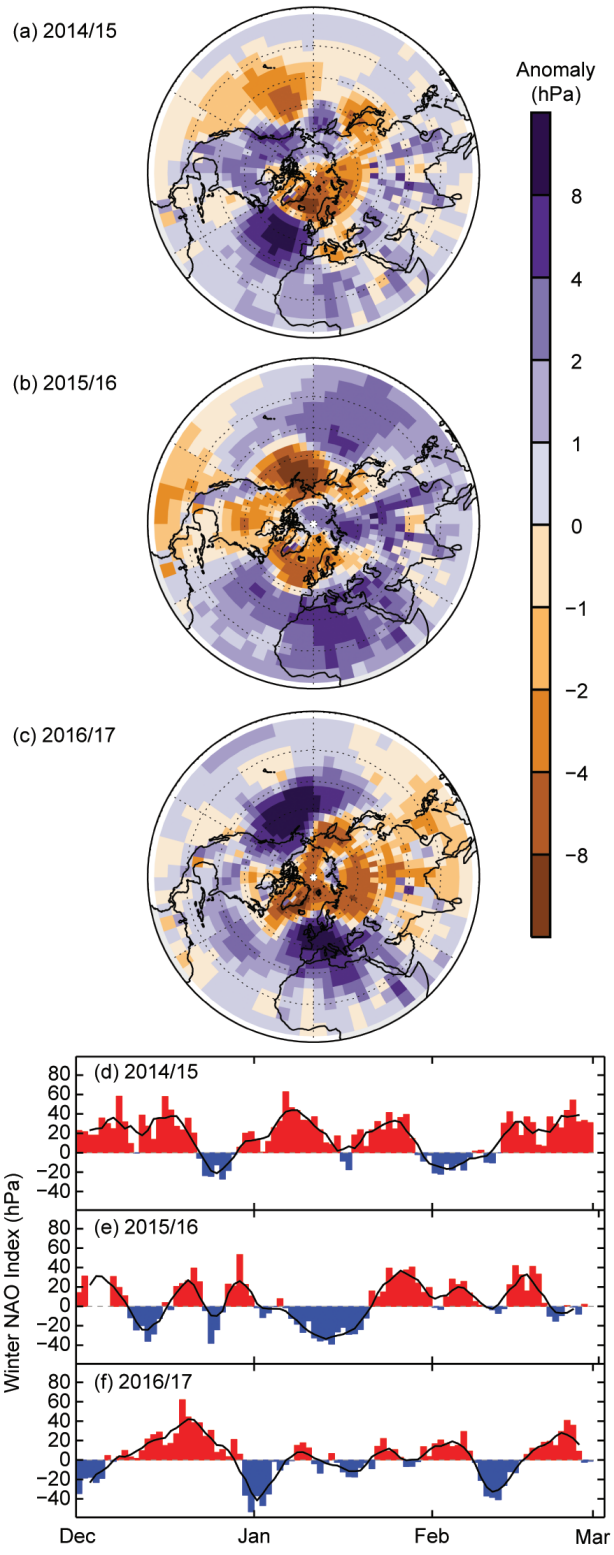

Fig. 2.35. (a) Boreal winter sea level pressure anomalies (hPa; 1981–2010 base period) averaged over Dec–Feb for (a) 2014/15, (b) 2015/16, and (c) 2016/17. (d) NAO daily time series (hPa) for winter (d) 2014/15, (e) 2015/16, and (f) 2016/17. The 5-day running mean is shown by the solid black line. The data are from HadSLP2r (Allan and Ansell 2006).

2.35c,f). The Aleutian low was markedly weakened, and winter storminess over the United Kingdom to western European region was reduced. Values of various UK precipitation series for October 2016 through January 2017 were drier than their counterparts a year earlier.

In 2016, the phase of the summer NAO (SNAO), defined over July and August as in Folland et al. (2009), was on average near neutral (Fig. 2.36a,b). There was a persistent region of anticyclonic anomalies over Greenland, normally associated with a negative SNAO, offset by further anticyclonic anomalies in the Atlantic west of western Europe extending toward Scandinavia with weak negative anomalies in between. Overall, July 2016 showed a weak negative SNAO and August a positive SNAO. Intraseasonal variability was quite large (Fig. 2.36c) compared to the July–August mean SNAO which shows a generally negative level but no trend in recent years. There is a continuing tendency toward a more negative July–August SNAO on decadal timescales since 1970 (Figs. 2.34i,j). The current decadally averaged SNAO is at a similar level to its long-term average over 1850–1960. The decline in recent decades, however, has been from exceptionally positive levels in the 1970s.

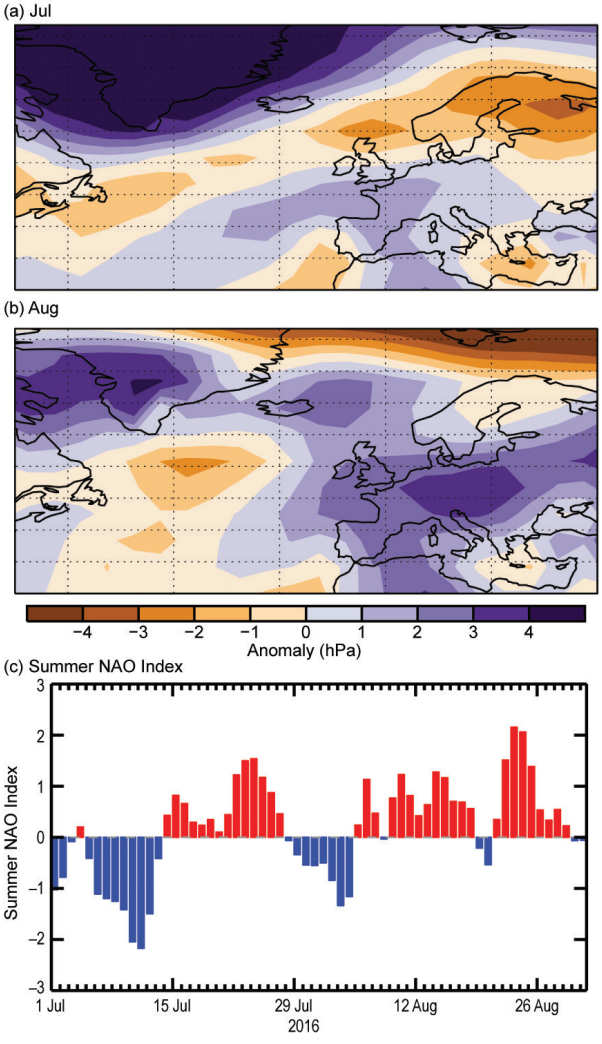

Fig. 2.36. MSLP (hPa) in (a) Jul and (b) Aug 2016 using HadSLP2r; (c) daily SNAO in Jul and Aug 2016.

In the Southern Hemisphere, the AAO was in its positive phase during 2015/16 (Figs. 2.34e,f), which favors reduced sea ice extent in the West Antarctic Peninsula (WAP) region, owing to enhanced westerly wind conditions (Stammerjohn et al. 2008). During 2015, however, the WAP sea ice margins were extended (http://nsidc.org/data/seaice_index) but had retreated to near-normal extent in 2016. In the interplay between the protracted El Niño, which favors a weaker polar jet stream, and a positive AAO mode, with stronger westerly winds, the former appeared to have dominated. Related positive wind speed anomalies were noted at 850 hPa (Section 2e3) over the midlatitude Southern Ocean. However, with the cessation of the protracted El Niño episode in mid-2016 and the AAO becoming negative (Fig. 2.34f), there has been a major reduction in the WAP sea ice margin since November 2016 (http://nsidc.org/data/seaice_index).

2) Surface winds—C. Azorin-Molina, R. J. H. Dunn, C. A. Mears, P. Berrisford, and T. R. McVicar

Surface wind speed slightly declined over land in 2016 (relative to 2015 and the climatology; Plate 2.1u; Fig. 2.37a), with an observed global (excluding Australia) average anomaly from the 1981–2010 climatology of −0.006 m s^{-1} (Table 2.4). After a continuous slowdown of wind speed (termed "stilling"; Roderick et al. 2007) from the beginning of records in 1973, this negative but nearly zero anomaly confirms indications of a "recovery" of wind speed since 2013 (Kim and Paik 2015; Dunn et al. 2016a). Although negative anomalies were reported for the North America (−0.083 m s^{-1}), Europe (−0.073 m s^{-1}), and Australia (−0.008 m s^{-1}) in 2016, all of them are less negative than the lowest values reached (in around 2013). This recent strengthening in terrestrial wind speed is more evident in central (+0.108 m s^{-1}) and East (+0.084 m s^{-1}) Asia, both showing positive anomalies in 2016. The occurrence of moderate (>3 m s^{-1}) and strong (>10 m s^{-1}) winds (Figs. 2.37b,c) exhibited a different long-term behavior: moderate winds displayed no trend at all or a weakly increasing trend in agreement with the recent recovery mentioned above. Strong winds showed the opposite pattern, reaching the second lowest percentage of occurrence (2.04%) globally in 2016.

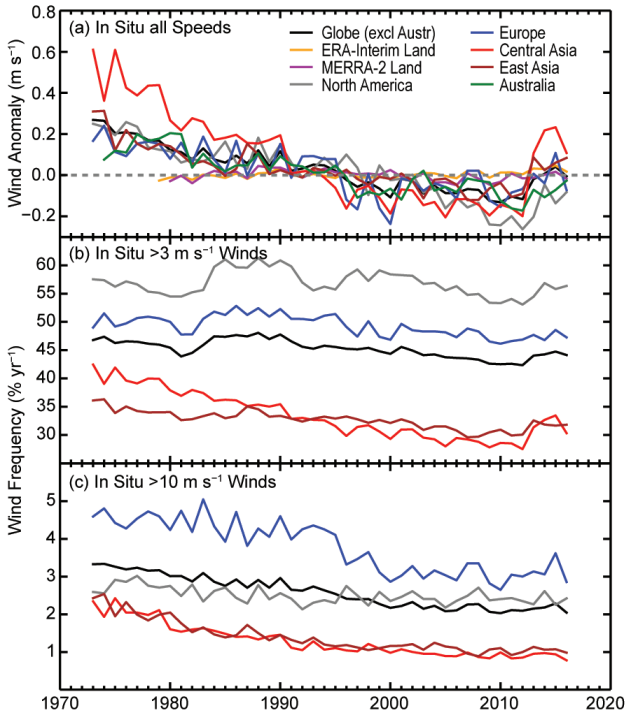

Fig. 2.37. (a) Land surface wind speed anomalies (m s^{-1}) for 1973–2016, relative to 1981–2010: HadISD2 for the globe (excluding Australia) and 4 regions; Australia (1974–2016) is based on an Australian dataset. ERA-interim (1979–2016) and MERRA-2 (1980–2016) anomalies, also shown, cover all land areas. Occurrence frequencies (in %) for wind speeds (b) >3 m s^{-1} and (c) >10 m s^{-1} do not include Australia.

The assessment of the spatial and temporal variability of surface wind speed in 2016 is based on two quality-controlled datasets from anemometer observation records: (1) the global HadISD2 (1973–2016; Dunn et al. 2012, 2016b) and (2) an Australian database (1974–2016; McVicar et al. 2008). As the spatial representativeness of these site-specific wind speed observations is limited (2625 stations in total), with low-density in, for example, South America and Africa, 10-m wind speed fields from the MERRA-2 (1980–2016; Gelaro et al. 2017) and the ERA-Interim reanalysis (1979–2016; Dee et al. 2011) are used to cover contiguous global scales (including ocean surfaces). Reanalysis products have the ability to provide global wind speed data, although investigations have detected shortcomings in the simulation of near-surface layer processes (e.g., McVicar et al. 2008; Pryor et al. 2009; Vautard et al. 2010).

Over land, during 1979–2016, observed long-term trends of wind speed were slightly negative for all regions, with a global declining change of −0.070 m s^{-1} decade^{-1}, being more negative in Australia (−0.068 m s^{-1} decade^{-1}) and less negative in East Asia (−0.043 m s^{-1} decade^{-1}) (Table 2.4). In comparison to 1979–2015 trends reported in Dunn et al. (2016a), inclusion of 2016 means linear trends are less negative due to the recent "recovery". This means that the sign and in particular the magnitude of trends are strongly sensitive to the period considered (Azorin-Molina et al. 2014). Despite the slight slowdown of terrestrial 1979–2016 wind speed, Fig. 2.38 displays a clear dominance of stations showing negative trends from the observed HadISD2 and the Australian dataset (65.6%) over those reporting positive trends (34.4%), especially for Northern Hemisphere midlatitudes. This agrees with the worldwide slowdown of terrestrial wind speed reviewed by McVicar et al. (2012). The wind speed anomalies and trends over land from ERA-Interim and MERRA-2 underestimate the magnitude of changes seen in the station-based datasets, as discussed in previous studies (McVicar et al. 2008; Pryor et al. 2009; Vautard et al. 2010).

Table 2.4. Global and regional statistics for land-surface wind speed using observational HadISD2 and Australian (McVicar et al. 2008) datasets for 1979–2016. Trend column includes 5%–95% confidence range.

Region	Mean 1981–2010 (m s^{-1})	Anomaly 2016 (m s^{-1})	Trend 1979–2016 (m s^{-1} decade^{-1})	Number of Stations
Globe (excluding Australia)	3.327	−0.006	−0.070 (−0.077 ♠ −0.062)	2584
North America	3.715	−0.083	−0.093 (−0.105 ♠ −0.081)	588
Europe	3.663	−0.073	−0.057 (−0.069 ♠ −0.045)	777
Central Asia	2.875	+0.108	−0.132 (−0.148 ♠ −0.105)	258
East Asia	2.739	+0.084	−0.043 (−0.052 ♠ −0.035)	460
Australia	2.066	−0.008	−0.068	41

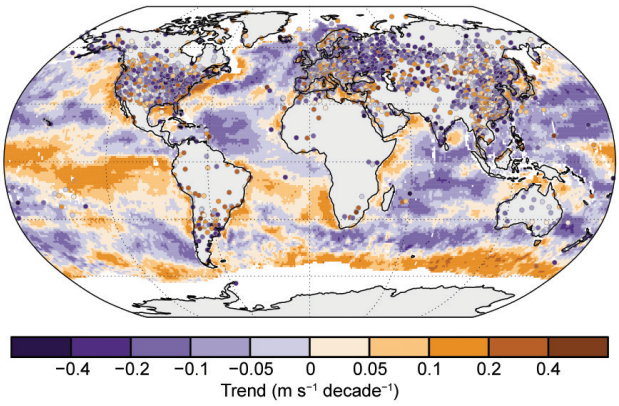

Fig. 2.38. Wind speed trends (m s^{-1} decade^{-1}) for the observational HadISD2 and Australian datasets (points) over land for 1979–2016, and the observational RSS radiometer over ocean for 1988–2016.

The attribution of long-term terrestrial wind speed trends, including the recent "recovery", is uncertain as different possible causes are occurring simultaneously and the mechanisms behind them likely vary spatio–temporally. The declining trend over the last 35 years has been attributed to, for example, changes in large-scale atmospheric circulation (Azorin-Molina et al. 2014, 2016); an increase of surface roughness (Vautard et al. 2010; Bichet et al. 2012; Wever 2012; Wu et al. 2016); instrumentation changes (Wan et al. 2010) and different measurement time intervals (Azorin-Molina et al. 2017); and air pollution (Xu et al. 2006). In contrast, the recent wind speed recovery has, to date, been poorly analyzed. Kim and Paik (2015) attributed this recovery to an increase of the spatial variance in near-surface air temperature.

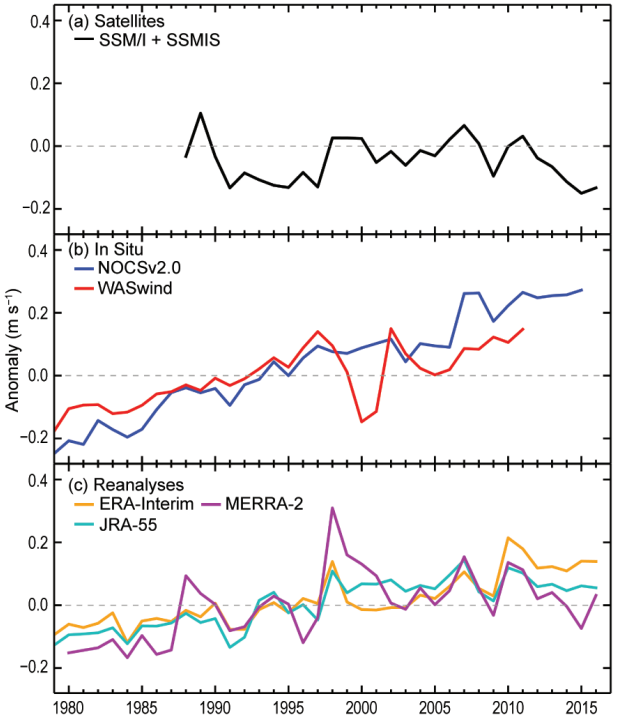

Fig. 2.39. Global average surface wind anomaly (m s^{-1}) over ocean relative to the 1981–2010 base period from (a) satellite radiometers, (b) in situ, and (c) reanalyses.

Over oceans, estimates of globally averaged wind speed obtained from satellite-borne microwave radiometers continued to be lower than average in 2016 (Wentz 1997; Wentz et al. 2007). Reanalysis winds over oceans, which are in relatively good agreement with both the satellite data and with each other from 1990 to 2009, diverge after 2010 (Fig. 2.39). All products show an increasing trend from 1990 to 2007, followed by a decline in 2008/09, and a recovery in 2010/11. Since then the wind speeds have fallen substantially in the satellite and MERRA-2 products but remained roughly constant for ERA-Interim and JRA-55. During 2016, winds showed large negative anomalies across the tropical Pacific and Indian Oceans (Plate 2.1u). Other ocean regions with negative anomalies include much of the southern Pacific and regions in the North Atlantic. The North Pacific showed large positive anomalies, with smaller positive anomalies present in the western North Atlantic and the southern Indian and Atlantic Oceans.

3) Upper air winds—L. Haimberger and M. Mayer

Upper air winds and their related potential and stream functions are essential climate variables that can indicate changes in planetary scale circulation patterns. During 2016, one of the strongest El Niños in recent decades decayed. As discussed in last year's report, the impact of the 2015/16 El Niño on upper-level divergent winds was weaker than that of the 1997/98 event. During the second half of 2016, weak La Niña conditions developed in the tropical Pacific. Anomalies of velocity potential and divergent winds at 200 hPa from ERA-Interim in November 2016 (Fig. 2.40b) are compared to those of November 1998 (Fig. 2.40a), when La Niña conditions prevailed. In both years, there is a distinct quadrupole pattern of anomalous upper-level divergence over the Indo-Pacific warm pool and the tropical Atlantic and anomalous upper-level convergence over the central to eastern Pacific as well as the Indian Ocean. This pattern is consistent with Mayer et al. (2013, 2014), who found a similar quadrupole anomaly pattern in the divergence of atmospheric energy transports and ocean heat content changes associated with La Niña.

Over the Pacific, anomalies of upper-level divergent winds seem to be weaker in 2016 compared to 1998, consistent with comparatively weak negative SST anomalies in the eastern equatorial Pacific. In contrast, the anomalous convergence over the Indian

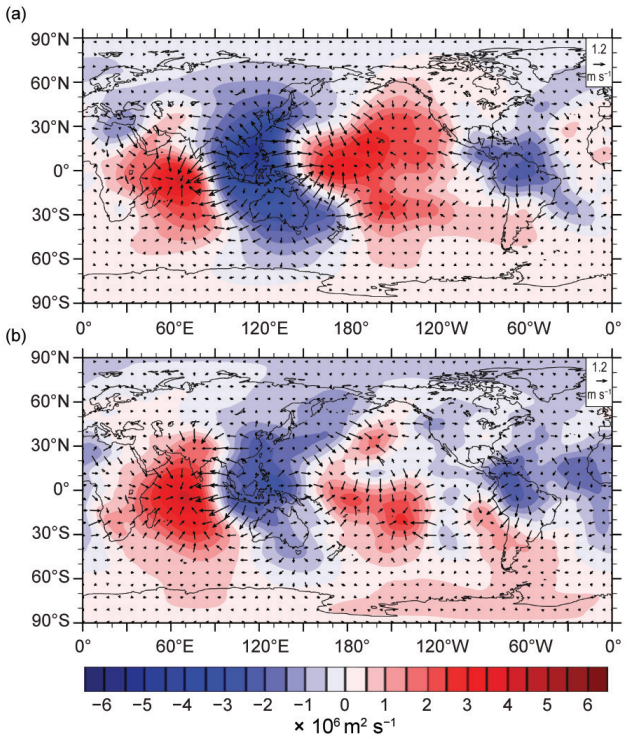

Fig. 2.40. Three-month averages of velocity potential (× 10^6 m^2 s^{-1}) and divergent wind at 200 hPa compared to the 1979–2014 average. Anomalies centered around (a) Nov 1998 and (b) Nov 2016.

Ocean was strong, in agreement with severe drought conditions in eastern Africa. Consistent with the shift in the divergence patterns, the number of central Pacific hurricanes (2) and Indian Ocean cyclones (1) was much lower than in 2015, while storm counts were high in the eastern Pacific (13) and western Pacific (13; where the storm season started late due to El Niño conditions in boreal spring but became very active in boreal autumn), as well as in the Atlantic (7).

The quasi-biennial oscillation (QBO), perhaps the most prominent stratospheric global oscillation phenomenon, is interesting because it reveals the limitations of our ability to reconstruct the stratospheric circulation with data from the mid-20th century observing system. This year it also deserves special attention because tropical stratospheric winds exhibited a strongly anomalous behavior in the first half of 2016. Figure 2.41 shows series of tropical and northern subtropical upper-air winds from observations and reanalyses since the mid-20th century. Radiosonde and pilot balloon are the best sources for station-based upper air wind climatologies, with data back to the early 1940s in the northern extratropics. Reanalyses need upper air information to capture the QBO, as can be seen from the increasingly better depiction with the ERA-preSAT (Hersbach et al. 2017) experimental assimilation run. Surface data–only reanalyses, which extend further back, currently do not capture the QBO. As suggested by the QBO reconstruction of Brönnimann et al. (2007) in Fig. 2.41c there is, however, enough information back to 1908 to reconstruct the state of the QBO. In the most recent years the agreement between reanalyses in terms of zonal mean winds is excellent.

As noted by Newman et al. (2016) and Dunkerton (2016) the strong 2015/16 El Niño may have also impacted the QBO, which exhibited a highly unusual and strong upward propagation of equatorial wind regimes, particularly between 10 hPa and 40 hPa.

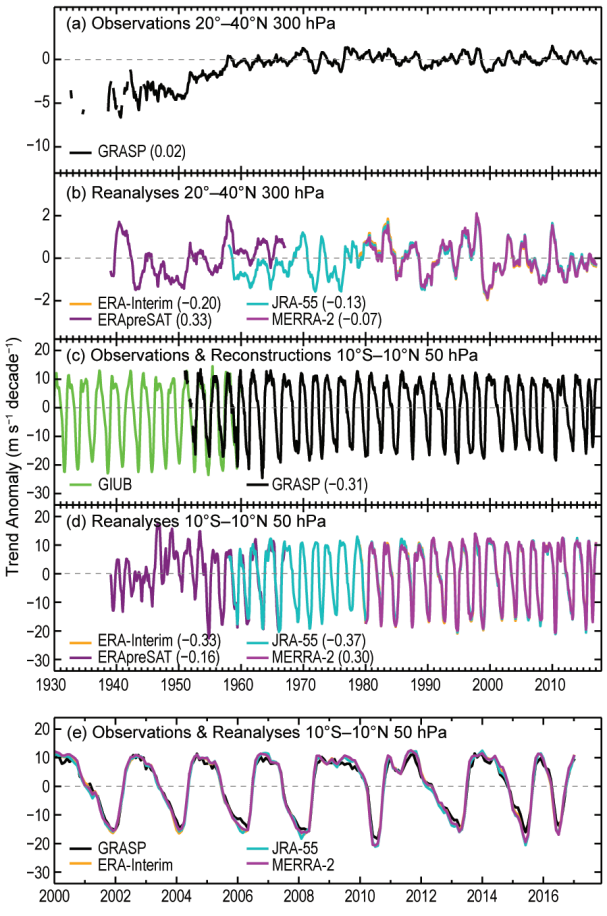

Fig. 2.41. Time series of zonal mean U-wind component in the 20°–40°N belt at 300 hPa from (a) radisondes and tracked balloons and (b) reanalyses; smoothed using a 12-point boxcar filter. Time series in the tropical belt 10°N–10°S at 50 hPa, calculated from (c) pilot balloon/radiosonde winds (GRASP; Ramella-Pralungo et al. 2014) and statistical reconstructions from (GIUB; Brönnimann et al. 2007). (d) ERA-Interim, MERRA-2, JRA-55 and ERA-preSAT reanalyses. (e) Same as (d) but for 2000–17 period only. Values in the legend are linear trends between 1981 and 2010 (m s^{-1} $decade^{-1}$). Trends for ERApreSAT and GIUB are for 1940–60. Note that positive (negative) changes in the zonal wind speed imply an increase in westerlies (easterlies).

This upward propagation, which cannot be explained by the QBO standard model, is unique since observations began in 1953 and was observed during the whole boreal spring of 2016. It is visible also in Figs. 2.41d,e as the very last westward wind maximum occurring only one year after the "regular" westward wind maximum in 2015. Osprey et al. (2016) attribute the QBO disruption more to influences from Northern Hemisphere midlatitudes. It will be interesting to follow the QBO after this disruption.

f. Earth radiation budget

1) Earth radiation budget at top-of-atmosphere—D. P. Kratz, P. W. Stackhouse Jr., T. Wong, P. Sawaengphokhai, A. C. Wilber, S. K. Gupta, and N. G. Loeb

Earth's radiation budget (ERB) at the top-of-atmosphere (TOA) represents the balance of the incoming total solar irradiance (TSI), the reflected shortwave (RSW), and the outgoing longwave radiation (OLR). This balance defines the energetic state of the Earth–atmosphere system, which drives weather processes, climate forcing, and climate feedbacks.

The years 2015 and 2016 were remarkable for the rise and fall of the most intense El Niño event to occur since the exceptionally strong 1997/98 El Niño event (see Chapter 4b). Having fully developed by May 2015, the 2015/16 El Niño remained strong through early 2016, as enumerated by the multivariate ENSO index (MEI; Wolter and Timlin 1993, 1998; www.esrl.noaa.gov/psd/enso/mei). After April 2016, however, the MEI index began a rapid decline, falling to roughly neutral levels by August, thereafter remaining relatively neutral through December. This latest El Niño event provided a stark contrast to the overall neutral conditions observed in 2013, the last relatively ENSO neutral year. The global-annual mean OLR in 2016 was ~0.70 W m^{-2} higher and the global-annual mean RSW was ~0.90 W m^{-2} lower when compared to 2013 (Table 2.5). The combination of the individual components amounted to an increase of ~0.15 W m^{-2} in the total net radiation into Earth's climate system relative to 2013, indicating net heating for 2016. The magnitude of the global-annual mean changes appears to be increasing relative to the ENSO neutral year of 2013, perhaps indicative of the atmospheric response due to the circulation anomalies over the past few years. Relative to the long-term average (2001–15), the global-annual mean flux anomalies (Table 2.5) for 2016 are, respectively, +0.65, −0.05, −0.70, and 0.00 W m^{-2} for OLR, TSI, RSW, and total net flux. The OLR and RSW anomalies were outside the corresponding 2-sigma interannual variability for this period and, thus, are significant. The positive 2016 OLR anomaly is most likely due to the strong El Niño. The negative 2016 global-annual mean RSW flux anomaly exceeds typical interannual variability, implying a darkening of Earth's TOA albedo. Interestingly enough, however, the large OLR and RSW anomalies in 2016 nearly canceled each other to produce an essentially zero global mean total net flux.

The monthly mean anomaly in the TOA flux time series (Fig. 2.42) for 2016 reveals that the OLR anomaly fluctuated between a maximum of +1.7 W m^{-2} and a minimum of 0 W m^{-2}. Indeed, the amplitude of the anomalies for the first five to six months was often greater than 0.8 W m^{-2}. The rapid decrease in the strength of the El Niño thereafter corresponded well with the MEI values. Overall, this led to a large positive annual OLR anomaly (see Table 2.5) with generally higher values near the equinoxes. This observed OLR variability is generally consistent with the NOAA-HIRS OLR (Lee et al. 2011). Meanwhile, the absorbed shortwave (TSI minus RSW) anomaly began the year at +0.5 W m^{-2}, followed by a general oscillating increase to a value around +0.8 W m^{-2} at year's end. The overall positive values for 2016 led to a large absorbed shortwave anomaly for the year. The total net anomaly, representing the combined OLR and absorbed shortwave anomalies, began 2016 with a value

Table 2.5. Global annual mean TOA radiative flux changes between 2016 and 2013 (the last non-El Nino year), and between 2016 and 2015 for the outgoing longwave radiation (OLR), total solar irradiance (TSI), reflected shortwave (RSW) and total net fluxes. The global annual mean radiative flux anomalies relative to their corresponding 2001–15 mean climatological values, and the 2-sigma interannual variabilities of the 2001–15 global annual mean fluxes are also shown. All units are in W m^{-2} and all flux values have been rounded to the nearest 0.05 W m^{-2} (round off errors account for components not adding to Net).

	Global Annual Mean Difference		2016 Anomaly (W m^{-2})	Interannual variability (W m^{-2})
	2016 minus 2013 (W m^{-2})	2016 minus 2015 (W m^{-2})		
OLR	+0.70	+0.40	+0.65	±0.60
TSI	−0.05	−0.10	−0.05	±0.15
RSW	−0.90	−0.15	−0.70	±0.55
Net	+0.15	−0.35	+0.00	±0.65

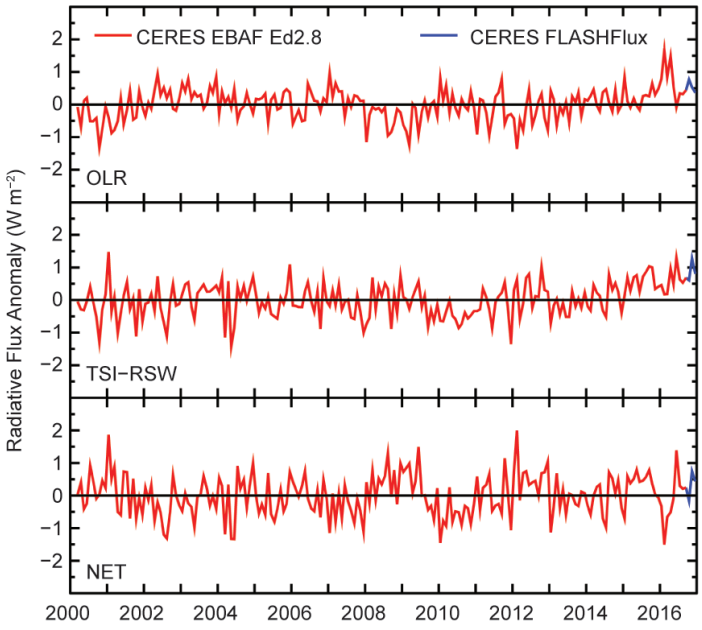

Fig. 2.42. Time series of global monthly mean deseasonalized anomalies (W m^{-2}) of TOA Earth radiation budget for OLR (upper), absorbed shortwave (TSI−RSW; middle), and total net (TSI−RSW−OLR; lower) from Mar 2000 to Dec 2016. Anomalies are relative to their calendar month climatology (2001–15). The time series shows the CERES EBAF Ed2.8 1Deg data (Mar 2000–Sep 2016) in red and the CERES FLASHFlux version 3B data (Oct–Dec 2016) in blue; see text for merging procedure (Sources: https://ceres.larc.nasa.gov/compare_products.php and https://eosweb.larc.nasa.gov/project/ceres/ceres_table.)

of −0.3 W m^{-2}, fell to −1.5 W m^{-2}, then recovered to positive values peaking in June at +1.4 W m^{-2} before remaining mostly positive, oscillating between −0.15 and +0.74 W m^{-2} for the remainder of the year. The periods of negative net anomalies occurred during the El Niño, and the positive net anomalies occurred after the El Niño had decayed. These offsetting positive and negative values tended to cancel, thereby producing essentially no annual total anomaly in the net flux.

The TSI data used in this study are provided by the Total Irradiance Monitor aboard the Solar Radiation and Climate Experiment (SORCE) spacecraft (Kopp and Lean 2011) and by the Royal Meteorological Institute of Belgium composite dataset (Dewitte et al. 2004), both renormalized to the SORCE Version 15. The RSW and OLR data were obtained from the Clouds and the Earth's Radiant Energy System (CERES) mission (Wielicki et al. 1996; 1998) aboard Terra and *Aqua*.

The time series (Fig. 2.42) was constructed from the CERES EBAF (Energy Balanced And Filled) Ed2.8 product (Loeb et al. 2009; 2012) for March 2000 to September 2016 and from the CERES Fast Longwave and Shortwave Radiative Fluxes (FLASHFlux) products (Kratz et al. 2014) for October to December 2016. The normalization of the FLASHFlux data (Stackhouse et al. 2016) results in a 2-sigma monthly uncertainty of ±0.23, ±0.08, ±0.19 and ±0.26 W m^{-2} for the OLR, TSI, RSW, and total net radiation, respectively. Note that FLASHFlux data are not intended for analyses longer than six months.

2) Mauna Loa Observatory clear-sky "apparent" solar transmission—K. Lantz and J. Augustine

Radiation from the sun is the fundamental energy that drives Earth's weather and climate. At the top of the atmosphere (TOA), the difference between the incoming and outgoing solar radiation represents the net radiation (energy) that is available within the Earth–atmosphere system. Incoming radiation is scattered and absorbed by the intervening atmosphere of clouds, aerosols, and gases before being transmitted to the surface. Across Earth the absorbed solar radiation is unevenly distributed both spatially and temporally; these differences are intricately reflected in our weather and climate. Atmospheric solar transmission has been measured at the Mauna Loa Observatory (MLO) in Hawaii by NOAA's Global Monitoring Division (GMD) since 1958 and is one of the longest, continuous records of that quantity. Because of its remote Pacific location and high elevation (3.4 km), the solar transmission at MLO represents the free tropospheric transmission with limited contamination from local influences. This record is often used to show the influence of large explosive volcanic eruptions, but it can also detect small volcanic eruptions into the upper troposphere and lower-most stratosphere (UT/LMS). Small volcanic eruptions have been shown to contribute aerosols up to 15 km in mid- to high latitudes (Ridley et al. 2014).

Daily and monthly clear-sky "apparent" solar transmission (AT) is calculated using ratios of direct-beam broadband solar irradiance pyrheliometer measurements for various pairs of fixed atmospheric paths (airmass = 2, 3, 4, 5; Ellis and Pueschel 1971). This technique is advantageous because ratios of direct solar irradiance remove influences due to instrument calibration and the variability of extraterrestrial irradiance. This analysis is also limited to clear-sky periods to remove cloud effects and to highlight the influence of aerosols or other trace gases in the atmospheric column. Past studies of changes in clear-sky AT at MLO have investigated the influences of volca-

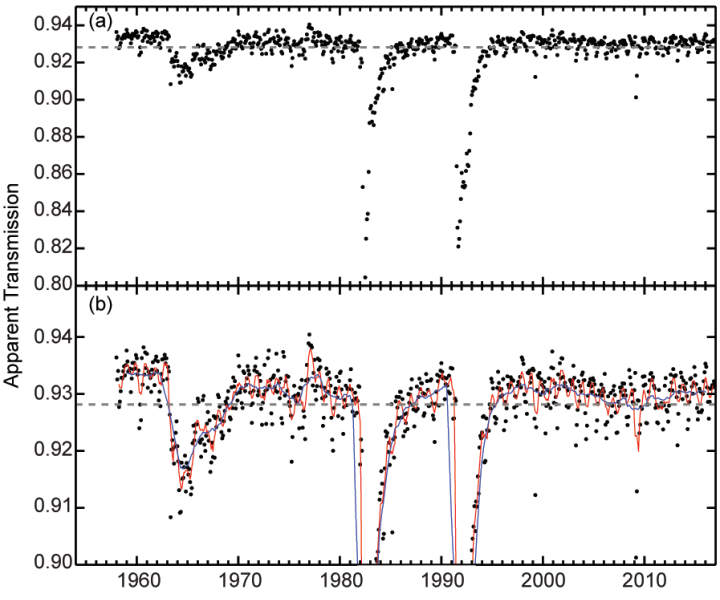

Fig. 2.43. (a) Monthly mean of the clear-sky AT at MLO. Means are determined from the morning values to reduce local influences. Gray dashed line is the 1958–62 background level. (b) Enlarged plot to highlight the seasonal (red line) and longer term changes (blue line) in the clear-sky AT record. The red line is the 6-month running smoothed fit, and the blue line is the 24-month smoothed fit.

nic aerosol, aerosol transport from Asia, ozone, water vapor, and the quasi-biennial oscillation (Bodhaine et al. 1981; Dutton 1992; Dutton and Bodhaine 2001; Dutton et al. 1985). However, effects due to aerosols are the most prominent.

The monthly record of clear-sky AT has been updated through December 2016 (Figs. 2.43a,b). Monthly averages are calculated using morning values during prevailing downslope wind to avoid local boundary layer influences that occur in the afternoon when the wind shifts to upslope conditions. Major volcanic eruptions from Agung, El Chichón, and Mt. Pinatubo are clearly visible in 1964, 1982, and 1991 (Fig. 2.43a). The gray dashed line reflects the cleanest background observed from1958 to 1962 and a brief period in 1978. Seasonal trends are highlighted by a 6-month running smoothed fit to the monthly values (Fig. 2.43b, red line) and have been attributed primarily to Asian aerosol transport in the spring (Bodhaine et al. 1981). Longer-term changes are highlighted by a 24-month running smoothed fit (Fig. 2.43b, blue line). Following the eruption of Mt. Pinatubo in 1991, the monthly clear-sky AT eventually returned to near-background conditions in mid-1998. The 24-month fit shows a slow decrease in clear-sky AT in the following decade (Fig. 2.43b). This slow decrease in clear-sky AT has been attributed to increased background aerosol due to several small volcanic eruptions (Solomon et al. 2011; Vernier et al. 2011). For example, several smaller dips in the 24-month smoothed fit coincide with the eruptions of Sarychev (Russia) and Redoubt (Alaska) in the spring of 2009 and Nabro (Eritrea) in June 2011 (Global Volcanism Program, www.volcano.si.edu; Andersson et al. 2015). This trend in AT does not continue after 2011 and is consistent with evidence from the NASA *CALIPSO* satellite record of 30°–60°N that shows a period of quiescence in the effects of these smaller volcanic eruptions on the UT/LMS (Andersson et al. 2015). Interestingly, this pattern of increasing aerosol optical depth (AOD) in the mid-1990s, then a slowing around 2011 can be seen in the long-term NOAA SURFRAD AOD record across rural regions of the contiguous United States, when limiting annual means to the five cleanest days of the year to limit influences from regional pollution (J. Augustine 2016, personal communication). There is a negligible change in the mean of the monthly clear-sky AT in 2016 with an increase of 0.00138 with respect to 2015, and the amplitude of the seasonal changes in clear-sky AT in 2016 is 0.006 consistent with the observed amplitude in 2015.

g. Atmospheric composition

1) Long-lived greenhouse gases—E. J. Dlugokencky, B. D. Hall, S. A. Montzka, G. Dutton, J. Mühle, and J. W. Elkins

The three most dominant long-lived greenhouse gases (LLGHG) contributing to climate forcing are, in decreasing order: carbon dioxide (CO_2), methane (CH_4), and nitrous oxide (N_2O). In 1958 systematic measurements of CO_2 began at Mauna Loa, Hawaii (MLO), and the atmospheric CO_2 abundance was ~315 ppm (parts per million in dry air). In 2016, MLO annual average CO_2 reached 404.2 ± 0.1 ppm (www.esrl.noaa.gov/gmd/ccgg/trends) while global average CO_2 at Earth's surface was 402.9 ± 0.1 ppm (Fig. 2.44a).

Fourfold increases in anthropogenic emissions of CO_2 from both fossil fuel combustion and cement production are largely responsible for its atmospheric growth since 1958 (Boden et al. 2015). About half of this anthropogenic CO_2 remains in the atmosphere while the other half is taken up by the terrestrial biosphere and oceans where it acidifies seawater (see Chapter 3j). The global growth rate of atmospheric CO_2 has risen from 0.6 ± 0.1 ppm yr^{-1} in the early

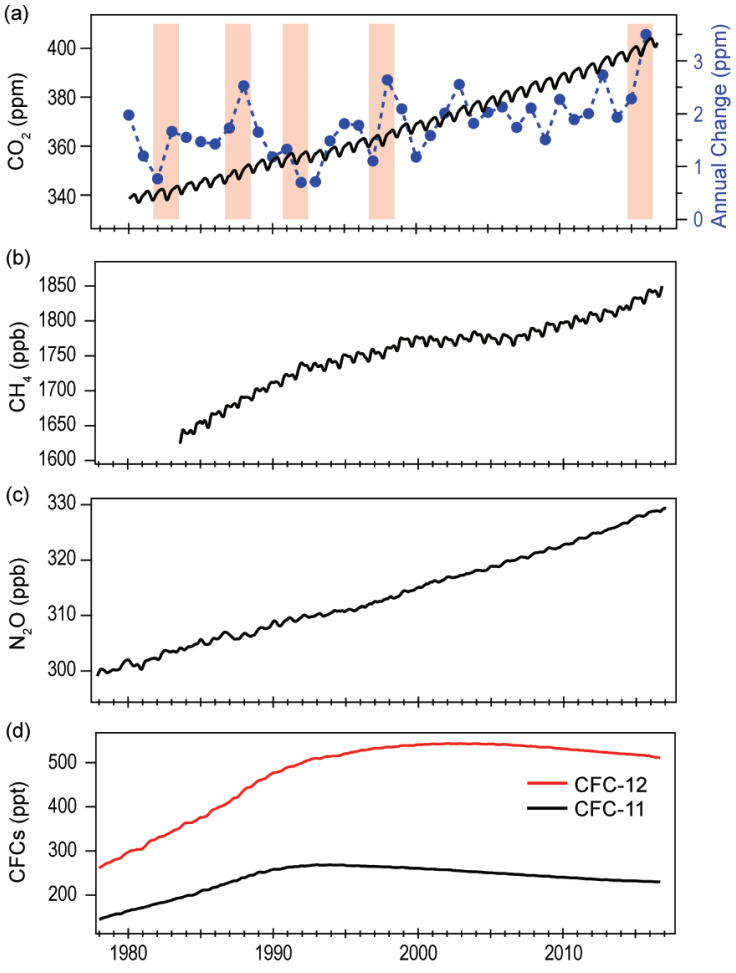

Fig. 2.44. Global mean surface mole fractions (in dry air) of (a) CO_2 (black curve, ppm), (b) CH_4 (ppb), (c) N_2O (ppb), and (d) CFC-12 and CFC-11 (ppt) derived from the NOAA sampling network. (a) Also shown in (a) are changes in annual global means of CO_2 (blue markers), and periods of moderate or stronger El Niño periods (shaded bands) based on Oceanic Niño Index values >1.5. (Source: www.cpc.noaa.gov/products/analysis_monitoring/ensostuff/ensoyears.shtml.)

1960s to an average of 2.3 ± 0.6 ppm yr^{-1} during the past ten years. However, the increase in global annual mean CO_2 from 2015 to 2016 was 3.5 ± 0.1 ppm (0.88% ± 0.03%), the largest annual increase observed in the 58-year atmospheric measurement record. The previous largest increase (2.7 ppm) occurred between 2012 and 2013. ENSO can play a role in the interannual variability of the CO_2 growth rate through its influence on terrestrial carbon fluxes (Bastos et al. 2013). The strong El Niño that peaked in late 2015 (indicated by shaded area in Fig. 2.44a) undoubtedly contributed to the record CO_2 increase from 2015 to 2016 (Betts et al. 2016).

Methane is emitted from both anthropogenic (~60%) and natural (~40%) sources (Fung et al. 1991). Anthropogenic sources include agriculture (e.g., ruminants and rice), fossil fuel extraction and use, biomass burning, landfills, and waste. Natural sources include wetlands, geological sources, oceans, and termites (Dlugokencky et al. 2011). A recent study has shown that fossil fuel exploitation (coal, oil, and natural gas) contributes more emissions than previously believed, ~30% of total global CH_4 emissions, but the magnitude of these emissions is likely not increasing (Schwietzke et al. 2016). The atmospheric CH_4 burden has increased 250% since pre-industrial time and currently contributes ~0.5 W m^{-2} direct radiative forcing, with an additional ~0.3 W m^{-2} indirect radiative forcing from the CH_4-related production of tropospheric ozone and stratospheric H_2O (Myhre et al. 2013). Based on observations of globally averaged CH_4, its rate of increase, and an estimate of its lifetime (~9.1 yr), total global CH_4 emissions are estimated at ~540 Tg CH_4 yr^{-1} (1 Tg = 10^{12} g) with a relatively small uncertainty of ~±10%. Bottom-up estimates of CH_4 emissions by country and source are challenging because the complex atmospheric CH_4 budget is composed of many sources that are difficult to quantify.

The rate of CH_4 increase slowed from more than 10 ppb yr^{-1} in the 1980s to nearly zero in the early 2000s, then increased to an average of ~7 ppb yr^{-1} since 2007 (Fig. 2.44b). Surface observations, including the spatial distribution and rate of increase, provide strong top-down constraints on CH_4 source and sink budgets. The 2016 globally averaged CH_4 mole fraction at Earth's surface was 1843.0 ± 0.8 ppb based on NOAA background air sampling sites. The increase in annual means from 2015 to 2016 of 9.0 ± 0.9 ppb was slightly less than for 2014 to 2015.

Nitrous oxide is both a greenhouse gas and an ozone-depleting substance (Ravishankara et al. 2009). The observed ~60 ppb (22%) increase in atmospheric N_2O over preindustrial levels (270 ppb) is largely the result of nitrogen-based fertilizer use (Park et al. 2012). The mean global atmospheric N_2O mole fraction in 2016 was 328.9 ± 0.1 ppb, an increase of 0.8 ppb from the 2015 mean (Fig. 2.44c). The 0.8 ppb annual change is similar to the average increase in global annual means over the last decade.

Halogenated gases, such as chlorofluorocarbons (CFCs), hydrochlorofluorocarbons (HCFCs), hydrofluorocarbons (HFCs), and carbon tetrachloride (CCl_4)

Table 2.6. Summary table of long-lived greenhouse gases for 2016 (CO_2 mixing ratios are in ppm, N_2O and CH_4 in ppb, and all others in ppt).

Industrial Designation or Common Name	Chemical Formula	AGGI	ODGI	Radiative Efficiency (W m^{-2} ppb^{-1})[a]	Mean Surface Mole Fraction, 2016 (change from prior year)[b]	Lifetime (years)
Carbon Dioxide	CO_2	Y	N	1.37×10^{-5}	402.9 (3.5)[c]	
Methane	CH_4	Y	N	3.63×10^{-4}	1843.0 (9.0)[c]	9.1
Nitrous Oxide	N_2O	Y	N	3.00×10^{-3}	328.9 (0.8)[c,d]	123
Chlorofluorocarbons						
CFC-11	CCl_3F	Y	Y	0.26	230.1 (–1.4)[c,d]	52
CFC-12	CCl_2F_2	Y	Y	0.32	512.5 (–3.6)[c,d]	102
CFC-113	CCl_2FCClF_2	Y	Y	0.30	71.6 (–0.3)[c]	93
Hydrochlorofluorocarbons						
HCFC-22	$CHClF_2$	Y	Y	0.21	237.2 (4.2)[c]	11.9
HCFC-141b	CH_3CCl_2F	Y	Y	0.16	24.5 (0.3)[c]	9.4
HCFC-142b	CH_3CClF_2	Y	Y	0.19	22.0 (0.2)[c]	18
Hydrofluorocarbons						
HFC-134a	CH_2FCF_3	Y	N	0.16	89.1 (5.6)[c]	14
HFC-152a	CH_3CHF_2	Y	N	0.10	6.6 (0)[c]	1.6
HFC-143a	CH_3CF_3	Y	N	0.16	17.5 (1.4)[c]	51
HFC-125	CHF_2CF_3	Y	N	0.23	18.9 (1.9)[c]	31
HFC-32	CH_2F_2	N	N	0.11	11.5 (1.6)[c]	5.4
HFC-23	CHF_3	Y	N	0.18	28.9 (0.8)[c]	228
HFC-365mfc	$CH_3CF_2CH_2CF_3$	N	N	0.22	0.89 (0.02)[c]	8.7
HFC-227ea	CF_3CHFCF_3	N	N	0.26	1.20 (0.02)[c]	36
Chlorocarbons						
Methyl Chloroform	CH_3CCl_3	Y	Y	0.07	2.6 (–0.5)[c]	5.0
Carbon Tetrachloride	CCl_4	Y	Y	0.17	81.3 (–0.9)[c,d]	33
Methyl Chloride	CH_3Cl	N	Y	0.01	563 (13)[c]	0.9
Bromocarbons						
Methyl Bromide	CH_3Br	N	Y	0.004	6.9 (0.3)[c]	0.8
Halon 1211	$CBrClF_2$	Y	Y	0.29	3.5 (–0.1)[c]	16
Halon 1301	$CBrF_3$	Y	Y	0.30	3.3 (0)[c]	72
Halon 2402	$CBrF_2CBrF_2$	Y	Y	0.31	0.4 (0)[c]	28
Fully fluorinated species						
Sulfur Hexafluoride	SF_6	Y	N	0.57	8.88 (0.29)[c]	>600
PFC-14	CF_4	N	N	0.09	82.7 (0.8)[c]	~50000
PFC-116	C_2F_6	N	N	0.25	4.56 (0.07)[c]	~10000

[a] Radiative efficiencies were taken from IPCC AR5 (Myhre et al. 2013). Steady-state lifetimes were taken from Myhre et al. (2013) (CH_4), Ravishankara et al. (1993) (SF_6), Ko et al. (2013), SPARC (2016) (CCl_4), and Carpenter et al. (2014). For CO_2, numerous removal processes complicate the derivation of a global lifetime.

[b] Mole fractions are global, annual surface means for the indicated calendar year determined from the NOAA global cooperative air sampling network (Hofmann et al. 2006), except for PFC-14, PFC-116, and HFC-23 which were measured by AGAGE (Mühle et al. 2010; Miller et al. 2010). Changes indicated in parentheses are the differences between the 2016 and 2015 global surface mean mole fractions.

[c] Preliminary estimate.

[d] Global mean estimates derived from multiple NOAA measurement programs ("Combined Dataset").

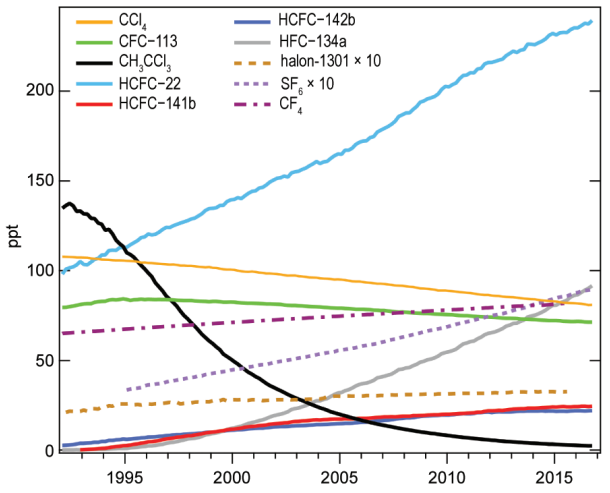

Fig. 2.45. Global mean mole fractions at Earth's surface (ppt, dry air) for several halogenated long-lived greenhouse gases. See Table 2.6 for the 2016 global mean mole fractions of these gases.

also contribute to radiative forcing. Atmospheric mole fractions of some CFCs, such as CFC-12 and CFC-11, have been decreasing for a decade or more in response to production and consumption restrictions imposed by the Montreal Protocol and its Amendments (Fig. 2.44d). The atmospheric burdens of many CFC-replacement compounds (HCFCs and HFCs) continued to increase in 2016 (Fig. 2.45; Table 2.6).

The NOAA Annual Greenhouse Gas Index (AGGI) summarizes trends in the combined direct radiative forcing by five major LLGHGs (CO_2, CH_4, N_2O, CFC-11, and CFC-12) and 15 minor gases (Hofmann et al. 2006; Fig. 2.46; www.esrl.noaa.gov/gmd/aggi). The AGGI represents the annual cumulative radiative forcing of these gases relative to the Kyoto Protocol baseline year of 1990 (2.17 W m^{-2}). It does not include indirect radiative forcings (e.g., influences on ozone and water vapor). In 2016, CO_2 contributed 1.99 W m^{-2} direct radiative forcing, 66% of the combined forcing of 3.03 W m^{-2} by the 5 major LLGHGs and 15 minor gases (Table 2.6). The combined forcing in 2016 represents a nearly 40% increase since 1990 (2016 AGGI = 1.399 ± 0.002) and a 1.82% increase over the 2015 AGGI of 1.374 ± 0.002. The current combined forcing is equivalent to a global average CO_2 mole fraction of ~490 ppm. Even without further increases in radiative forcing, current levels of long-lived greenhouse gases portend significant further warming, sea level rise, and financial cost to future generations (Hansen et al. 2016).

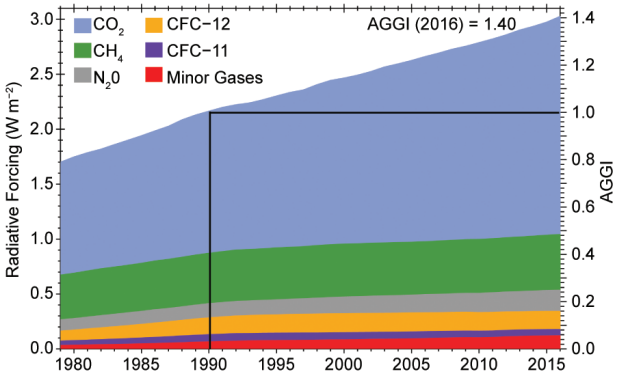

Fig. 2.46. Direct radiative forcing (W m^{-2}) due to 5 major LLGHG and 15 minor gases (left axis) and the associated values of the AGGI (right axis). Direct radiative forcing due to LLGHG and 15 minor gases, 3.03 W m^{-2} in 2016, has increased 40% since 1990 (AGGI = 1.4 for 2016).

2) Ozone depleting gases—B. D. Hall, S. A. Montzka, G. Dutton, and J. W. Elkins

In 2016 the combined radiative forcing by CFCs, HCFCs, and other halogenated ozone-depleting gases was 0.32 W m^{-2}, 10% of the total radiative forcing by LLGHG (Table 2.6; Fig. 2.46). In addition, these chlorine- and bromine-containing gases contribute indirectly to radiative forcing by destroying stratospheric ozone. The emissions and atmospheric burdens of many of the most potent ozone-depleting gases have been declining (Figs. 2.44d, 2.45) in response to production and consumption restrictions imposed by the Montreal Protocol on Substances that Deplete the Ozone Layer and its Amendments and Adjustments. The combined direct radiative forcing of CFC-11 and CFC-12 has declined 7% since 2000, from 0.238 ± 0.001 W m^{-2} in 2000 to 0.222 ± 0.001 W m^{-2} in 2016, contributing to the "climate benefit" of the Montreal Protocol (Velders et al. 2007).

Equivalent effective stratospheric chlorine (EESC) is a measure of the ozone-depleting potential of the stratospheric halogen loading at a given time and place. As EESC declines, stratospheric ozone is showing some signs of recovery (Bourassa et al. 2014; Pawson et al. 2014; see Section 2g4). EESC is calculated from global average surface mole fractions of halogenated, ozone-depleting gases and weighting factors that include surface- to-stratosphere transport times, mixing during transit, photolytic reactivity, and ozone-destruction efficiency (Schauffler et al. 2003; Newman et al. 2007). Progress toward reducing the stratospheric halogen load is evaluated by the NOAA Ozone-Depleting Gas Index (ODGI; Hofmann and Montzka 2009; www.esrl.noaa.gov/gmd/odgi). The ODGI relates EESC in a given year to the maximum EESC value (ODGI = 100) and the 1980 EESC value (ODGI = 0), a benchmark often used to assess prog-

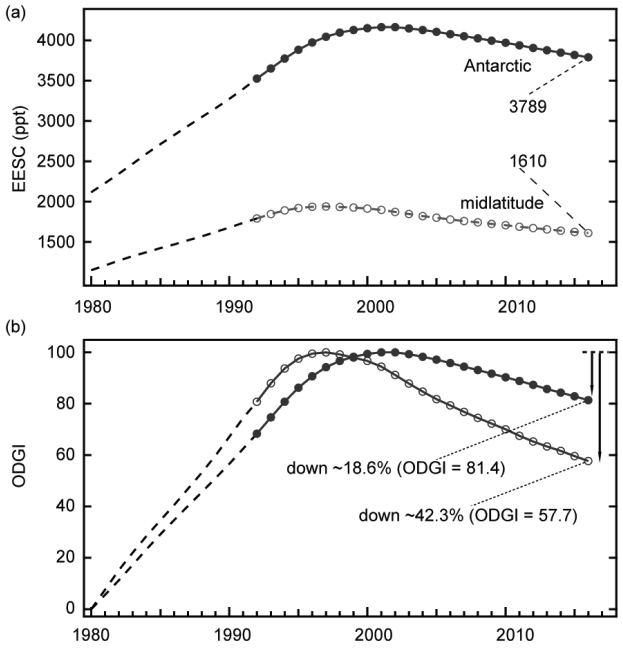

Fig. 2.47. (a) EESC (ppt) and (b) NOAA ODGI. The ODGI represents the relative mole fractions of reactive halogen in in the midlatitude (open circles) and Antarctic (closed circles) stratospheres scaled such that ODGI = 100 at maximum EESC and zero in 1980. ODGI values in these two regions have dropped 42.3% and 18.6%, respectively, from their peak values. Both EESC and ODGI are derived from NOAA surface measurements of ozone-depleting gases (circles) or, for earlier years, WMO scenarios (dashed lines; Harris et al. 2014). The EESC and ODGI values from 1992 forward are for Jan of each year.

ress towards reducing stratospheric halogen loadings to pre-ozone hole levels (Fig. 2.47).

The EESC and ODGI are calculated for two representative stratospheric regions—Antarctica and the midlatitudes—that differ in total available reactive halogen (Fig. 2.47a). EESC is larger in the Antarctic stratosphere than in the midlatitudes because more ozone-reactive halogen is released during the longer transit time to the Antarctic. At the beginning of 2016, ODGI values in the Antarctic and midlatitude stratospheres were 81.4 and 57.7, respectively, compared to 82.9 and 59.5 at the same time in 2015. The 2016 values represent 18.6% and 42.3% reductions from the peak values in EESC over Antarctica and the midlatitudes, respectively, toward the 1980 benchmarks.

3) Aerosols—S. Rémy, A. Benedetti, and O. Boucher

Atmospheric aerosol particles affect Earth's climate and can present a serious public health issue during surface pollution events (WHO 2013). Aerosols impact climate directly by scattering and absorbing short- and long-wave radiation, and indirectly by affecting the concentrations, sizes, and chemical composition of cloud condensation nuclei that influence clouds' life cycles, optical properties, and precipitation activity. More information about the radiative forcing by aerosols is provided by Boucher et al. (2013).

Data in this section are based on the Copernicus Atmosphere Monitoring Service (CAMS) interim reanalysis of global aerosols (Flemming et al. 2017) that is constrained by Collection 5 MODIS retrievals of aerosol optical depth (AOD) at 550 nm (Remer et al. 2005). CAMS couples all relevant physical aerosol processes, such as emissions, wet/dry deposition, and sedimentation, with meteorology. Five aerosol types are considered: sea salt, desert dust, black carbon, organic matter, and sulfate aerosols. Biomass burning aerosol emissions equal the sum of black carbon and organic matter emitted by open fires and biofuel combustion. Open fire emission estimates were provided by the Global Fire Assimilation System (GFAS) inventory (Kaiser et al. 2012) based on MODIS observations of fire radiative power. CAMS interim reanalysis of total AOD has a –2.5% bias relative to independent, ground-based AERONET (Aerosol Robotic Network) observations, but the AERONET stations may not be representative of global field values at the model resolution.

The 2016 average anomalies of AOD at 550 nm due to total aerosols, dust, and biomass burning (Plates 2.1x,y,z, respectively) depict strong regional influences. These were calculated against 2003–16 mean values. Dust anomalies were positive in most of the source regions (southern Sahara, Arabian Peninsula, and the Taklamakan desert in northwestern China) and several areas downwind of the sources. The strong positive anomalies extending from western Africa to South America indicate more active trans-Atlantic dust transport than in previous years. More dust than usual was also transported to the Mediterranean region from central and eastern Sahara, and from the Taklamakan to Mongolia and northern China. Negative dust anomalies were found over Iran and the Caspian Sea.

Overall, the 2016 anomalies of biomass burning aerosols (Plate 2.1z) are consistent with those of tropospheric ozone (Section 2g6), carbon monoxide (Section 2g7), and fires (Section 2h3). Seasonal biomass burning in 2016 was more severe than usual in many regions. Biomass burning and total AOD anomaly maps show the large fire events of 2016 in and around equatorial Africa, in Siberia northwest of Lake Baikal (May–August), and in western Canada

(May–August), including the Fort McMurray fire (May) in northeastern Alberta (see Sidebar 7.1). Biomass burning aerosols in the Amazon basin in 2016 were below the long-term average, continuing the downward trend from 2003. Interestingly, there was much lower fire activity than usual in Indonesia in 2016, following a year (2015) of extreme Indonesian fire activity caused by a powerful El Niño event (Benedetti et al. 2016).

Positive sea salt aerosol anomalies (not shown) over the North Atlantic Ocean were caused by a more active storm season there in January–February and again in December 2016. Sea salt anomalies were also positive over the northeast Pacific region.

Time series of globally averaged total AOD during 2003–16 (Fig. 2.48) show strong seasonality, with semiannual maxima typically in March–April and August–September driven mainly by dust episodes and biomass burning in Africa and South America.

Figure 2.49 presents global maps of the 2003–16 average total AOD, linear trends in total AOD from 2003 through 2016, and the number of days with extremely high AOD values. The highly polluted areas of eastern Asia and India are prominent features in the total AOD map (Fig. 2.49a), as are the dust-producing regions of the Sahara, Arabia, the Middle East, and the Taklamakan and Gobi deserts. Seasonal biomass burning drives the large total AOD values over equatorial Africa and Indonesia. The map of linear trends in total AOD (Fig. 2.49b) highlights long-term decreases in anthropogenic aerosols over the eastern United States, Europe, Japan, and parts of southern China, while increases in anthropogenic aerosols occurred over most of the Indian subcontinent. Decreasing trends in the southern Amazon basin are associated with reduced deforestation (Chen et al. 2013) while those over the northern Sahara and western Mediterranean indicate fewer and/or weaker dust episodes in these regions. Although there are many Southern Hemisphere oceanic regions with positive trends, these may be an artifact of the MODIS Collection 5 observations used in the reanalysis which, over these areas, are typically greater than MODIS Collection 6 (Levy et al. 2013) observations. The number of days with extremely high AOD values (Fig. 2.49c) shows that most extreme events are associated with large fires in Siberia, Central and South

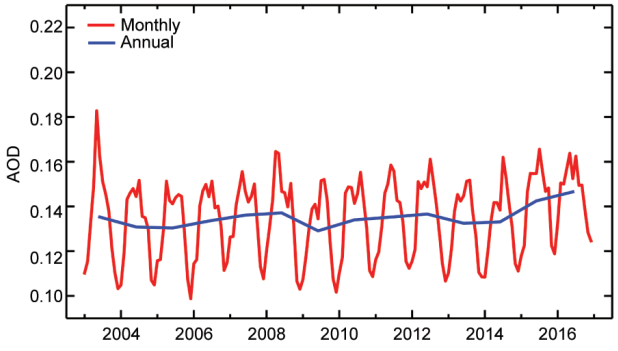

Fig. 2.48. Global averages of total AOD at 550 nm averaged over monthly (red) and annual (blue) periods for 2003–16. A linear regression fit to the monthly averages suggests a long-term increase, but the trend is not statistically significant (95% confidence).

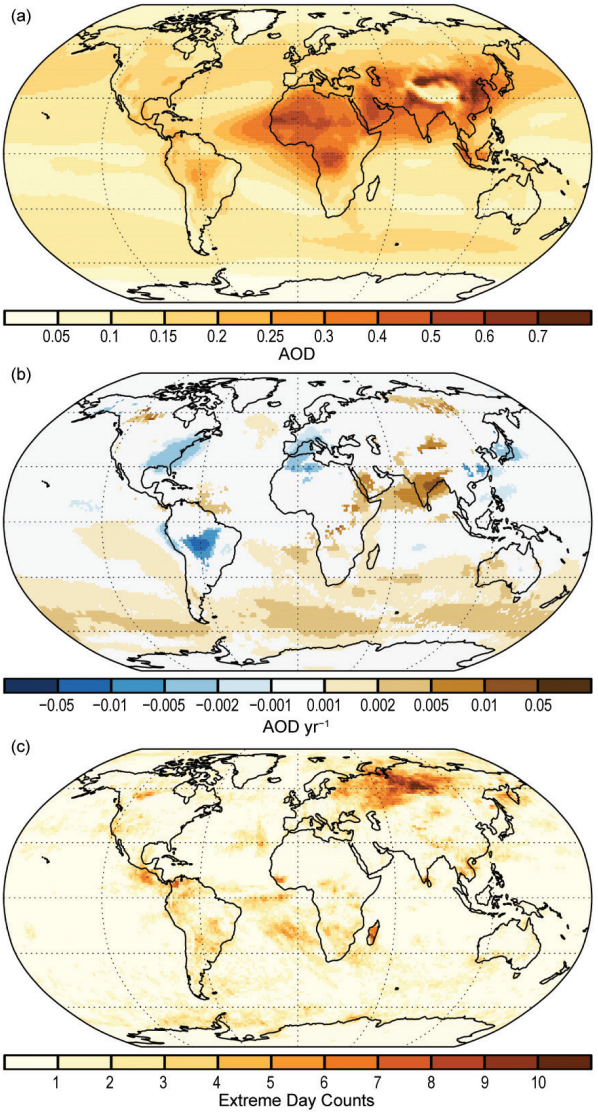

Fig. 2.49. (a) Total 550 nm AOD averages for 2003–16. Note the regional differences, with much greater total AOD values over parts of northern Africa, the Arabian Peninsula, southern Asia, and eastern China. (b) Linear trends of total AOD (AOD unit yr^{-1}) for 2003–16. Only trends that are statistically significant (95% confidence) are shown. (c) Number of days in 2016 with extremely high AOD (defined as greater than the 2003–16 average plus 5 std. dev.).

America, northwestern Canada, Southeast Asia, and Africa. Other contributors to extreme AOD values include dust events in the Mediterranean and North Atlantic, and sea salt events near the Antarctic coast.

4) Stratospheric ozone—M. Weber, W. Steinbrecht, S. M. Frith, O. Tweedy, M. Coldewey-Egbers, S. Davis, D. Degenstein, Y. E. Fioletov, L. Froidevaux, J. de Laat, C. S. Long, D. Loyola, C. Roth, and J. D. Wild

Total ozone columns in 2016 from GOME-2 were within a few Dobson units (DU) of the long-term (1998–2008) average for most of the globe (Plate 2.1s). At middle to high Northern Hemisphere (NH) latitudes total ozone was below the long-term average. The strong NH polar vortex observed during December 2015–February 2016, with record low temperatures and correspondingly large chlorine activation throughout, led to very low ozone values in the Arctic lower stratosphere during this period (not shown; Manney and Lawrence 2016). Very low stratospheric temperatures are needed to form polar stratospheric clouds (PSCs) that activate halogens (chlorine and bromine) for fast catalytic ozone depletion. Large ozone losses are regularly observed over Antarctica in the Southern Hemisphere (SH) spring (see Chapter 6h) but only sporadically over the Arctic. The observed Arctic ozone loss in early 2016 was comparable to or even stronger than the previous record loss during the Arctic winter 2010/11. Both winters showed Arctic ozone losses at levels typically only observed in the Antarctic ozone hole (Fig. 4 in WMO-GNR 2017; Manney et al. 2011).

In contrast, 2016 total ozone at middle to high SH latitudes was above average (Plate 2.1s) because of the below-average size of the Antarctic ozone hole in 2016 (see Chapter 6h). Both the size and intensity of ozone loss within the Antarctic vortex are variable and depend on the meteorology and atmospheric dynamics (transport) of any given winter.

At the equator there was a narrow band of slightly above-average total ozone (Plate 2.1s). Year-to-year variability of tropical total ozone is mainly governed by the phase of the quasi-biennial oscillation (QBO). The QBO is a periodic change of stratospheric winds in the lower to middle tropical stratosphere that affects the meridional (Brewer–Dobson) circulation and modulates high latitude ozone and the strength of the polar vortices (e.g., Strahan et al. 2015). In the 2015/16 boreal winter, radiosonde temperature observations revealed an unprecedented disruption in the downward propagation of the QBO westerly phase (Newman et al. 2016) that modified circulation and substantially impacted tropical and extratropical ozone (Tweedy et al. 2017). In Fig. 2.50, a "climatological" ozone QBO anomaly derived from deseasonalized SBUV Merged Ozone Data (MOD) V8.6 for 1982–2014 (14 QBO cycles) is compared to the ozone QBO evolution during late 2014–16. Each cycle is defined as starting when the vertical wind shear at 40 hPa shifts from negative (zonal wind decreasing with height) to positive. The long-term average evolution shows the typical increase in equatorial ozone associated with positive shear followed by a decrease associated with negative shear. The atypical cycle evolution in 2015/16 shows the anomalous equatorial ozone increase starting in June 2016.

The anomalous positive 40-hPa wind shear during April–November 2016 caused decreased tropical upwelling which led to a positive perturbation in tropical total ozone. This reduced upwelling was balanced by weaker extratropical downwelling, which decreased extratropical total ozone from April to September 2016. Total ozone shows markedly perturbed behavior in 2016 compared to the past, but the response of ozone and a variety of dynamical

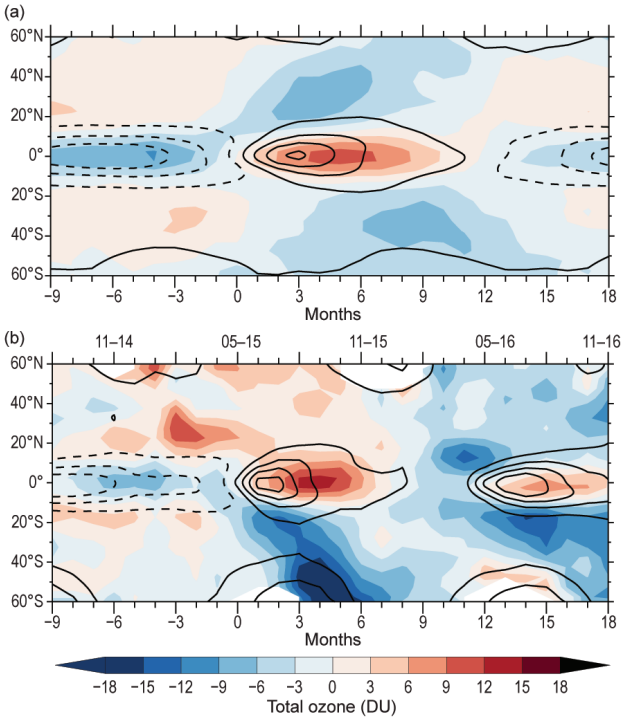

Fig. 2.50. Latitude–time evolution of the deseasonalized SBUV MOD V8.6 total ozone (color scale) for (a) the climatology of 14 QBO cycles (1982–2014) and (b) late 2014–16 (month–year indicated at the top). Solid and dashed black contours (interval is 2 m s^{-1} km^{-1}) show positive and negative vertical wind shear, respectively, for the composite and late 2014–16. Bottom axes show months before and after vertical wind shear changes from easterly to westerly at 40 hPa. Adapted from Tweedy et al. (2017).

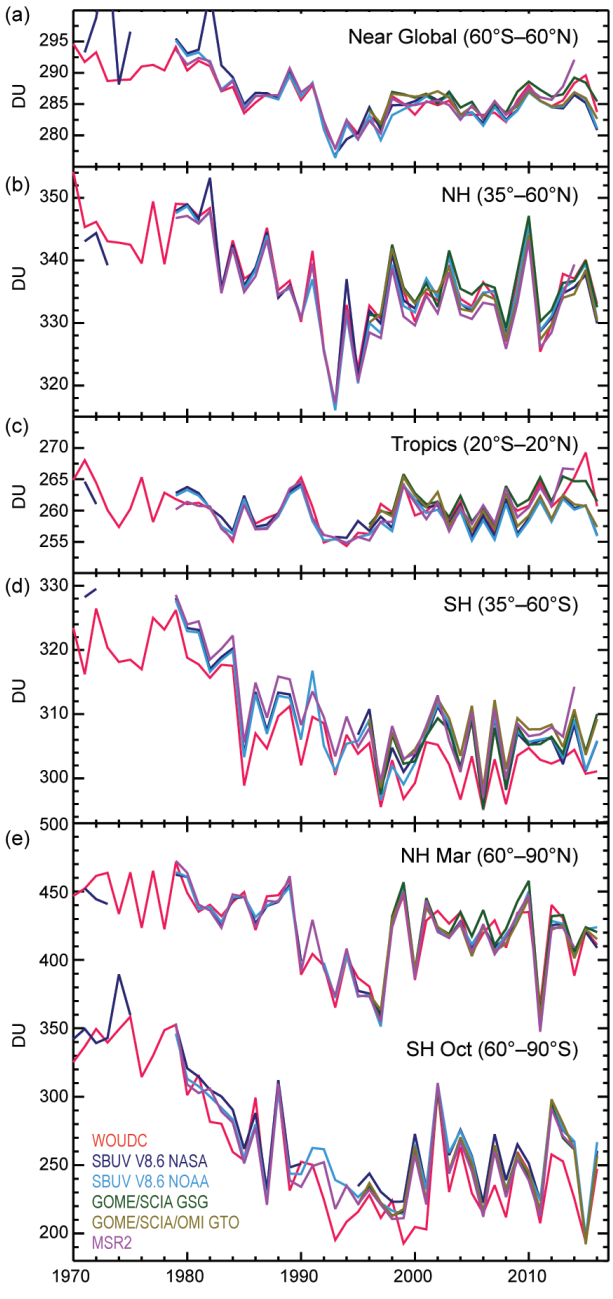

Fig. 2.51. Time series of annual mean total ozone in (a)–(d) four zonal bands and (e) polar (60°–90°) total ozone in Mar (NH) and Oct (SH). Data are from WOUDC ground-based measurements combining Brewer, Dobson, SAOZ, and filter spectrometer data (red; Fioletov et al. 2002, 2008); the BUV/SBUV/SBUV2 V8.6 merged products from NASA (MOD V8.6; dark blue; Chiou et al. 2014; Frith et al. 2014) and NOAA (light blue; Wild et al. 2016); the GOME/SCIAMACHY/GOME-2 products GSG from University of Bremen (dark green; Weber et al. 2011) and GTO from ESA/DLR (light green; Coldewey-Egbers et al. 2015); and the MSR V2 assimilated dataset extended with GOME-2 data (magenta; van der A et al. 2015). WOUDC values for 2016 are preliminary because not all ground station data were available at the time of writing this report.

and tracer fields is consistent with our understanding of the QBO-induced transport (Tweedy et al. 2017).

Time series of total column ozone annual means from different data sources are shown for 1970–2016 in various zonal bands (Fig. 2.51): near-global (60°N–60°S), middle latitudes in both hemispheres (35°–60°), and the inner tropics (20°N–20°S). Also shown are the polar time series in March (60°–90°N) and October (60°–90°S), the months when polar ozone losses are largest in the NH and SH, respectively (Fig. 2.51e). As a result of the early final warming in the Arctic (Manney and Lawrence 2016) and the breakup of the NH polar vortex, the 60°–90°N ozone levels in March 2016 quickly recovered to values close to the long-term mean despite the previously mentioned large chemical losses in early 2016.

Figure 2.51a shows that the continuous ozone decline due to the increase of ozone depleting substances (ODS) until the mid-1990s has ended. Since 2000 total ozone has leveled off in the extratropics of both hemispheres (Figs. 2.51b,d). Because the decline of ODS is slow (Section 2g2), ozone recovery is still difficult to separate from the considerable year-to-year variability. In the NH, tropical, and near-global averages, the annual mean ozone columns in 2016 were a few DU lower than those in the last couple of years, an expected result due to the declining phase of the 11-year solar cycle. Overall, the 2016 ozone columns are in agreement with expectations from

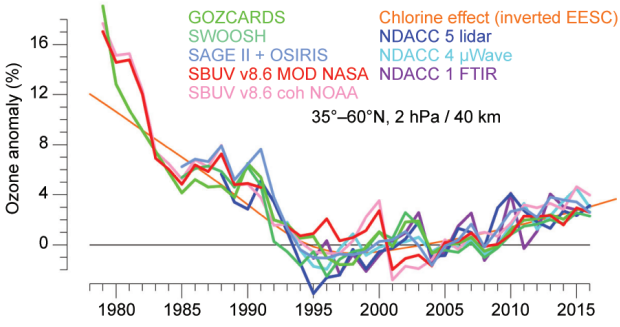

Fig. 2.52. Annual mean upper stratospheric ozone anomalies at 2 hPa (~40 km) in the zonal band 35°–60°N. Data are from the merged SAGE II/OSIRIS (Bourassa et al. 2014), GOZCARDS (Froidevaux et al. 2015), SWOOSH (Davis et al. 2016b), the BUV/SBUV/SBUV2 v8.6 merged products from NASA (Frith et al. 2014) and NOAA (Wild et al. 2016) as well as averages from five lidars, four microwave radiometers, and one FTIR measuring from the ground (Steinbrecht et al. 2009; Vigouroux et al. 2015). The anomaly basis for all time series is the 1998–2008 average of annual means. The thin orange curve represents EESC, inverted and scaled to reflect the expected ozone variations due to changes in stratospheric halogens. Data points for 2016 are still preliminary as of early 2017.

the last WMO Scientific Assessment of Stratospheric Ozone Depletion (WMO 2014).

The clearest signs of significant ozone recovery have occurred in the upper stratosphere at ~2 hPa/40 km (WMO 2014; Fig. 2.52). Both ground- and satellite-based measurements show recent increases of 2%–4% decade^{-1} in upper stratospheric ozone. At least in the upper stratosphere, adherence to the Montreal Protocol has successfully stopped the decline of stratospheric ozone and turned the previous downward trend into an upward trend since the late 1990s. Ensembles of chemistry–climate models indicate that the decline in stratospheric halogens and increases in greenhouse gases have contributed nearly equally to the positive ozone trend (WMO 2014).

5) Stratospheric water vapor—S. M. Davis, K. H. Rosenlof, D. F. Hurst, H. B. Selkirk, and H. Vömel

Stratospheric water vapor (SWV) levels varied dramatically during 2016. At the start of the year, water vapor mixing ratios in the tropical (15°N–15°S) lowermost stratosphere (at 82 hPa) were about 15% (0.5 ppm, parts per million mole fraction, equivalent to μmol mol^{-1}) above the previous decade's January average (Fig. 2.53). These positive anomalies followed the extremely high levels of SWV in November and December 2015 (Davis et al. 2016a; Fig. 2.54a) and the associated warm anomaly in cold point temperatures (CPTs) in the tropical tropopause layer (TTL) that began in mid-2015 and continued through the first two months of 2016 (Fig. 2.54b). The tropical SWV anomaly at 82 hPa in December 2015 (~0.9 ppm) is the highest observed in the now 13-year *Aura* Microwave Limb Sounder (MLS) record.

Between March and July 2016 the tropical SWV anomaly at 82 hPa dropped to ~0.2 ppm, then in August started to drop further, reaching –1.0 ppm in November 2016, the driest monthly anomaly observed in the *Aura* MLS record (Fig. 2.53b). Thus, from December 2015 to November 2016, the anomaly dropped by nearly 1.9 ppm, which is 40% of the long-term November mean tropical SWV mixing ratio at 82 hPa and 80% of the average seasonal cycle amplitude at 82 hPa in the tropics. In agreement with the MLS measurements, the steep water vapor decrease in the tropical lower stratosphere during 2016 was also observed by balloon-borne frost point hygrometer soundings at the tropical sites Hilo, Hawaii (20°N), and San José, Costa Rica (10°N) (Figs. 2.55b,c).

The annual cycle of tropical lower SWV is predominantly controlled by the annual cycle of CPTs in the TTL. These minimum temperatures are a major factor in determining the water vapor content of the lower stratosphere, because they impact the freeze–drying of moist tropospheric air during its slow ascent through the TTL. Seasonal to interannual variability in tropical SWV around 82 hPa is highly correlated with CPT variations. The dramatic decrease in tropical lower SWV during 2016 is consistent with the substantial ~1.5°C decrease in tropical CPTs over the same period (Fig. 2.55c).

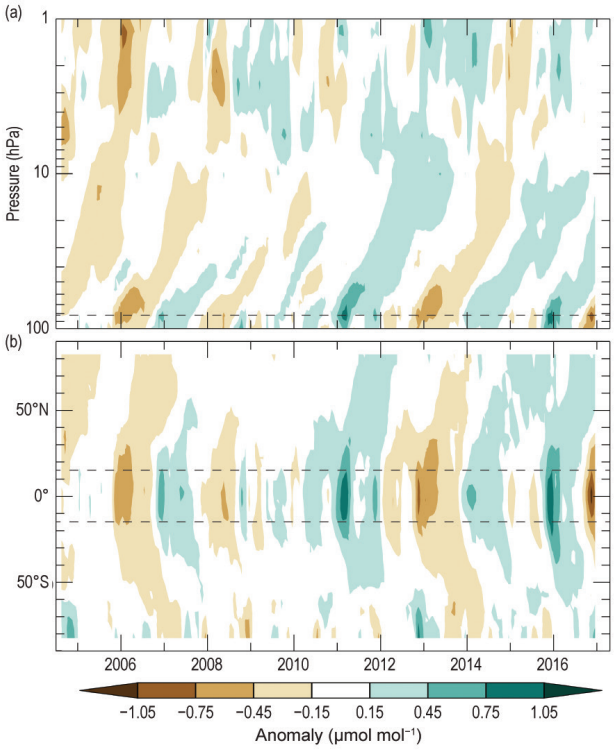

Fig. 2.53. (a) Time series of vertical profiles of tropical (15°N–15°S) stratospheric water vapor anomalies (μmol mol^{-1}) and (b) latitudinal distributions of SWV anomalies (μmol mol^{-1}) at 82 hPa. Both are based on *Aura* MLS data. Anomalies are differences from the mean 2004–2016 water vapor mixing ratios for each month. (b) Propagation of tropical lower SWV anomalies to higher latitudes in both hemispheres as well as the influences of dehydrated air masses from the Antarctic polar vortex as they are transported towards the SH midlatitudes at the end of each year. Dashed horizontal lines in the panels indicate (a) the 82-hPa pressure level and (b) the tropics 15°N–15°S.

Interannual variations in CPTs are partially related to interannual variability in the phases of ENSO and QBO in tropical stratospheric winds. At the beginning of 2016, the QBO was in a westerly (warm) phase at 70 hPa in the lowermost stratosphere, but an anomalous set of events brought descending easterlies to the tropical lower stratosphere during June–November 2016 (Newman et al. 2016; Osprey et al. 2016; Dunkerton 2016; Section 2e3). The colder TTL and drier tropical lower stratosphere at the end of 2016 is

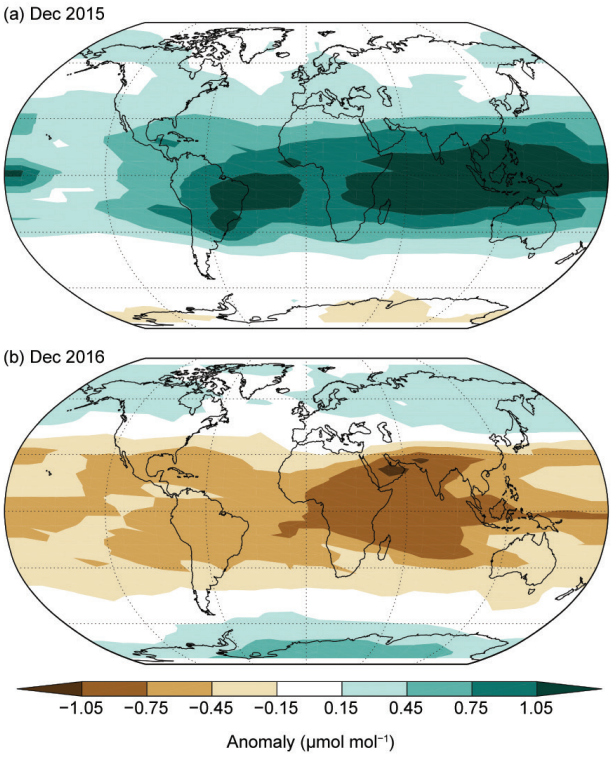

Fig. 2.54. Global stratospheric water vapor anomalies (μmol mol^{-1}) centered on 82 hPa in (a) Dec 2015 and (b) Dec 2016 from the *Aura* MLS. In Dec 2016 very strong negative (dry) anomalies were observed in the tropics and subtropics, in stark contrast to the strong positive (wet) anomalies of Dec 2015.

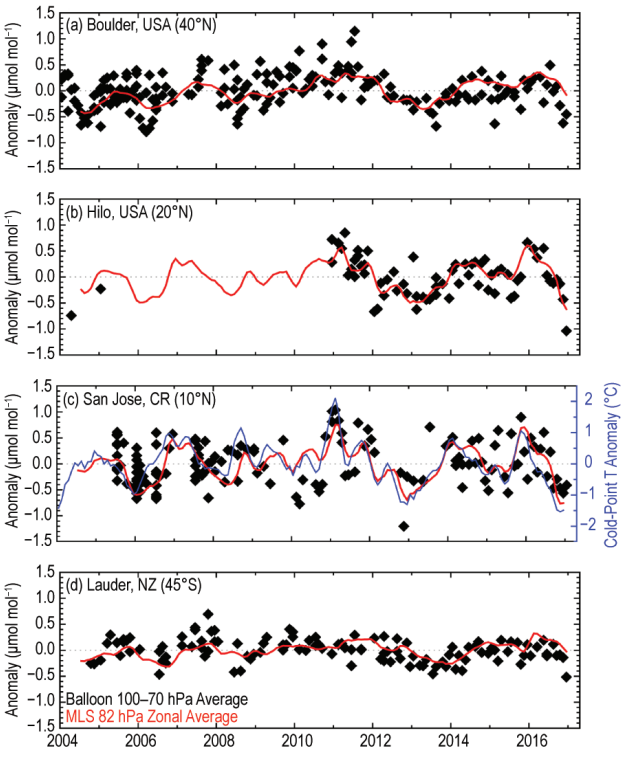

Fig. 2.55. Lower stratospheric water vapor anomalies (μmol mol^{-1}) over four balloon-borne frost point (FP) hygrometer stations. Each panel shows the lower stratospheric anomalies of individual FP soundings (black) and of monthly zonal averages of MLS retrievals at 82 hPa in the 5° latitude band containing the FP station (red). High-resolution FP vertical profile data were averaged between 70 and 100 hPa to emulate the MLS averaging kernel for 82 hPa. Each MLS monthly zonal mean was determined from 2000–3000 profiles. Tropical CPT anomalies based on the MERRA-2 reanalysis [blue curve in (c)], generally well correlated with the tropical lower SWV anomalies, are the driving force behind the sharp decline in tropical SWV during 2016.

consistent with descending easterlies in this region. The decrease in SWV over the tropical warm pool and the entire tropical Indian Ocean regions during the latter half of 2016 is consistent with an adiabatic response of the TTL to enhanced convection driven by the La Niña conditions present.

Water vapor anomalies in the tropical lowermost stratosphere propagate from the tropics to the middle latitudes of both hemispheres, as is demonstrated by the "C"-shaped contours in Fig. 2.53b. The early 2016 wet anomaly and the late 2016 dry anomaly in tropical lower SWV can be seen a few months later in the middle latitudes of each hemisphere. These midlatitude anomalies are also observed by balloon measurements at Boulder, Colorado (40°N), and Lauder, New Zealand (45°S) (Figs. 2.55a,d). SWV anomalies over Lauder were near zero during most of 2016 but dropped at the end of the year (Fig. 2.55d). The timing of this decrease is consistent with the poleward transport of the strong dry tropical anomalies that emerged in August 2016. The timing of the poleward transport is a function of season. There is less mixing of tropical air into the midlatitudes of the winter hemisphere because of the stronger winter jet, thus the dry tropical anomaly signal is seen at Boulder before Lauder (Figs. 2.55a,d). It should also be noted that SWV in the SH midlatitudes can be influenced during austral springtime (October–November) by the northward transport of air masses dehydrated within the Antarctic vortex. The lack of dry anomalies at high southern latitudes in December 2016 (Fig. 2.54b) indicates that the Antarctic dehydration in 2016 was not unusually strong. Therefore, the strong negative anomalies observed at Lauder in late 2016 are primarily attributed to the southward transport of the strong tropical dry anomalies.

6) Tropospheric ozone—J. R. Ziemke and O. R. Cooper

Tropospheric ozone is a greenhouse gas, a surface pollutant, and the primary source of the hydroxyl

radical (OH), the main oxidizing agent in the troposphere. Sources include transport from the stratosphere and photochemical production from a variety of precursor gases such as lightning NO_x, methane, biogenic hydrocarbons, and emissions from the combustion of fossil fuels and biomass (e.g., Sauvage et al. 2007; Martin et al. 2007; Leung et al. 2007; Murray et al. 2013; Young et al. 2013; Neu et al. 2014; Monks et al. 2015). Tropospheric ozone is variable at small (urban) to large (hemispheric) scales because of variations in its photochemical production (i.e., precursor gases and sunlight) and in atmospheric transport. Transport phenomena that drive large-scale variability include the El Niño–Southern Oscillation (e.g., Chandra et al. 1998, 2009; Sudo and Takahashi 2001; Doherty et al. 2006; Koumoutsaris et al. 2008; Voulgarakis et al. 2011) and the Madden–Julian oscillation (Sun et al. 2014; Ziemke et al. 2015). Variability at daily to annual timescales (e.g., Ziemke et al. 2015, and references therein) adds challenges to the quantification of decadal trends at hemispheric and global scales (e.g., Neu et al. 2014; Cooper et al. 2014; M. Lin et al. 2014; Parrish et al. 2014).

In 2012 the tropospheric ozone summary was based on measurements by ground- and satellite-based instruments (Cooper and Ziemke 2013). Since then the tropospheric ozone reports have utilized only OMI/MLS satellite measurements (Ziemke et al. 2006) because of delays in obtaining final quality-assured data from the ground-based sites (Cooper and Ziemke 2014, 2015; Ziemke and Cooper 2016). The 2016 analysis again relies mainly on the OMI/MLS satellite data after conducting an in-depth analysis of drift in the 12-year OMI/MLS tropospheric ozone record by comparing with global ozonesondes and OMI convective cloud differential measurements (Ziemke et al. 1998). A small drift of about +0.5 DU decade^{-1} was found, attributed to an OMI error in total ozone, and an appropriate correction has been applied to the OMI/MLS data.

Plate 2.1w shows broad regions of positive anomalies of up to 1.2 DU (4%) in NH tropospheric ozone columns for 2016 and mostly near-zero anomalies elsewhere. Hemispheric and global average tropospheric ozone burdens and their 95% confidence level uncertainties for 2016 were 151 ± 12 Tg for 0°–60°N, 136 ± 9 Tg for 0°–60°S, and 287 ± 21 Tg for 60°N–60°S (Fig. 2.56). Each of these 2016 averages represents an increase from previous years, continuing the long-term upward trends in tropospheric ozone. Linear trends in hemispheric and global burdens from October 2004 through December 2016 (Fig. 2.56) all depict increases of nearly 0.7% yr^{-1} that are statistically significant.

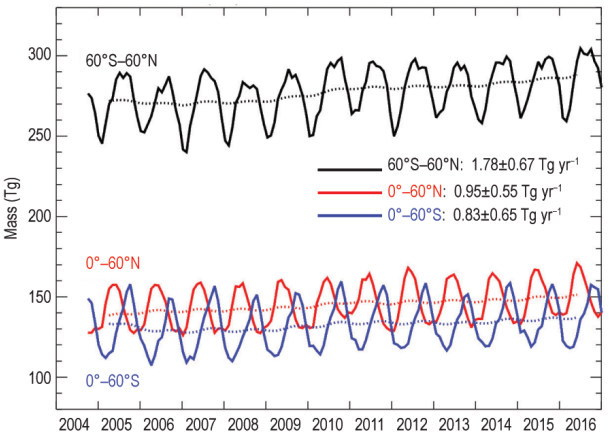

Fig. 2.56. Monthly averages of OMI/MLS tropospheric ozone burdens (Tg) for Oct 2004–Dec 2016. The top curve (black) shows 60°N–60°S monthly averages with 12-month running means. The bottom two curves show monthly averages and running means for the NH (red) and SH (blue). Slopes of linear fits to the data are presented with their 2-sigma uncertainties. All three trends are statistically significant at the 95% confidence level.

The spatial distribution of linear tropospheric ozone trends is shown on a 5° × 5° grid in Fig. 2.57. All the trends with statistical significance depict increases, the strongest of which [~3.5 DU decade^{-1} (1.1% yr^{-1})] are located in India, Southeast Asia, and the western Pacific. These upward trends are consistent with model estimates based on strengthening emissions of ozone precursors from Southeast, East, and South Asia primarily due to fossil fuel combustion (Yu. Zhang et al. 2016; Lin et al. 2017). The ozone produced in these densely populated areas is clearly transported eastward into the western Pacific region (Fig. 2.57).

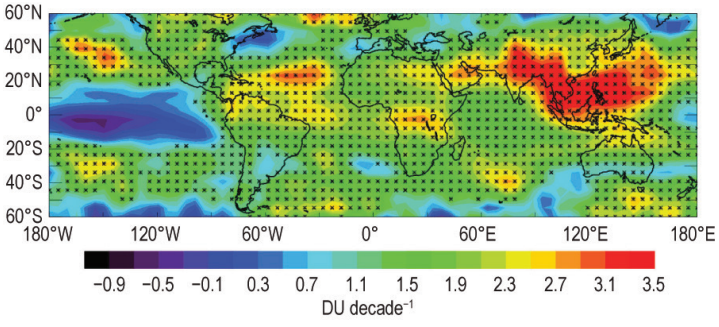

Fig. 2.57. Linear trends in OMI/MLS tropospheric column ozone (DU decade^{-1}) on a 5° × 5° grid for Oct 2004–Dec 2016. Asterisks denote statistically significant trends at the 95% confidence level. Note that all trends with statistical significance depict increases in tropospheric ozone.

As mentioned, it is difficult to annually update the global ozone distribution using surface observations because most measurement stations do not produce quality-assured final data rapidly enough for the timing of this report. One site with rapidly updated data is the high-elevation Mauna Loa Observatory (MLO) in Hawaii (19.5°N, 155.6°W, 3397 m asl). Nighttime ozone observations from MLO are representative of a broad region of the lower free troposphere. Figure 2.58 shows that ozone has increased at MLO since 1974, but the large interannual and seasonal variability make it difficult to determine statistically significant trends over the shorter time span of 2000–16. A new technique that can help reduce trend uncertainties and provide additional information is to examine ozone trends separately for the dry and moist air masses that reach the site. Drier air masses tend to originate at higher altitudes and latitudes to the west and northwest of MLO, while moist air masses tend to come from the east at lower latitudes and altitudes (Harris and Kahl 1990; Oltmans et al. 2006). Ozone observations at MLO were divided into dry (<40th percentile) and moist (>60th percentile) air masses using observed dew point temperatures and a long-term climatology. Since 2000, ozone in dry air masses has increased at the rate of 0.42 ± 0.22 ppb yr^{-1} while the trend in moist air masses is not significantly different from zero. The robust increase of ozone in dry air masses at MLO since 2000 suggests that the site is being influenced by ozone increases in upwind regions to the west and northwest, most likely Asia where limited in situ observations have shown general ozone increases over the past two decades at the surface (Cooper et al. 2014; Ma et al. 2016; Sun et al. 2016; W. Xu et al. 2016; Wang et al. 2017) and in the free troposphere (Yu. Zhang et al. 2016).

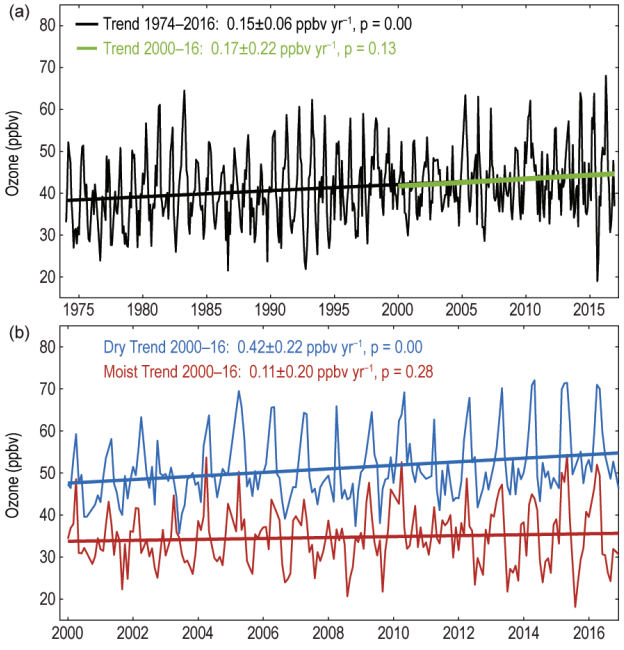

Fig. 2.58. (a) Monthly median nighttime ozone values at MLO for 1974–2016. Linear trends are reported for the full record and for 2000–16. (b) 2000–16 ozone trends at MLO for dry and moist air masses. Ozone in the dry air masses increased at 0.42 ± 0.22 ppbv yr^{-1} during 2000–16, a rise of 6.7 ppbv (14%) in 16 years. There was no statistically significant ozone increase in the moist air masses. The dry air masses reaching MLO tend to come from the northwest so the ozone increase is attributed to the positive ozone trends in southeast Asia (Fig. 2.57).

7) Carbon monoxide—J. Flemming and A. Inness

Carbon monoxide (CO) plays a significant role in determining the abundance of climate forcing gases like methane (CH_4), through hydroxyl radical chemistry, and tropospheric ozone, as a chemical precursor (Hartmann et al. 2013). CO is therefore regarded as an indirect climate forcing agent. Sources of CO include the incomplete combustion of fossil fuels and biomass and the oxidation of atmospheric CH_4 and other organic trace gases. The combustion and chemical oxidation sources typically produce similar amounts of CO each year.

The Copernicus Atmosphere Monitoring Service (CAMS) produced a retrospective analysis of CO, aerosols, and ozone for the period 2003–15 by assimilating satellite retrievals of these species (and others) with the ECMWF model (Flemming et al. 2017). Total column retrievals of CO from the MOPITT instrument (Version 5; Deeter et al. 2013) were assimilated in the CAMS interim reanalysis. Anthropogenic emission estimates were taken from the MACCity inventory (Granier et al. 2011) that accounts for projected emission trends according to the representative concentration pathways (RCP) v8.5 scenario (Riahi et al. 2011). Biomass burning emissions were taken from the Global Fire Assimilation System (GFAS v1.2; Kaiser et al. 2012). All analyses have now been extended to the end of 2016 and the updated data are used here.

Studies using MOPITT and other CO observations conclude that the global CO burden has decreased by about 1% yr^{-1} during the last decade (Worden et al. 2013; Yin et al. 2015; Flemming et al. 2017). A linear fit of the time series of monthly global CO burdens obtained from the CAMS interim reanalysis (Fig. 2.59) shows a decrease from 405 Tg in early 2003 to 365 Tg at the end of 2016, a trend of −2.9 ± 0.8 Tg yr^{-1} (−0.75% ± 0.20% yr^{-1}). Seasonal variations in the global burden result from seasonal changes in CO sources (combus-

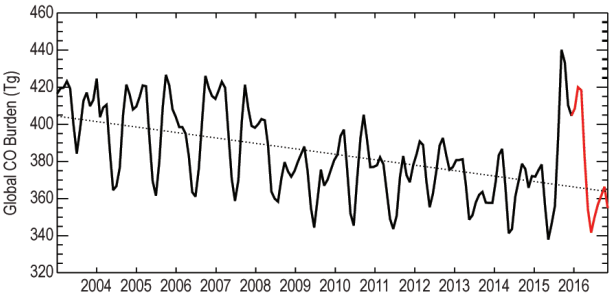

Fig. 2.59. Time series of monthly global total column CO burdens (Tg) from the CAMS interim reanalysis for 2003–15 (black curve) and 2016 (red curve). The linear fit over 2003–16 (dotted black line) indicates a trend of −2.9 ± 0.8 Tg yr^{-1} (−0.75% ± 0.20% yr^{-1}).

tion) and sinks (OH). The large upward spike in the CO burden during the latter half of 2015 was due to exceptionally strong biomass burning emissions in Indonesia during September and October. The anomalously high global CO burden persisted into early 2016, but by mid-2016 had decreased to levels conforming to the decadal trend.

Annual average CO anomalies for 2016 were small (< 5%) with much of the tropics and SH slightly above the long-term median, with the exception of a strong negative anomaly over the maritime continent, and most of the NH middle and high latitudes slightly below the median (Plate 2.1ae). However, these annual averages don't clearly show that predominantly strong positive anomalies in the first six months (Fig. 2.60a) changed to pronounced negative anomalies in the second six months (Fig. 2.60b). During January–June 2016 the tropical and SH anomalies were still positive due to the Indonesian fires in September–October 2015 and intense fire emissions during January–March 2016 in tropical Africa and South America. During July–December 2016 most of the globe showed strong (5%–10%) negative CO anomalies, in particular over the eastern half of North America, the outflow region from South America toward southern Africa, and a pronounced –30% anomaly over maritime Southeast Asia. The latter anomaly, which also appeared as a –15% annual average anomaly (Plate 2.1ae), was caused by a strong reduction in fire emissions from Indonesia and northern Australia. Intense fires in central Siberia during July produced a localized positive anomaly for the last six months of 2016. The May 2016 Fort McMurray fire in Canada is visible as a small positive anomaly in the January–June map (see Sidebar 7.1).

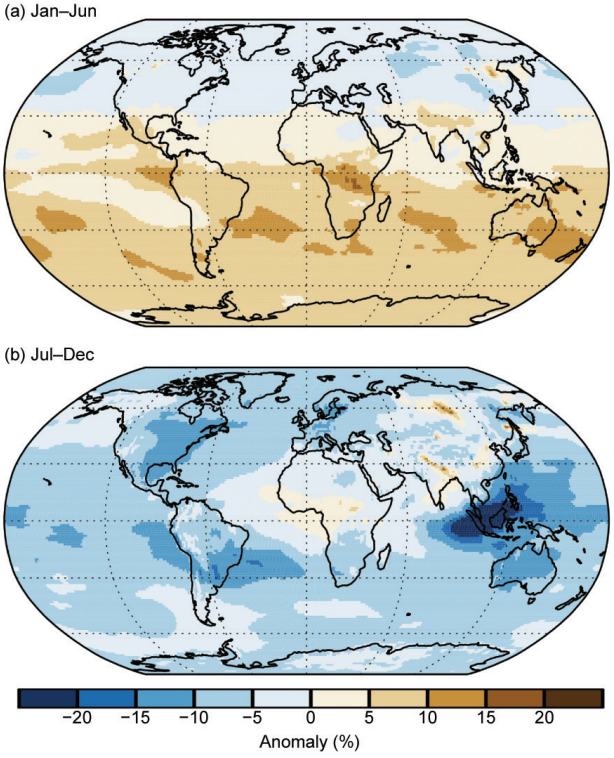

Fig. 2.60. Total column CO anomalies (%) for (a) Jan–Jun 2016 and (b) Jul–Dec 2016 with respect to the 2003–16 median from the CAMS interim reanalysis.

h. Land surface properties

1) Land surface albedo dynamics—B. Pinty and N. Gobron

The land surface albedo represents the fraction of solar radiation scattered backward by land surfaces. In the presence of vegetation, surface albedo results from complex nonlinear radiation transfer processes determining the amount of radiation that is scattered by the vegetation and its background, transmitted through the vegetation layer, or absorbed by the vegetation layer and its background (Pinty 2012).

The geographical distributions of normalized anomalies in visible and near-infrared surface albedo (V005) for 2016 calculated for a 2003–16 base period (for which two MODIS sensors are available; Schaaf et al. 2002) are shown in Plates 2.1ab,ac, respectively. Mid- and high latitude regions of the Northern Hemisphere are characterized by both positive (blue) and negative (orange) anomalies mainly as a consequence of interannual variations in snow cover (Section 2c2), amount, and duration in winter and spring seasons. The large negative anomalies especially in the visible range over central and eastern Europe, Kazakhstan, western and far east Russia, northeastern China, and across parts of the Tibetan Plateau are probably associated with a below-average snow cover in late winter and early spring seasons, due to the occurrence of anomalous warmth in most of these regions, especially from February onwards. Similarly, negative anomalies over Alaska, central Canada, and north-

eastern United States can be associated with the fast decline of the snow cover extent and duration as early as February due to unusually warm conditions. These negative anomalies would have been even stronger except for an above-average snow extent in January for the United States and much of Canada, and also in eastern and north central Europe and much of Asia. Nevertheless they reached (or locally exceeded) –30% and were larger in the visible than in the near-infrared domain although with the same sign.

A few snow-free regions show slight positive anomalies, especially in the visible domain, in equatorial regions, northeast Brazil, southern Africa, and northeast of the Black Sea. These are generally associated with less favorable vegetation growing conditions in comparison with previous years (see Section 2h2) although contamination of the albedo retrievals by clouds and aerosol load (especially in intertropical regions) may also induce artifacts. A large fraction of snow-free regions exhibit spatially consistent noticeable negative anomalies, in particular in the visible domain, across Mexico and southern United States, and over the southern regions of South America (including La Pampa and Rio Negro provinces in Argentina), Australia, Indonesia, and southern and central China. Consistent warmer-than-usual conditions persisted over most of these regions, sometimes associated with above-average precipitation. A significant fraction of these variations are attributable to vegetation dynamics (Pinty et al. 2011a,b) over these regions particularly sensitive to water availability. Although weaker in the near-infrared domain, these negative anomalies are, in some instances, spectrally correlated. The amplitude of these positive and negative anomalies often changes with seasons.

Analysis of the zonally averaged albedo anomalies in the visible (Fig. 2.61a) and near-infrared (Fig. 2.61b) spectral domains indicates considerable interannual variations related to the occurrence of snow events in winter and spring at mid- and high northern latitudes, as well as to vegetation conditions during the spring and summer periods. Strong negative anomalies are noticeable between 20° and 45°S in 2016, featuring a deviation from average conditions mainly over South America and Australia. Consistent negative anomalies in the visible domain are discernible across midlatitude regions in the Northern Hemisphere in 2016.

The amplitude of the globally averaged normalized anomalies resulting from a 12-month running mean (Figs. 2.62a,b) is within ±5% (3%) of the mean in the visible (near-infrared) domain. The anomalies are not estimated over Antarctica due to missing data. The year 2016 is characterized by negative anomalies in

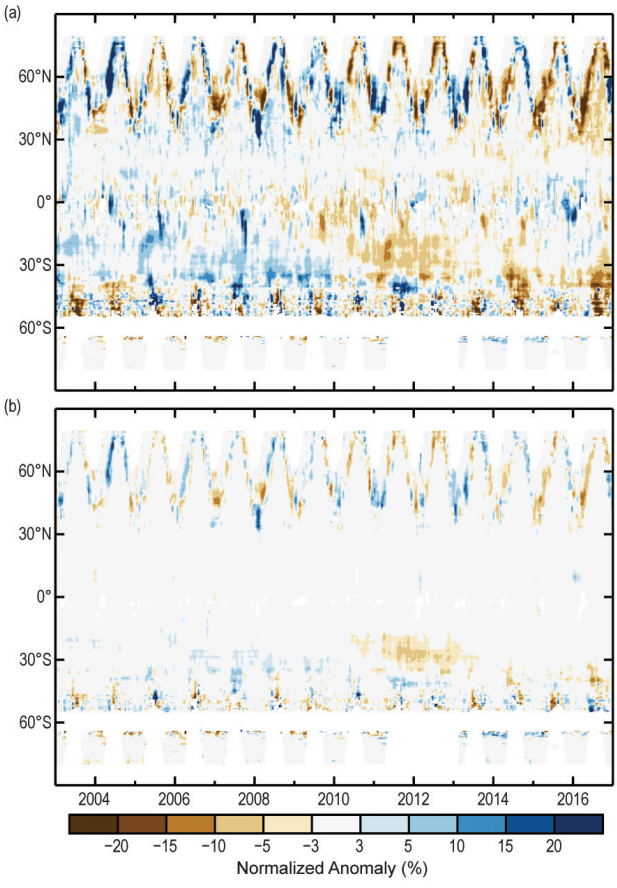

Fig. 2.61. Zonal means of the MODIS white-sky broadband surface albedo normalized anomalies (%) in the (a) visible and (b) near-infrared domains relative to the 2003–16 base period.

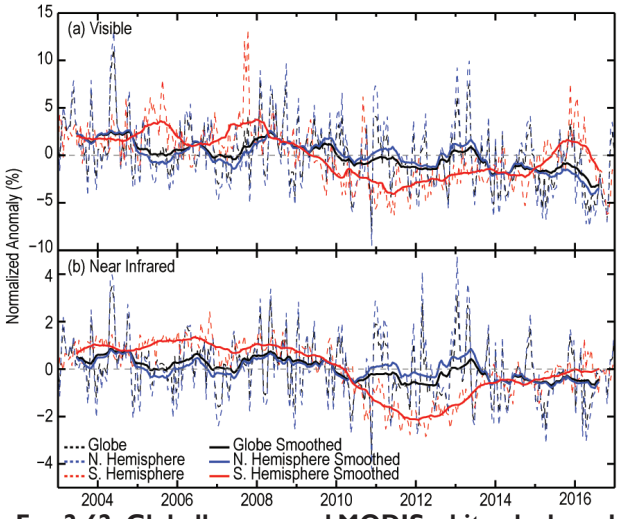

Fig. 2.62. Globally averaged MODIS white-sky broadband surface albedo normalized anomalies with a 12-month running mean in the (a) visible and (b) near-infrared domain relative to the 2003–16 base period at global scale (black) and over SH and NH in red and blue, respectively.

the visible domain driven by the dominant contributions from Northern Hemisphere regions. Figure 2.62 also indicates the presence of spectrally correlated multiannual variations during the 2003–16 base period with positively biased values at the beginning of this period.

2) Terrestrial vegetation dynamics—N. Gobron

Analysis of the 19-year record shows that large spatiotemporal deviations in vegetation dynamics occurred at regional and continental scales during 2016 (Plate 2.1aa). The state of vegetation is examined by merging 1998–2016 estimates of the Fraction of Absorbed Photosynthetically Active Radiation (FAPAR) from three different sensors: SeaWiFS (NASA), MERIS (ESA) and MODIS (NASA) (Gobron et. al. 2010; Pinty et al. 2011b; Gobron and Robustelli 2013). A large number of regions experienced much higher-than-average annual temperatures during 2016 along with a few extreme precipitation and regional drought events. This translates into a large geographical variation in vegetated surface conditions at the global scale.

The largest annual negative FAPAR anomalies (not favorable for vegetation) occurred over Alaska, the central Siberian plateau, and the northeast region of Brazil. Over most of the southern half of the African continent vegetation was stressed, especially over the equatorial regions with evergreen forest, the coastal zones of Kenya and Tanzania, and the Kwazulu-Natal region of South Africa. To a lesser extent, India and the Black and Caspian Seas regions were also affected.

The largest positive annual anomalies are detected over the Saskatchewan–Montana region (Canada–U.S.), West and East Kazakhstan, the southern regions of Ukraine, the eastern part of China, and Indonesia. In the Southern Hemisphere, La Pampa and Rio Negro provinces in Argentina, the wheat belt of western Australia, and northern parts of Victoria (eastern Australia) also show positive anomalies. Smaller positive anomalies occurred over a large fraction of the North American continent, eastern Europe, and central Russia.

The poor rainy season over Africa together with higher temperatures and drought events in South Africa impact the annual anomalies over this continent. The anomalies over Alaska were mainly due to a warmer-than-normal year. Precipitation belowthe seasonal average over the northeast regions of Brazil may be the main cause for the occurrence of strong annual negative anomalies there. Higher-than-normal-precipitation over the second half of the year over La Pampa and Rio Negro provinces in Argentina contributed to favorable conditions for vegetation health and growth.

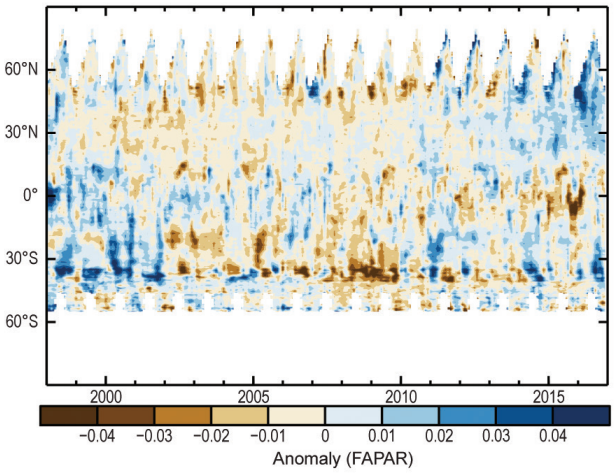

Fig. 2.63. Time series of monthly zonal anomalies (base period: 1998–2016) of FAPAR from SeaWiFS, MERIS, and MODIS sensors. Gray areas indicate missing data.

Zonally averaged monthly mean anomalies (Fig. 2.63) illustrate the differences between the two hemispheres, with persistent negative anomalies over the Southern Hemisphere during all seasons between 2002 and 2009. Large positive anomalies over the Northern Hemisphere exist in 2016 as well as over regions located around 20°–30°S during the second half of the year.

The monthly mean averaged anomalies for 2016, smoothed using a 12-month running average (Fig. 2.64), indicate a relatively healthy state of the vegetation at the global scale and over the Northern Hemisphere, compared with a slightly less healthy state over the Southern Hemisphere.

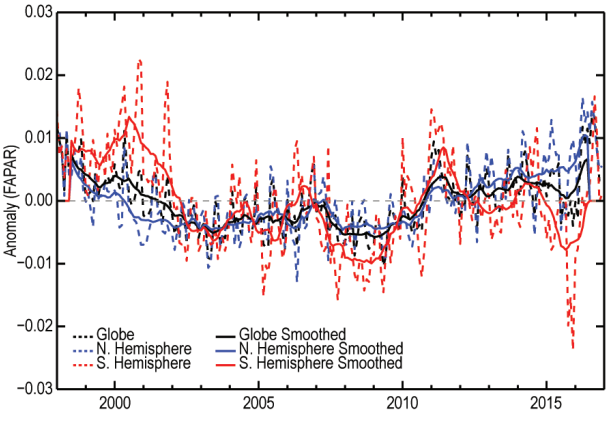

Fig. 2.64. Average monthly FAPAR anomalies with a 12-month running mean (base period: 1998–2016) at the global scale (black) and for the NH (blue) and SH (red).

3) Biomass burning—J. W. Kaiser and G. R. van der Werf

Fire has been increasingly recognized as a major source of aerosols and (greenhouse) gases. Especially in the tropics, humans start most fires, but climate governs the temporal and spatial fire patterns leading to relatively large fluctuations in fire strength. On average, fires burn about 500 million hectares, the size of the European Union, each year with the majority of burned areas occurring in tropical savannas.

Since the late 1990s fire occurrence and the associated burned areas have been routinely detected by satellites. The Global Fire Assimilation System (GFAS) builds on active fire detections and their associated fire radiative power to estimate emissions in near-real time (Kaiser et al. 2012). GFAS is calibrated to partly match the Global Fire Emissions Database (GFED) which estimates emissions based on burned area and fuel consumption with a much longer latency (van der Werf et al. 2010). The combined use of GFAS (2001–16) and GFED (1997–2014) indicates that fire emissions were on average 2.1 Pg C yr^{-1} (1 Pg = 10^{15} g; C is carbon) with substantial interannual variability mostly stemming from tropical deforestation zones and the boreal regions where fire activity varies more from year to year than in most savanna areas.

In 2016, negative regional anomalies of around –75 Tg C (1 Tg = 10^{12} g) in each of tropical Asia, Australia, and Southern Hemisphere America led to total global fire emissions below average (–6%; see Table 2.7, and Plate 2.1ad). Tropical Asia stands out with an 85% drop in fire activity from 2015 to 2016 (Fig. 2.65); these two years represent the highest and second lowest value in the GFAS record, respectively. Furthermore, North America experienced a negative anomaly of –30 Tg C (Table 2.7), and its monthly peak fire activity was the lowest in the GFAS record (Fig. 2.65).

Stronger-than-usual fire activity occurred in particular in northern and southeastern Asia, with anomalies of +51 Tg C and +44 Tg C, respectively. Emissions from northern Asia are dominated by boreal fires in Siberia. These are known to have a strong interannual variability, and the 2016 emissions were within the previously recorded range. However, fires in Southeast Asia were not more active earlier in the GFAS period. Their strong positive anomaly came from the Indochinese peninsula, where fires are dominated by human activity (see Plate 2.1ad). Further positive anomalies were recorded in Central America and Africa north of the equator. The latter is noteworthy because the general trend over the past decade has been one of decreasing emissions there, linked to the expansion of cropland at the cost of frequently burning savannas (Andela and van der Werf 2014).

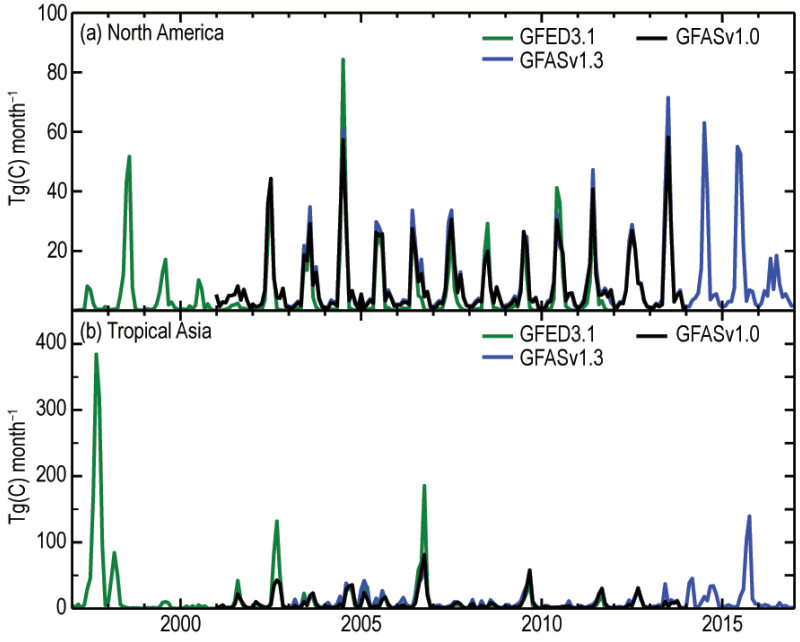

Fig. 2.65. Time series of fire activity during 1997–2016 in terms of carbon consumption for (a) North America and (b) tropical Asia.

Table 2.7. Annual continental-scale biomass burning budgets in terms of carbon emission (Tg C yr^{-1}): 2001–02 from GFASv1.0 (Remy and Kaiser 2014), 2003–16 from GFASv1.3.

Time Period		2001–15	2016	
Quantity in Tg C yr^{-1}		Mean Value (Range)	Value	Anomaly (%)
Global		2052 (1652–2339)	1918	−133 (−6%)
North America	30°–57°N 170°W–30°W	112 (50–167)	82	−30 (−27%)
Central America	0°–30°N 170°W–30°W	68 (49–101)	86	+18 (+27%)
SH America	0°–60°S 170°W–30°W	310 (153–474)	231	−79 (−25%)
Europe and Mediterranean	30°–75°N 30°W–60°E	35 (19–62)	29	−7 (−17%)
NH Africa	0°–30°N 30°W–60°E	402 (331–506)	427	+26 (+6%)
SH Africa	0°–35°S 30°W–60°E	519 (473–591)	506	−13 (−3%)
Northern Asia	30°–75°N 60°E–170°W	205 (105–470)	256	+51 (+25%)
Southeast Asia	10°–30°N 60°E–170°W	128 (83–171)	171	+44 (+62%)
Tropical Asia	10°N–10°S 60°E–170°W	114 (22–329)	43	−71 (−62%)
Australia	10°–50°S 60°E–170°W	159 (52–296)	86	−73 (−46%)

The Martian Atmosphere

In terms of its atmosphere and climate, Mars is the planet in the solar system most similar to Earth (e.g., Read and Lewis 2004; Read et al. 2015). With roughly half the radius of Earth (3396 km compared to 6371 km), Mars has around the same land surface area as Earth. Its tenuous atmosphere is composed mostly of CO_2 (95% by mass) plus much smaller amounts of N_2 (1.9%), Ar (1.9%), O_2 (0.15%), CO, H_2O, and other trace gases (Mahaffy et al. 2013) with a mean surface pressure of 6.1 hPa. It orbits at a distance of 1.4–1.6 AU[1] from the sun, receiving around half the solar irradiance of Earth (with significant annual variations) and with an orbital period of 687 Earth days. Mars rotates about its axis with a period scarcely different from Earth (24^h 40^m) and with an obliquity of 25°, resulting in a seasonal pattern of solar forcing that is remarkably Earth-like (although the seasons are longer in duration). It also sustains massive, permanent caps of water ice which are comparable in mass to Earth's Greenland ice sheet. Winter temperatures fall so low (−128°C, at the surface) that CO_2 also freezes, falling from clouds as snow or condensing directly onto the surface as frost, with up to one third of the total atmospheric mass deposited on the winter pole.

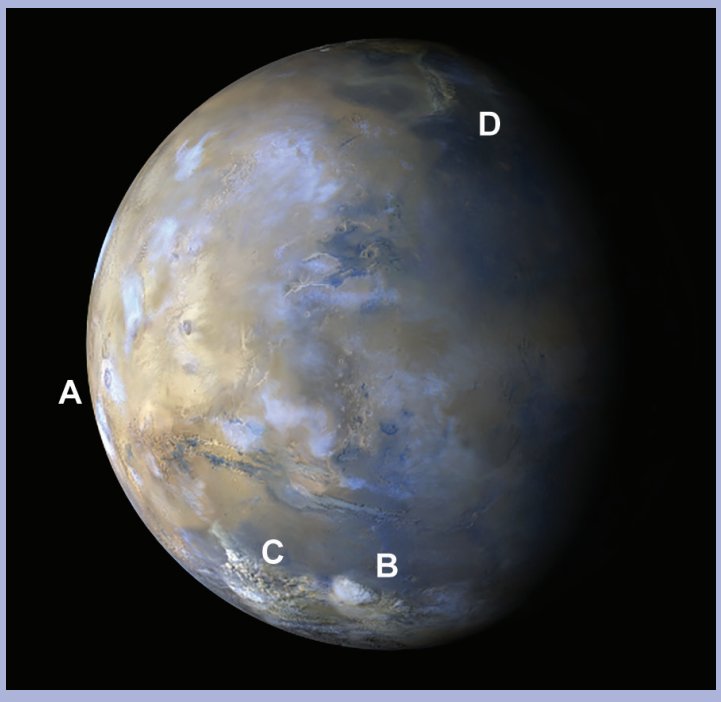

FIG. SB2.1. Mars as seen in May 2016 by the MARCI instrument on board the *Mars Reconnaissance Orbiter* spacecraft. Blueish-white features at low and midlatitudes are afternoon water ice clouds, typically tied to high topography, for example, the Tharsis Ridge volcanoes (A). White patches at high southern latitudes show surface frosts and fogs (e.g., B). Regional dust storms appear yellow, for example, lower left of center close to the southern cap (C), and the arc right of center at the top of the disc (D). (Image credit: NASA/JPL-Caltech/Malin Space Science Systems.)

Despite the low atmospheric density, Mars is meteorologically active with intense mid-latitude/circumpolar baroclinic storms during autumn, winter, and spring, and frequent dust storms, especially during southern summer (when the planet is closest to the Sun at perihelion). Without surface oceans, this is essentially a desert planet with landscapes variously resembling arid sand and boulder fields or rugged mountain ranges found on Earth, although with numerous ancient impact craters and volcanic peaks. Hence seasonal variations in temperature in response to solar forcing are typically much larger than on Earth, and even the diurnal cycle leads to a strong atmospheric thermal tide that dominates the weather in the tropics.

Even though the present climate is cold, dry, and inhospitable, geological evidence indicates that Mars was more hospitable in the distant past (more than 3 Gyr ago), with features suggesting erosion by large volumes of flowing water, persistent lakes, or active glaciers, although the precise conditions are still controversial. But the existence of liquid water at the surface raises the possibility that Mars previously sustained life, so it has long been targeted for detailed exploration of its surface and climate, using both observations and model simulations.

Measuring and modeling the Martian atmosphere

In recent years a succession of sophisticated space missions have visited the planet, aimed at surveying and analyzing the Martian surface and atmosphere, both from orbit and using in situ surface landers. Since the late 1990s, starting with NASA's *Mars Global Surveyor* (*MGS*) spacecraft, Mars has been observed from circular polar orbit at relatively low altitude (350–450 km), enabling remote sensing of the thermal structure of the atmosphere via infrared spectrometry and the detection of clouds and

[1] Where 1 AU is the mean Earth–Sun distance of 1.496×10^8 km; see http://nssdc.gsfc.nasa.gov/planetary/factsheet/marsfact.html.

aerosols of mineral dust, water, and CO_2 ice. The mapping configuration of *MGS* provided 12 sun-synchronous orbits per Martian day, sampling the full range of latitude and longitude across the planet every day (albeit fairly sparse in longitude), allowing the Thermal Emission Spectrometer (TES) instrument to recover profiles of temperature from the surface to altitudes of 40–50 km, together with column densities of dust and ice. This measurement density and consistency lends itself well to data assimilation approaches, given the availability of a suitable numerical models (e.g., Lewis et al. 2007; Hoffman et al. 2010). Such models borrow heavily from the techniques used for Earth and have now reached a level of sophistication that is beginning to rival Earth climate models, with complex radiative transfer parameterizations (including dust and ice clouds), hydrological cycles for both water and CO_2, dust transport cycles, dust storm evolution, and a range of surface processes (Forget et al. 1999; Newman et al. 2002; Steele et al. 2014).

Since the end of the *MGS* mission in 2004, a number of other spacecraft have continued to remotely sense the surface and atmosphere with increasing coverage and resolution, including NASA's *Mars Odyssey* and *Mars Reconnaissance Orbiter* (*MRO*), and ESA's *Mars Express* orbiter. The *MRO* in particular is equipped with the infrared limb-sounding instrument Mars Climate Sounder (McCleese et al. 2007), which can obtain vertical profiles of atmospheric temperature, dust, and ice opacity (Kleinböhl et al. 2009, 2011, 2017). This combination of instruments has thus extended the *MGS* record, so that the complete observational record stretches from 1999 to the present and consists of more than eight Mars years. Such a consistent record is transforming our view of the Martian climate, allowing detailed studies of dynamical processes across the planet and a clearer perspective on the interannual variability of Martian meteorology.

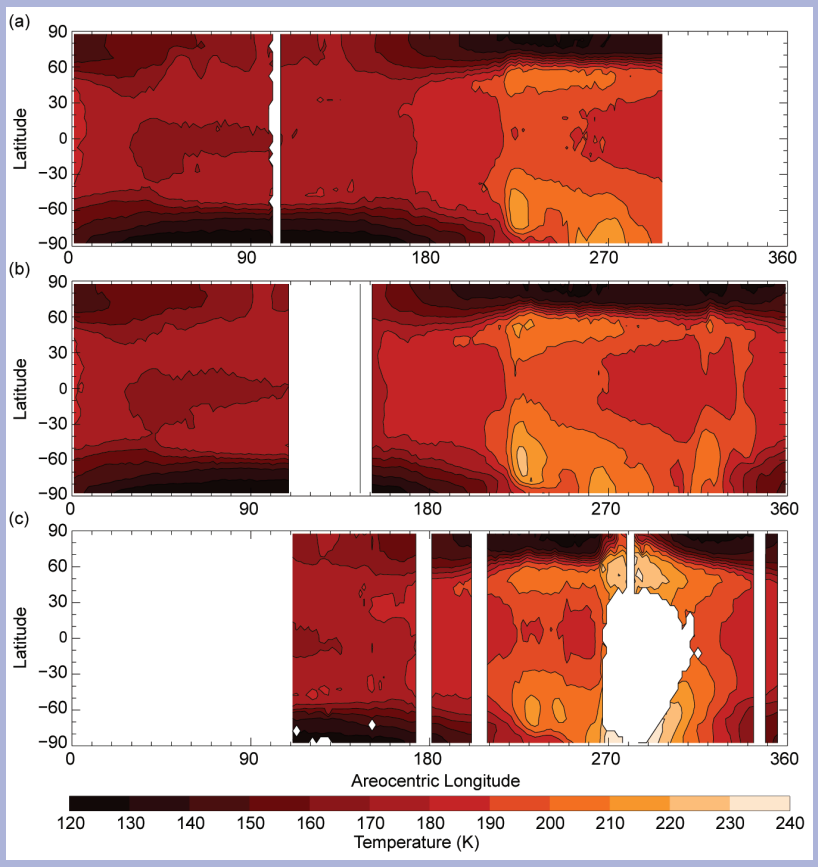

Fig. SB2.2. Zonally averaged temperature (K) on the 50-Pa surface as a function of time of year (LS) for (a) MY33 to Jan 2017, (b) MY32, and (c) MY28 from the start of the Mars Reconnaissance Orbiter mission; data from the MCS instrument. White indicates periods of missing data or when temperature retrievals on the surface were impossible owing to high levels of atmospheric dust.

The Martian climate in 2016–17

Figure SB2.1 shows a composite image of Mars, taken on 8 May 2016 (when Mars was farthest from the Sun; aphelion). The season is mid–late northern hemisphere summer on Mars [L_S = 149°, where areocentric longitude[2] is an angle that measures the seasonal date such that L_S=0° and 180° represent northern spring and autumn equinoxes while 90° and 270° represent summer and winter solstices]. Solar heating is significantly reduced near aphelion due to being farther from the Sun, and the atmosphere is typically colder and clearer than at other times of year. The regional dust storm, indicated by the arc-like feature (D in Fig. SB2.1), is dust revealing frontal-like behavior in a northern hemisphere weather system. Baroclinic cyclone waves, of similar horizontal scale to

[2] The year on Mars starts at L_S = 0°, northern hemisphere vernal equinox (as the civil year once did on Earth).

terrestrial weather (on the order of 1000 km), circulate around the northern mid-high latitudes (around 60°N) throughout autumn, winter, and spring (Lewis et al. 2016).

Figure SB2.2 shows how the zonal mean temperature retrieved on the 50-Pa pressure surface from the Mars Climate Sounder instrument aboard NASA *MRO* varied during the last two Mars years (MY) and during the first year of the mission, which featured a stronger, global dust event in northern winter. Following Clancy et al. (2000), MY are commonly numbered following a scheme where MY1 began on 11 April 1955; northern hemisphere winter of MY33 on Mars started 28 November 2016. Data from the day side of the MRO sun-synchronous orbit have been binned into 5° latitude and 2° L_S bins and averaged over all longitudes. The 50-Pa surface lies about 25 km above the reference datum on Mars, except during global dust events (e.g., MY28, L_S = 265°–300°), when it rises to about 30 km as the lower atmosphere warms and expands.

The most obvious features of the annual temperature cycle are the cold winter poles in both hemispheres. The first half of the year, northern hemisphere spring and summer, is typically cooler than the second half, as explained in connection with Fig. SB2.1. The notable warm patches at mid- to high southern latitudes from L_S = 220°–240° and L_S = 250°–290° are large dust events, denoted storms A and B following Kass et al. (2016). Neither approach global scales or are particularly strong in MY33; the warming at similar times at northern midlatitudes is the dynamical consequence of these dust storms, which enhance the strength of the single cross-equatorial Hadley cell, resulting in stronger adiabatic heating in the descending branch. So far, the Martian atmosphere in MY33 has appeared remarkably similar to the previous year on Mars (MY32; Fig. SB2.2b) with, if anything, even weaker dust storm activity. This is in direct contrast to some previous years, e.g., MY25 and MY28 (Fig. SB2.2c), which exhibited global dust events that warmed the atmosphere significantly (by up to 40 K) at these altitudes over a large range of latitudes and for intervals of at least 50 days.